FIRST PRINCIPLES DFT ANALYSIS OF LEAD FREE Rb_2MInX_6 DOUBLE PEROVSKITE HALIDES FOR PHOTOVOLTAIC APPLICATIONS

A thesis submitted to the

Department of Materials and Metallurgical Engineering (MME)

of

Bangladesh University of Engineering and Technology (BUET)

In partial fulfillment of the requirement for the degree of

MASTER OF SCIENCE IN MATERIALS AND METALLURGICAL ENGINEERING

by

Md. Jahidul Islam

Roll: 0421112004

Department of Materials and Metallurgical Engineering

BANGLADESH UNIVERSITY OF ENGINEERING AND TECHNOLOGY (BUET)

December 2022

This thesis titled "**First Principles DFT Analysis of Lead Free Rb2MInX6 Double Perovskite Halides for Photovoltaic Applications**" submitted by Md. Jahidul Islam, Roll No. 0421112004 and Session: April 2021 has been accepted as satisfactory as a partial fulfilment of the requirement for the degree of Master of Science in Materials and Metallurgical Engineering on 17 December, 2022.

BOARD OF EXAMINERS

Dr. Fahmida Gulshan Professor Department of MME, BUET, Dhaka	Chairman (Supervisor)
Dr. AKM Bazlur Rashid Professor & Head Department of MME, BUET, Dhaka	Member (Ex-Officio)
Dr. Kazi Mohammad Shorowordi Professor Department of MME, BUET, Dhaka	Member
Dr. Md. Muktadir Billah Associate Professor Department of MME, BUET, Dhaka	Member
Dr. Syed Ansar Md Tofail Associate Professor and Head Department of Physics, University of Limerick, Ireland	Member (External)

CANDIDATE'S DECLEARATION

IT IS DECLERED THAT THIS THESIS PAPER OR ANY PART OF IT HAS NOT SUBMITTED ANYWHERE ELSE FOR THE AWARD OF ANY DEGREE.

(Signature)

Md. Jahidul Islam

... ...

Md. Jahidul Islam

ACKNOWLEDGEMENT

At the very beginning, I would like to express my heartiest gratitude towards the Almighty for providing me the chance to complete my thesis within time.

I express my sincere gratitude to my supervisor, Prof. Dr. Fahmida Gulshan, for her kind supervision, indispensable guidance, valuable and constructive suggestions and liberal help during this thesis work. I am truly indebted to her for esteemed guidance and encouragement from the beginning to the end of this thesis.

I am profoundly thankful to Dr. Shaestagir Chowdhury, Intel Corporation, USA for his valuable advice and directions that help me a lot to choose the proper direction for the thesis.

I would like to thank Prof. Dr. Samia Subrina, Department of Electrical and Electronic Engineering, BUET, for the support and advice she continues to give me, without which the research work would have become unduly lengthened.

I would like to thank Dr. Mainul Hossain, Department of Electrical and Electronic Engineering, the University of Dhaka for giving the access to the server by which some parts of my theoretical works are done.

I'm also thankful to Dr. Ishtiaque M. Syed, University of Dhaka, University of Dhaka for giving the access to the server by which some parts of my theoretical works are done.

Finally, I would like to thank my family members who support and contribute to me to complete the Degree.

ABSTRACT

Perovskites have emerged as a new superstar in the field of photovoltaics. This group of semiconductors has a wide range of properties that are suitable to be used in a wide range of optoelectronic. The efficiency of perovskite solar cells has greatly increased during the past ten years, and the organic-inorganic hybrid halide perovskite foramidinium lead tri-iodide ($FAPbI_3$) has attained a high efficiency of 25.8%. Commercial use of halide perovskites may revolutionize the field of world photovoltaic and energy due to having cheaper, easily available in nature, easy, rapid and low temperature processing, and more efficient than silicon-based technology. But toxicity and insufficient long-term stability are the main barriers to being used commercially in large-scale applications. Finding stable, non-toxic, Pb-free perovskites is therefore crucial for the advancement of perovskites-based optoelectronic technologies.

Recent studies demonstrated that the stability and toxicity issues can be solved simultaneously by using lead-free, all-inorganic double halide perovskites. This thesis presents a first-principles Density Functional Theory (DFT) investigations of the structural, electronic, optical and mechanical properties and thermodynamic and mechanical stability of Alkaline and Indium based noble inorganic double halide perovskites group Rb_2MInX_6 (where, M= Li, Na and K and X= Cl, Br, I). It is found from this study that Rb_2LiInX_6 perovskites have failed to meet the structural stability criterion imposed by the octahedral factor. First principles study demonstrates that Rb_2KInX_6 have structural, and thermodynamical stability against decomposition but don't have mechanical stability. On the other hand, all the Sodium (Na) based perovskites, Rb_2NaInX_6, have structural, mechanical, and thermodynamical stability against decomposition and show ductile behavior and direct nature in the band gap (3.01 eV for $Rb_2NaInCl_6$ 1.81 eV for $Rb_2NaInBr_6$ and 0.66 eV for Rb_2NaInI_6). $Rb_2NaInBr_6$ and Rb_2NaInI_6 have strong absorption in the visible range and suitable band gap and electron-effective mass for use in solar cells. Additionally, we have found that $Rb_2NaInCl_6$ exhibits strong UV absorption and suitable VBM and CBM energy to function as a photocatalyst in the water-splitting process.

Table of Contents

Table of Figures

Table of Tables

CHAPTER 1: INTRODUCTION

1.1 BACKGROUND

The primary source of energy in the world is fossil fuels. The world is searching for a new, clean and dependable renewable energy source due to the rise in energy demand, as well as the environmental pollution and greenhouse effect of fossil fuels. The most plentiful energy available at hand is without a doubt solar energy. Over 1,500 exawatt-hours of energy comes into the earth in the form of solar rays which is nearly 200 times greater than the sum of all the known reserves of fossil fuel energy (just 9 exawatt-hours) [1]. Less than 0.3% of this energy can meet the world's energy demands. A photovoltaic cell can directly convert solar energy into electrical energy, bypassing all the complicated steps needed for conventional power conversion. However, the cost per unit of energy for solar cells is much higher than the cost of energy from fossil fuels because it is more expensive to produce traditional solar cells like silicon or GaAs [2].

Perovskites have emerged as a new superstar in the field of photovoltaics that can be synthesized rapidly at low temperatures [3]. It has compatible properties for PV applications [4] [5] such as suitable direct band gap, strong absorption in the visible range,[6] [7] low carrier effective masses, high carrier diffusion length, lifetime and mobility [8] [9] [10], defect tolerance and self-regulation [11] [12]. Due to having those properties perovskites are not only used as a solar absorber but also used in the field of photocatalysts [13] [14], white light emitters, LASERs, phosphors [15] [16], photodetectors [14] [17], scintillators [18], memristors [19] and field-effect transistors (FET). A lot of research work and advancement has been done on perovskite solar cells in the last decade and the efficiency increases from the first reported value of 3.8% in 2009 [20] to 25.8% in 2022 [21]. Even though the lead-based hybrid perovskite has very high efficiency, it has poor long-term stability in the ambient environment and the efficiency decreases very rapidly with time [22][23]. The replacement of the organic cation at the A site ($APbX_3$) by inorganic substitution of Cs^+/Rb^+ cations can increase the stability [24] [25] [26], however the toxicity of the Lead cannot be ignored.

To address the long-term stability and toxicity, recent research is focused on the perovskite and perovskite-like structure to find a non-toxic alternative to lead-based perovskites. But it is not easy to find a nontoxic material with long-term stability that still has promising photovoltaic properties.

Different directions have been taken for this purpose. The first direction was the substitution of the Pb^{2+} cation with homovalent cations like Ge^{2+}, Sn^{2+}, etc [27]. But the halide perovskites with Sn and Ge are highly unstable and prone to oxidation in ambient conditions due to having nonbonding valence electrons, ns^2, and oxidized to tetravalent cation from divalent cation [28]. The following direction has been the heterovalent substitution of two Pb^{2+} cations by one single charged (+1) and triple charged (+3) cation to yield the same overall charge balance as the conventional perovskites and formed a new type of materials, halide double perovskite, that have chemical formula unit as $A_2B(I)B(III)X_6$ [29]. Due to having octahedra with two different types of cations, it shows different types of band structures and absorption depending on the nature of the cations. The first known material with this structure was K_2NaAlF_6 which has a cubic structure with an $Fm\bar{3}m$ space group that was first revealed in 1932. A lot of organic-inorganic (hybrid) and all inorganic perovskites have been synthesized successfully and photovoltaic performance has been measured. It is found that all inorganic perovskites overcome the stability problem in hybrid perovskites due to replacing the organic cation at the A site with Cs+/Rb+ which enhances the interaction between those inorganic cations and $[BX_6]^-$ octahedra [25].

All-inorganic perovskites have drawn interest due to these intriguing properties, and ongoing theoretical and experimental research is being done to identify new, promising candidates. Numerous all-inorganic double halide perovskites have been synthesized, and their various applications have been identified. For instance, $Cs_2AgBiBr_6$ perovskite with an indirect nature band value of 1.95 eV and a room-temperature photoluminescence lifetime as high as 660 ns was first synthesized by Slavney et al. [30]. Due to its high light sensitivity and fast responses, it is used as a photodetector. Most recently, its highest efficiency is increased to 6.37% [31] and can also effectively use as the top layer in tandem solar cells. Some other high-stable perovskites like $Cs_2AgBiCl_6$ [32], $Cs_2AgSbCl_6$ [33] and $Cs_2AgInCl_6$ with the same characteristics have also been synthesized [34]. The synthesis of a highly stable direct band gap perovskite, Cs_2NaVCl_6 with strong absorption in the visible-IR range [35] has also been reported. The lists are continually growing and new perovskites with special properties are synthesized, such as $Cs_2NaScCl_6$ exhibiting strong blue emission [36], $Cs_2NaBiCl_6$ that exhibits photoluminescent properties with doping [37] [15], $Cs_2NaInCl_6$ can be used as a LED and phosphor by doping [38] [39].

1.2 RESEARCH PROBLEM

The halide perovskites are still being the developed stage despite the significant amount of research that has been performed in a very short period of time. This is because there are still certain challenges. Low production cost, high efficiency, and notably long-term sustainability are required for the commercial uses of halide perovskites [40]. According to the literature review, it is found that lead halide hybrid perovskites such as $MAPbI_3$ have undergone more exploration than others because of exhibiting excellent power conversion efficiencies (PCEs). The issue with those materials is that they don't offer enough stability and include lead (Pb), which is poisonous and might be dangerous for the environment and human health. According to a recent report, the lifespan of perovskite materials that include iodine may also be shortened by iodine's tendency to self-degrade [22]. Therefore, it is essential to obtain Pb-free perovskites, which have long term stability and could be used for optoelectronic and energy applications. Furthermore, Pb-containing organic-inorganic perovskites $MAPbX_3$ (X = I, Br, Cl) have a low relative dielectric constant. Because of the small dielectric constant, the charge carrier recombination rate enhances and has an impact on the overall performance of solar cells, this is a serious constraint for solar cell applications [41].

Because of the materials' structural instability against moisture, air, and temperature as well as the toxicity of lead, commercializing them on a wide scale remains extremely difficult. Finding sustainable and nontoxic perovskites is essential for the production of perovskite solar cells in the future. By employing carbon encapsulation, multi-cation substitution, and the addition of hydrophobic moieties, the long-term stability problem of the halide perovskites can be addressed [42]. However, replacing Pb with non-toxic elements is the only solution to resolve the toxicity of perovskite materials [43]. But it is not easy to find a nontoxic material with long-term stability that still has promising photovoltaic properties. Different directions have been taken for this purpose. The first direction was the substitution of the Pb^{2+} cation with homovalent cations like Ge^{2+}, Sn^{2+}, etc. But the halide perovskites with Sn and Ge are highly unstable and prone to oxidation in ambient conditions due to having nonbonding valence electrons, ns^2, and oxidized to tetravalent cation from divalent cation.

Both toxicity and stability problems can be addressed simultaneously by inorganic double halide perovskites. In which the heterovalent substitution of two Pb^{2+} cations by one single charged (+1)

and triple charged (+3) cation produces a structure with chemical formula unit $A_2M(I)M(III)X_6$ with the overall same charge as like lead halide perovskite.

1.3 AIMS AND OBJECTIVES

To achieve the goal of this study, the specific objectives can be summarized below:

1. Prediction of the stability of the cubic phase of Rb_2MInX_6 (Where, M= Li, Na and K, and X= Cl, Br, and I) double perovskite by empirical equations.
2. Determining the thermodynamic and mechanical stability of those proposed perovskites.
3. Studying the structural, optoelectronic, thermoelectric, dielectric, optical, and mechanical properties of stable Rb_2MInX_6 perovskites by DFT calculations to find best possible Pb-free inorganic perovskites for photovoltaics and optoelectronics.
4. Determining the suitability of those perovskites to be used as light absorbers in solar cells and used in other applications like Photocatalysts, Light Sensors, Diodes, etc.

1.4 THESIS OUTLINE

In order to develop a stable Pb-free material for photovoltaic and optoelectronic applications, this thesis describes a first-principles density functional theory (DFT) examination of the structural, electrical, optical, transport and mechanical properties of Rb_2MInX_6 perovskites. Herein, all about the thesis.

- Chapter 1 introduces this research including the background of the research topic, current problems and challenges as well as the aims and objectives of this study.
- Chapter 2 presents a literature review explaining the background and current advancement in this field of research. The structure, divisions, characteristics of perovskite materials and broad range of prospective uses for perovskites beyond the photovoltaic is presented. Furthermore, the progress in finding Pb-free perovskites appropriate for photovoltaic devices and optoelectronic devices has also been highlighted in this article. The most recent research studies are also discussed here.

- Chapter 3 contains the theory behind DFT, implementation of DFT and applications of DFT in finding the lattice parameter by finding the equilibrium structure, calculating the density of state and band structure and other properties like dielectric, optical and mechanical.
- Chapter 4 gives a more detailed description of the computational methods employed and parameters used for the first principal study by using the VASP and details about the INPUT files are also discussed.
- Chapter 5 reports the obtained results of the structural, electronic, optical, and mechanical properties of Alkaline and Indium based inorganic double perovskites, Rb_2MInX_6 (Where, M= Li, Na and K, and X= Cl, Br, and I). In this study, this section also focused on the investigations of the stability and fundamental properties of perovskite materials to understand the characteristics of the materials and the possible use of Rb_2MInX_6 perovskites in the field of photovoltaic applications.
- Finally, chapter 6 outlines the main conclusions of the ongoing investigations. It also contains important recommendations for the further advancement of the field by considering the findings of the study.

CHAPTER 2: LITERATURE REVIEW

2.1 CONCEPT OF PEROVSKITE MATERIALS

2.1.1 Perovskite and Perovskite Structure

The material known as perovskite was initially discovered by Gustav Rose in the Ural Mountains of Russia in 1839, is named in honor of von Perovski, a Russian mineralogist and the pioneer and founder of the Russian Geographical Society [44]. A compound that possesses the same structure as the perovskite mineral is known as a perovskite structure or perovskite material. Calcium titanium oxide is the earliest perovskite material to be found ($CaTiO_3$) [45]. However, A perovskite material is a substance that shares the same crystalline structure as a perovskite mineral and has the chemical formula ABX_3, where 'A' and 'B' are two cations of greatly dissimilar radii, and X is an anion that bonds to both of them.

2.1.2 Crystal Structure of Perovskite Materials

Depending on the temperature, the inorganic and organic halide perovskites possess various phases [46]. At high temperature, these materials have a cubic perovskite ABX_3 structure with space group $pm\bar{3}m$ having space group number 221 [47] in which $[BX_6]^{4-}$ form a corner connecting 3D networks. The unit cell contains one formula unit, ABX_3, shown in figure 1-1, where the “A” atoms are positioned at (0, 0, 0) point of the lattice, “B” atoms are positioned at the centered (½, ½, ½) positions and the “X” atoms are at the face centered (½, ½, 0) positions or center of each face plane of the cubic lattice as shown in Figure 2.1.

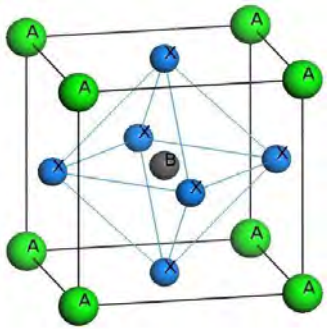

Figure 2-1 Unit cell of cubic ABX3 halide perovskite structure

2.1.3 Classification of Perovskite Materials

Perovskite materials fall into two types based on their chemical composition.

(a) Inorganic Perovskites

(b) Organic- Inorganic or Hybrid Perovskites

When all positions of the unit cell contain inorganic materials/elements are called inorganic perovskites. For example, $CsPbI_3$, $CsSnBr_3$, etc. When the A-site of the perovskite is replaced by an organic cation, it's called Organic- Inorganic or Hybrid Perovskites. The most widely used replacement is methylammonium (CH_3NH_3 or MA) [48]. Some other organic cations like formamidinium ($NH_2CH{=}NH_2$ or FA) is also replaced the inorganic cation to form organic compounds [49] [50]. Initially, hybrid halide perovskite was the center of research interest. Nowadays both organic and inorganic perovskites are investigated intensively.

2.2 PHYSICAL PROPERTIES AND CRITICAL PARAMETERS

Due to having an optical bandgap ranging from 1.48 eV to 2.23 eV, the methylammonium lead trihalide (CH3NH3PbX3, where X is a halogen ion such as I, Br, or Cl) is the most researched perovskite absorber [50]. It ought to be able to achieve better efficiencies since the minimum bandgap is nearer to the ideal value for both single junction and hetero-junction solar cells [50]. The halide concentration of methylammonium lead halides may be controlled to almost cover the visible spectrum and tailor the band gap completely [51]. Additionally, the materials exhibit electron and hole diffusion lengths larger than one micrometer [52]. In fact, W. J. Yin et al. [53] speculate that the materials' lengthy electron-hole diffusion length may be the reason behind their strong optical absorption, low carrier effective masses, and dominating point defects. Additionally, one of the most intriguing characteristics of perovskite materials is sluggish carrier recombination. However, C. Motta et al. suggest that this sluggish carrier recombination may be brought on by molecule rotations, with the subsequent dynamical shift in the band structure [54]. The materials have adjustable structural and compositional characteristics in addition to the fundamental optoelectronic characteristics [55].

2.3 POTENTIAL APPLICATIONS OF PEROVSKITES

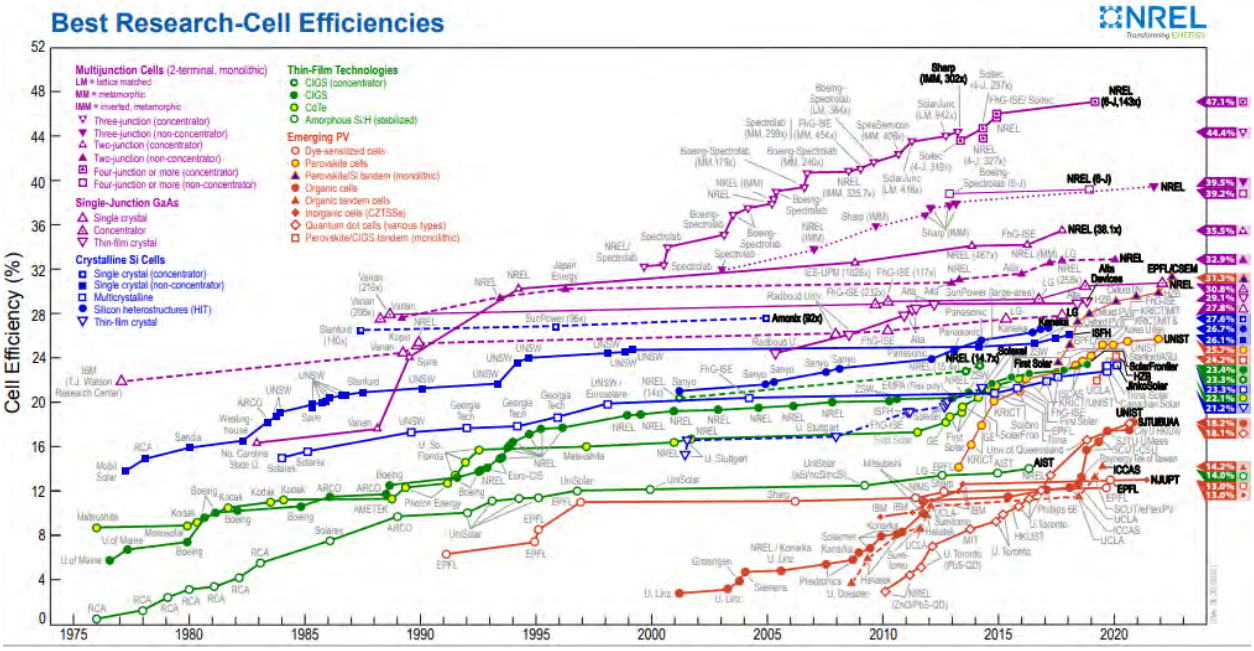

Figure 2-2 Variation of efficiency over time in different solar cell technology [56].

Despite the fact that these perovskite materials have been well-known for many years, it wasn't until 2009 when Miyasaka et al. [20] employed them in solar cells. Miyasaka et al. [20] used a dye-sensitized solar cell model and obtained a power conversion efficiency (PCE) of 3.8% by depositing a thin layer of perovskite onto an electron transport layer, mesoporous TiO_2. But, after a limited period of time, the cell lost its effectivity and decomposed into various binary compounds when it came into contact with moisture. In 2012, Henry Snaith and his co-workers [57] found that the perovskite is stable in contacted with a solid-state hole transporter such as spiro OMeTAD and did not require the mesoporous TiO_2 layer in order to transport electrons. But the high synthesis cost of spiro-OMeTAD gives rise to another problem for commercial applications. After this, a power conversion efficiency (PCE) of 9.7% was found in solid-state mesoscopic heterojunction solar cells employing nanoparticles (NPs) of methylammonium lead iodide $(CH_3NH_3)PbI_3$ as light harvesters in the middle of 2013 [58]. At the same time, Henry Snaith *et al.* [59] found a PCE of 12.3% by planar thin-film architecture and they also found that the ambipolar perovskite transports both holes and electrons, converts the absorbed photons into collected charge with close to 100% efficiency. Using the thin-film architecture with planar geometry, Yang Yang *et al.* [60] found a

PCE of 19.3% and they also claimed that their fabricated perovskite solar cells operated in air and are inexpensive.

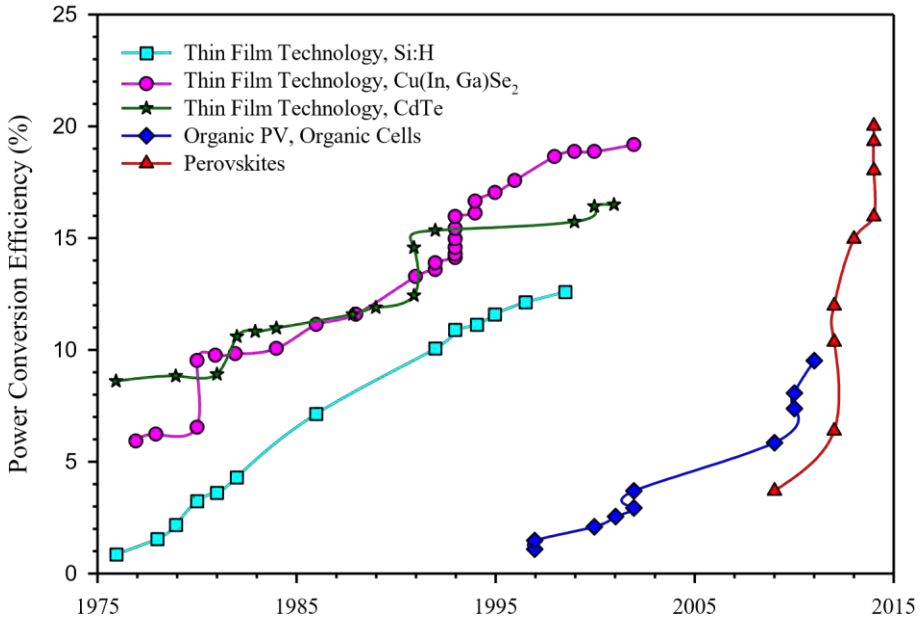

Figure 2-3 The change in Power Conversion Efficiency of perovskite solar cells compared to other types of photovoltaics over recent years. (Data collected from "www.ossila.com").

Researchers from the Swiss Federal Institute of Technology in Lausanne (EPFL) and the Ulsan National Institute of Science and Technology (UNIST) recently claimed to get a record efficiency of 25.7% for a single junction solar cell with [56]. Additionally, Figures 2-3 and 2-4 show that the perovskite solar cell's efficiency is growing quickly in comparison to all other solar cell technologies.

It is commonly believed that a good light absorber may also be a good light emitter, and this idea has encouraged researchers to consider further optoelectronic uses for perovskite materials. In a recent article, J. Chen et al. [61] illustrated all of the potential uses for perovskites as well as their optoelectronic characteristics (Figure 2-5). It is conceivable to produce such materials at the nanoscale, claim Chen et al. [61]. Perovskites, therefore, have promise in a variety of optoelectronic applications, including photodetector, photoluminescence, electroluminescence, light-emitting diodes, lasers, field-effect transistors, and light-emitting electrochemical cells [61]. In addition, these materials' band gaps are easily adjustable throughout practically the whole visible light spectrum, which is crucial for color light-emitting diodes, lasers, and other optoelectronic applications [51].

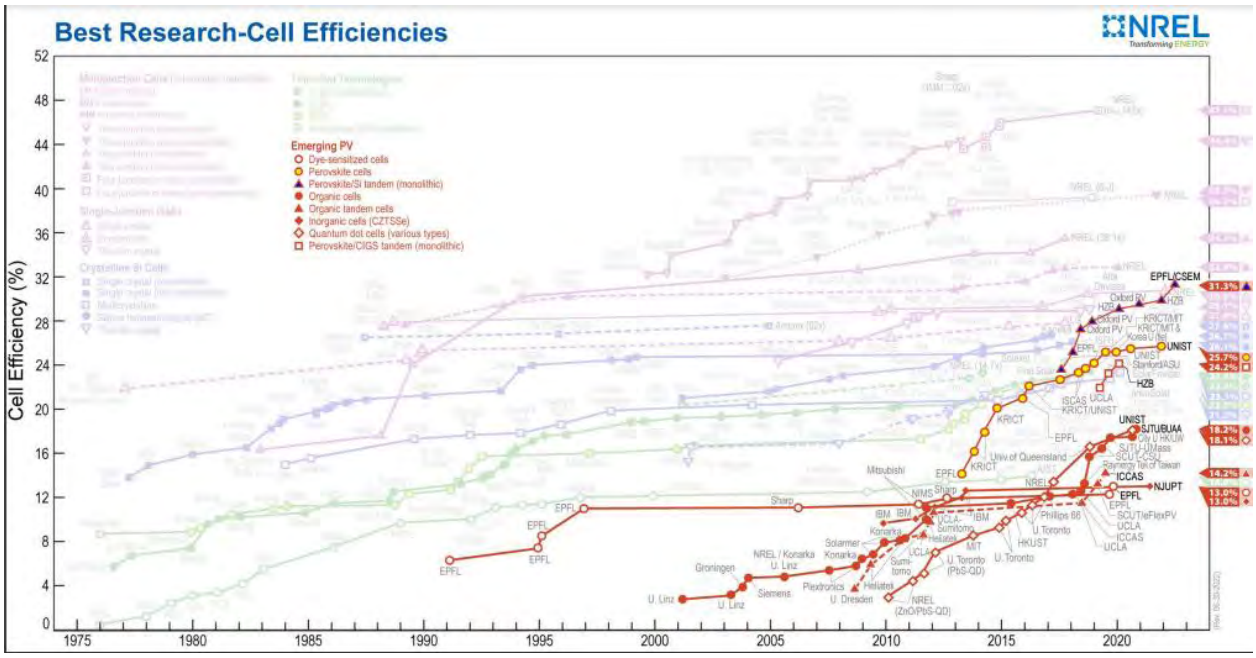

Figure 2-4 The efficiency of emerging PV in recent years [56]

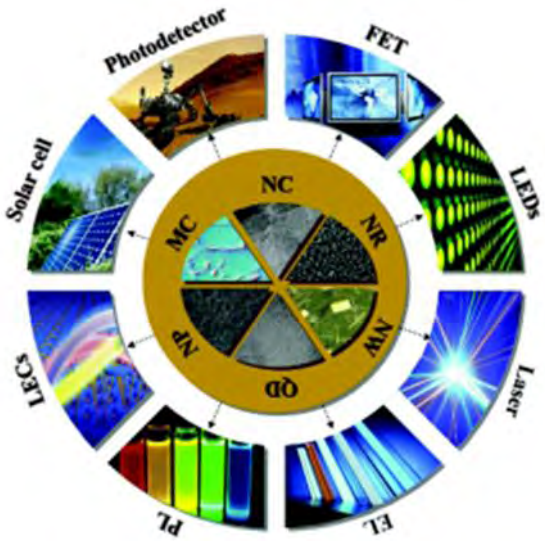

Figure 2-5 Potential optoelectronic properties and applications of typical perovskite ABX3 (acronyms: QD: quantum dots, NW: nanowire, NR: nanorod, NC: nanocrystal, MC: millimeter-scale crystal, NP: nanoparticle, PL: photoluminescence, EL: electroluminescence, LEDs: light-emitting diodes, FET: field-effect transistor and LECs: light-emitting electrochemical cells) .

2.4 DOUBLE PEROVSKITES

2.4.1 Crystal Structure of Double Perovskites

Double perovskites are a novel family of materials that share a crystalline structure with perovskite materials. In perovskite, ABX3, only B forms a 3D network of high symmetric corners connected BX_6 octahedral site. In double halide perovskites, two divalent B ions are replaced by a monovalent and trivalent element and form double perovskite with a formula unit $A_2BB'X_6$, Where A is single valance element and compound which form cation A^+, B is elements with +1 ionic state and B' is elements with +3 ionic state. This belongs to cubic double perovskite groups, which have an $Fm\bar{3}m$ space group. In which two different octahedra, BX_6 formed by B^+ with six surrounding halogens (X) ions and $B'X_6$ formed by B^{3+} with six surrounding halogen s(X) ions, alternate in space to form a corner connecting three-dimensional (3D) networks [62] as seen in Fig. 2-6. Similar to Na^+ and Cl^- in rock salt, one BX_6 octahedron is surrounded by six $B'X_6$ octahedra and vice versa. The A cation has four adjacent octahedra. In the unit cell of double perovskite $A_2BB'X_6$, the A atoms occupy the 8c Wyckoff position with fractional coordinates (0.25, 0.25, 0.25), the B′ atoms occupy the 4a Wyckoff position with fractional coordinates (0, 0, 0), the B″ atoms occupy the 4b Wyckoff position with fractional coordinates (0.5, 0.5, 0.5) and the X atoms occupy the 24e Wyckoff position with fractional coordinates (x, 0, 0)

Those two types of octahedra are formed by two different hetero-charged cations (B^+ and B^{3+}) at the center that have different electronegativity. The bond lengths of B-X and B'-X are different, so they form octahedrons of two different sizes. This reduces the symmetry of the system of double halide perovskite to that of single perovskite, in which only one type of octahedron forms the corner connecting 3D networks.

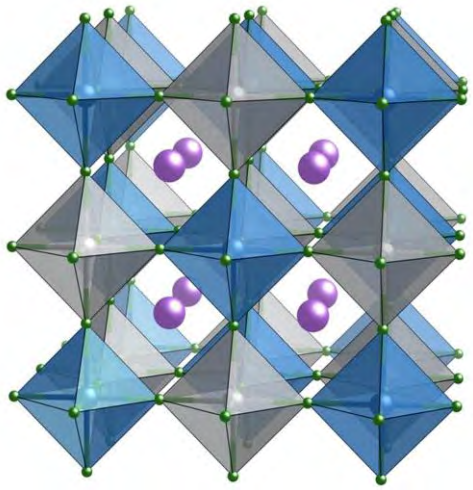

Figure 2-6 Polyhedral model of the conventional unit cell of a double perovskites

2.4.2 Properties and Potential applications of Double Perovskites

Like inorganic and organic-inorganic hybrid perovskites, double perovskite materials are anticipated to exhibit comparable optoelectronic characteristics [63]. In addition, it is anticipated that the materials could possibly escape the toxicity and instability problems related to lead-based organometallic perovskites [64]. As a result, just like perovskite materials, double perovskites have the potency to be used in a variety of applications beyond the solar cells, including the field of LEDs [38-39], photocatalysts [13-14], white light emitters, LASERs, phosphors [16,18], photodetectors [14,15,17], scintillators [18], memristors [19] and field-effect transistors (FET), light-emitting electrochemical cells, and solar-to-fuel energy conversion devices. Despite this wide variety of potential uses, the synthesis and characterization of many halides' inorganic double perovskites (such as Cs2BiAgI6, Cs2BiAgBr6, Cs2BiAgCl6, and Cs2InAgCl6) [64] [66] in addition to halide hybrid double perovskites (such as $MA_2BiAgBr_6$ [67], MA_2BiKCl_6, $MA_2BiTlBr_6$, MA_2KGdCl_6, MA_2KYCl_6) [67] [68] have been reported in the literature. However, most of the investigated compounds either have significant electrical band gap values or have inferior optical characteristics, making the investigated compounds unsuitable for solar use [69]. As a result, it is predicted that researching a wide range of B and B' combinations in $A_2BB'X_6$ may open up prospects to discover an effective alternative to Pb-based halide perovskites in photovoltaics and optoelectronics [43].

2.5 MATERIALS SELECTION

Finding a noble Pb-free, non-toxic perovskites for photovoltaic and optoelectronic applications is the prime objective of the current investigation. Pb from perovskites must be replaced with other appropriate elements in order to accomplish this. A complex substitution of Pb in perovskites can be done by a combination of a trivalent and a monovalent cation to produce a new structure called as double perovskites which can be expressed by the general chemical formula, $A_2BB'X_6$, where A is a relatively large cation (typically Cs+/Rb+), B and B′ are respectively monovalent and trivalent cations, and X is halogen. For instance, the double perovskite Cs_2NaInI_6 is created when the element Pb is removed from the perovskite $CsPbI_3$ and replaced with the trivalent elements In (Indium) and monovalent element Na (sodium). The probable trivalent elements can be scandium (Sc), yttrium (Y), antimony (Sb), Indium (In) and bismuth (Bi), the elements are shown by green colour in the periodic table as shown in Figure 2-7. Also, the probable monovalent elements can be Lithium (Li), Sodium (Na), Potassium (K), copper (Cu), silver (Ag) and gold (Au) and are shown by a red color box and the probable large cation at site A are showed by a blue color in Figure 2-7.

A literature review was done on all the theoretically and experimentally studied perovskites to find out the noble group of perovskites and pencil and sketch method is used to select one group of perovskites that have favorable properties for electronic and photovoltaic application. Direct band gap double perovskite can be identified by pencil and sketch method shown in figure 2-8.

2.5.1 Theoretical and experimental works done on inorganic double perovskites

An intensive literature review has been done on different classes of double perovskites based on the combination of B (I) and B' (III) site materials. Properties of different group of perovskites found from this review and suitable noble perovskite materials can also be identified.

Group-1 and group-13:

Saeed et. al. [70] did a DFT-based study of group-1 and group-13 based double halide perovskites by using the full-potential linearized augmented plane wave plus local orbitals (FP-LAPW+lo) method based on the WIEN2k code. They employed generalized gradient approximation (WC-

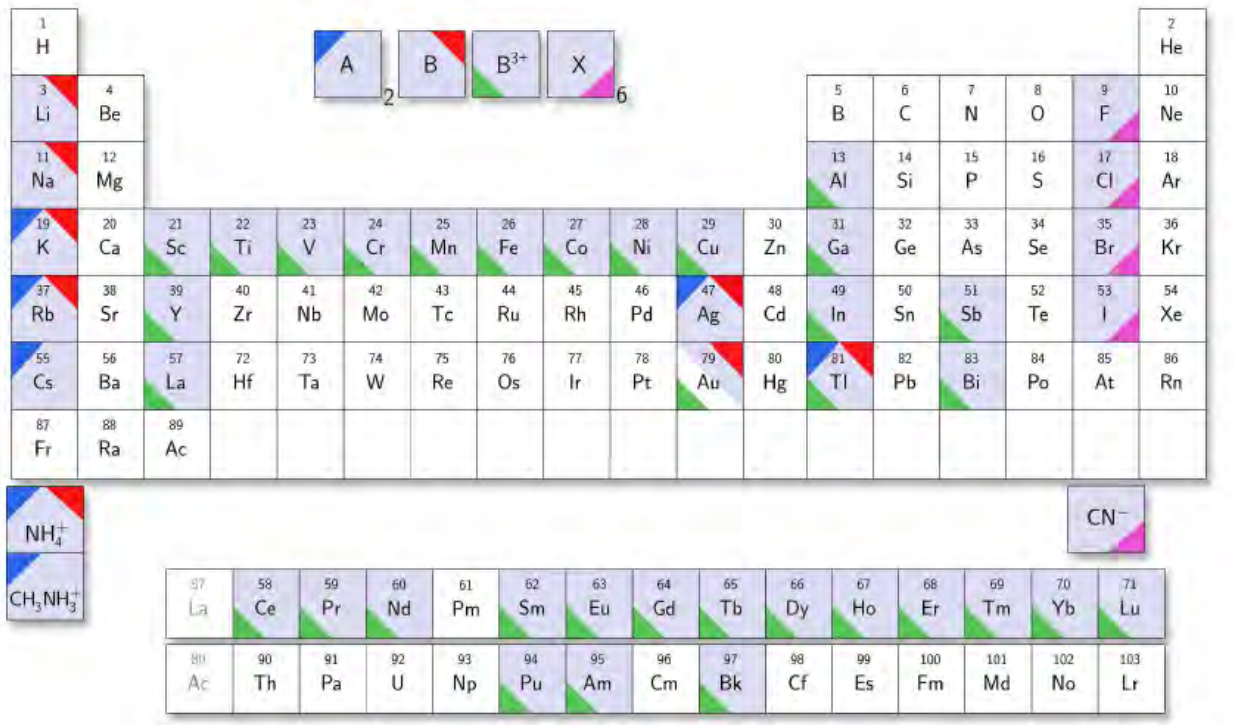

Figure 2-7. Periodic table showing the possible trivalent (blue boxes) and monovalent (red box) elements to form double perovskite structure because of the replacement of Pb from perovskite by complex substitution.

Orbitals		Prediction	
B	B'	VBM	CBM
s	*s*	Γ	Γ
p	*p*	Γ	Γ
$d_{x^2-y^2}/d_{z^2}$	$d_{x^2-y^2}/d_{z^2}$	Γ & X	Γ & X
s	*p*	L	L
s	$d_{x^2-y^2}/d_{z^2}$	X	X
p	$d_{x^2-y^2}/d_{z^2}$	–	–
s	null	X	Γ
p	null	L	L
$d_{x^2-y^2}/d_{z^2}$	null	Γ & X	X
null	null	Γ & X	–

Figure 2-8 Expected k-point location of conduction band minimum and valance band maximum for all the possible combinations of B and B' orbitals.

GGA) to calculate electronic and thermodynamic properties. To find a more accurate band gap they employed modified Becke–Johnson (mBJ) schemes [71]. It is found from this study that $Cs_2LiAlBr_6$, $Cs_2NaAlBr_6$, $Cs_2LiGaCl_6$, $Cs_2LiGaBr_6$, $Cs_2NaGaCl_6$, $Cs_2NaGaBr_6$, $Cs_2LiInBr_6$ and $Cs_2NaInBr_6$ have band gap value in the range of 0.8 eV to 2 eV in WC-GGA approximation calculation. For this class of materials, VBM is consist of from X-p orbital and at CBM, X and M'(III) jointly contribute [71].

For this group of materials, the band gap value is decreasing with increasing the ionic size of the halide due to uplifting the VBM level with walking from Cl to Br to I. This uplifting is resulted from the increasing the energy of X-p orbital from Cl to Br to I. The energy of s orbital increases when walking from Na to K to Rb and so this lifting up the CBM. But when going from Na to K to Rb, the B^+X_6 also increases due to increasing ionic radii that shrinks B^{3+} octahedral, promoting enhanced coupling between the p orbital of X and s orbital of B'(III). Thus, the evolution of VBM, depending on the relative enhancement band gap can increase or decrease [10]. The band gap values of $Cs_2LiGaBr_6$ and $Cs_2NaGaBr_6$ are much lower than the compounds of this class of materials and so further calculations with SOC+ mBJ are done to find more accurate band gap values and found a value of 1.97 eV for $Cs_2LiGaBr_6$ and 1.76 eV for $Cs_2NaGaBr_6$. And so, we can say that band gap values are very much underestimated in the calculation without SOC+mBJ and so all the materials other than $Cs_2LiGaBr_6$ and 1.76 eV for $Cs_2NaGaBr_6$ have band gap values more than 2 eV and will go to out of consideration for photovoltaic applications.

A low carrier effective mass is required for photovoltaic devices. The calculated effective masses of Cs_2Li (Na)$GaBr_6$ are 0.154 (0.176) and 0.176 (0.186) for m_e* and m_h* respectively [71] that is comparable to $MAPbI_3$ and very good transport properties. Both selected materials are mechanically stable and have good absorption coefficient in the visible range [71]. But $Cs_2NaGaBr_6$ has a higher absorption coefficient value and band gap value closer to the ideal than $Cs_2LiGaBr_6$.

Group-3 and Group-13:

Noor et. al. [72] did a DFT based studies of Rb_2ScInI_6 and Cs_2ScInI_6 double halide perovskites by using the full-potential linearized augmented plane wave plus local orbitals (FP-LAPW+lo) method based on the WIEN2k code. They optimized the structure by using generalized gradient approximation (PBEsol-GGA) method and further employed modified Becke-Johnson (mBJ) plus

SOC schemes were brought into use over PBEsol-GGA to find more appropriate band gap values. They find that both compounds have a band gap in the suitable region for photovoltaic applications [72]. From the dos calculations, we find that 3d orbitals of Scandium and 5p orbitals of Iodine are main contributor at the edge of valance band maxima and 3d orbitals of Scandium and 5p orbitals of Indium are main contributor at the edge of conduction band minima.

Both materials also meet the goldsmith tolerance factor, have negative formation enthalpy and is mechanically stable [72] according to the criteria set by Born [36]. Both materials have high absorption coefficient in both IR and visible range and band gap lies in the range of effective photo voltaic range. So, both materials have potential to be used in solar cells. Cs_2ScInI_6 is more stable, has higher ductility than Rb_2ScInI_6. Cb_2ScInI_6 also has a band gap value relatively closer to ideal than Rb_2ScInI_6 [72]

Group-11 and Group-13:

Zhao et al. [32] theoretically calculated the potentiality of perovskites in this group to be used in solar cell as a light absorber. They calculated the band gap of those 36 candidates by using VASP code with the Heyd-Scuseria-Ernzerhof (HSE) hybrid functional approach with a standard 25% exact Fock exchange included. They screened those compounds with adopting $0.5 < Eg < 3.0$ and Decomposition enthalpy (ΔHd) >0 found only six compounds $Cs_2AgInCl_6$, $Cs_2AgInBr_6$, $Rb_2CuInCl_6$, $Rb_2CuInBr_6$, $Rb_2AgInCl_6$ and $Rb_2AgInBr_6$ fulfilled those conditions.

Yao et al. [73] did a high throughput computational study to make a database on inorganic double halide perovskite employing HSE-06 and GGA-PBE DFT methods using PAW method employed in VASP package. They also calculate spectroscopic limited maximum efficiency (SLME) and suggest the materials that has theoretical efficiency greater than 10%. They suggest $Rb_2AgInBr_6$ with efficiency 23.4%.

Wang et al. studied on $Cs_2BB'Br_6$ (B = Cu, Ag, and Au; B′ = Ga, In, Sb, and Bi) and measure HSE band gaps. They also calculated formation energy and decomposition energies. From all of those analyses, they suggest 2 compounds, $Cs_2AgGaBr_6$ and $Cs_2AgInBr_6$, which has thermodynamic stability, negative energy of formation and band gap value in between 0.8-2.0 eV with direct in nature.

Tang et al. [74] theoretically investigated the electronic, optical, and mechanical properties of A_2AgAlX_6 (where A = K, Rb, Cs, and X= Cl, Br, I) double perovskite. Band gaps are calculated by using CASTEP based on Materials Studios software with the Heyd-Scuseria-Ernzerhof (HSE) hybrid functional approach. All those compounds, $Cs_2AgAlCl_6$, $Cs_2AgAlBr_6$, $Rb_2AgAlBr_6$ and $K_2AgAlBr_6$ show band gap value greater than 2 expect Cs_2AgAlI_6 (Eg = 0.773ev) but this has positive formation enthalpy [74]. So, none of those are potential materials for single-junction solar cells.

In this class of materials, VBM consists of dominantly by p orbital of X (halogen) with d orbitals of B(I) [75]. Conduction band minima (CBM) consists of predominately by s-p orbitals of B' (III) with the p orbitals of X formed by an antibonding nature [76]. Cs or Rb has very little effect in VBM and almost no effect in CBM. In this class of materials, Ag containing materials has larger band gap value than Cu and Au due to having lowest energy d orbitals and VBM is driven from hybridization between Cu/Ag/Au-d and X-p orbitals [77]. In this class of materials, $Cs_2AgAlCl_6$ has largest band gap due to having shallow Al-s state, that leads to strong hybridization of Al-Cl and so form antibody state with high energy level that increase the CBM at high energy. From Cl to Br to I, these interactions weaken and so CBM decreases to lower level and so band gap decrease from Cl to Br to I [74]. And band gap trends for B'(III) shows that band gap values for similar perovskite is Al > In, Ga > Tl.

All the perovskite in this group has indirect band gap due to having same electronic configurations, electronic configuration of B(I) and B'(III) are $d^{10}s^0$ and $d^{10}s$ respectively [73].

It is found that $Cs_2AgGaBr_6$, $Rb_2CuInCl_6$, $Rb_2AgInBr_6$, and $Cs_2AgInBr_6$ have direct band gaps values within the range of 0.8-2 eV. But xiao et. al. found that $Rb_2CuInCl_6$ and $Rb_2CuInBr_6$ have negative decomposition energy, so those are not stable. No Cu+ double perovskite is stable even though double perovskite with Ag+ is synthesized experimentally. This is because of having a much higher energy level for Cu $3d^{10}$ orbital than Ag $4d^{10}$ orbital and so Cu does not favor to form 6-fold coordination required for $[Cu(I)X_6]$ octahedron [78]. With theoretical analysis, xiao et. al. has tried solid-state synthesis of $Cs_2CuInCl_6$ and $Cs_2CuInBr_6$ but failed to synthesize experimentally and found a mixture of 4-fold coordinated $CsCu_2X_3$ with $Cs_3In_2X_9$ [78].

The experimental band gap of $Cs_2AgTlCl_6$ and $Cs_2AgTlBr_6$ are 2.0 and 0.95ev respectively [79] and theoretical band gap of $Rb_2AgTlCl_6$ is 0.78eV [80]. $Cs_2AgTlBr_6$ has great potential for solar application due to having a small band gap, small effective carrier mass, long carrier lifetimes, and good charge carrier mobility [79]. But Thallium is a highly toxic material and compounds containing Thallium have restricted use only.

So, form this class of perovskite $Cs_2AgGaBr_6$, $Rb_2AgInBr_6$, and $Cs_2AgInBr_6$ can be used as a potential candidate in solar cell due to having band gap close to the ideal value. Theoretical efficiency of $Rb_2AgInBr_6$, and $Cs_2AgInBr_6$ also show above 20%.

Group-1 and Group-15:

Zhao et al. have done first principal study of $Cs_2B(I)B'(III)X_6$ (where B = Na, K and Rb, B'= Sb and Bi X = F, Cl, Br and I) to find out band gap, electron and hole mobility, binding energy and formation enthalpy by employing the HSE hybrid functional containing 25% of the exact Fock exchange [77].

For this class of perovskites, VBM is derived from anti-bonding state between the p orbital of X and s orbital of M'(III). Due to the reduced symmetry in double perovskite than single perovskite, having octahedral sites with 2 different types of atoms in the center, the p-s coupling at the W point and X point is higher than Gamma point and VBM located at Gamma point is in lower position than X and W. And so VBM located at W point instead of Gamma point. Main contributors at CBM are unoccupied s orbital of M(I) (Alkaline metals), p orbital of Cl and p orbital of M'(III). The energy of s orbital increases when walking from Na to K to Rb and so lifting the CBM. But when going from Na to K to Rb, the M^+X_6 also increases due to increasing ionic radii that shrinks M^{3+} octahedral, promoting enhanced coupling between the p orbital of X and s orbital of M'(III) and thus the evolution of VBM. Depending on the relative enhancement band gap can increase or decrease [77]. Band gap decreases when walking from Cl to Br to I both for Sb and Bi due to increasing the energy of X-p orbital that lifting up the VBM at higher level [77]. But Bi has a slightly higher band gap than identical perovskite of Sb due to lower energy of Bi 6s orbital than Sb 5s orbital coming from the mass-Darwin relativistic effect. But all the Group-11 gropu-13 perovskite has higher band gap and higher hole effective mass that is incompatible for the photovoltaic applications. So, none of those perovskite are suitable for using in solar cell.

Group-11 and Group-15:

Bi^{3+} has stable $6s^2$ $6p^0$ electronic configuration like Pb^{2+}. So, Bismuth has great potential to be a nontoxic replacement of Pb based perovskite light absorber in PV device.

Zhao et al. [77] did the first principal study of $Cs_2BB'X6$ (where B' = Sb and Bi, B = Cu, Ag, and Au, and X = F, Cl, Br, and I) to find suitable PV materials. They have found $Cs_2CuSbCl_6$, $Cs_2CuSbBr_6$, $Cs_2CuBiBr_6$, Cs_2CuBiI_6, $Cs_2AgSbBr_6$, Cs_2AgSbI_6, Cs_2AgBiI_6, $Cs_2AuSbCl_6$, $Cs_2AuBiCl_6$ and $Cs_2AuBiBr_6$ suitable band gap for light absorption (0.8 eV < Eb < 2.00 eV), standard effective mass beneficial for ambipolar carriers' conduction and easy carriers' extraction (both electron and hole effective mass less than 1.0 m0) and suitable exciton binding energy (<100eV). Cs_2CuBiI_6 has positive formation enthalpy so it will be excluded from the list [77].

But unfortunately, all those compounds have indirect band gap [77] [81] due to having different electronic configurations resulting mismatch in symmetry, electronic configuration of B(I) and B'(III) are $d^{10}s^2$ and $d^{10}s^2$ respectively [73][81]. The VBM is mainly derived from the anti-bonding hybridization between the d orbital of M(I) and p orbital of X, the s orbital of M'(III) has also minor contribution. The orbital mismatch between the M(I)-d and M'(III)-s orbital reduces the electronic symmetry and resulting in large off-center p-d coupling that moves the VBM from Gamma point to the X point and so the position of CBM and VBM located at different k-point. The CBM is mainly derived from the hybridization among the p orbital of M'(III), p orbital of X and s orbital of M(I). In this class of materials, Ag+ containing materials has highest band gap values due to having d orbital with lowest energy that lowered the position of VBM at lower level and Au+ containing materials has lowest band gap values due to having d orbital with highest energy that uplifting the position of VBM at higher level. The band gap Cu+ has intermediate between two due to having intermediate energy of d orbital. Band gap decreases when walking from F to I both for Sb and Bi due to increasing the energy of X-p orbital that lifting up the VBM at higher level [77].

Indirect band gap has lower power conversion efficiency due to having involve of phonon with photon during PV conversion and so require higher thickness compared to direct band gap materials to absorb sufficient solar energy for PV applications. Filip et al. has studied Phase Diagrams and Stability of those group-11 and group-15 double perovskite. Among those perovskites they found only $Cs_2AgBiBr_6$ is stable and inconclusive about $Cs_2CuSbCl_6$ and

$Cs_2AgSbBr_6$. But 2 inconclusive perovskite $Cs_2CuSbCl_6$ and $Cs_2AgSbBr_6$ have synthesized experimentally [83] and so be stable. Stability of $Cs_2AgBiBr_6$ validated by synthesizing experimentally [84]. The instability of $Cs_2CuBiBr_6$, Cs_2CuBiI_6 and Cs_2AgBiI_6 have also been found by Xiao et. al. [78]. Instability of $Cs_2SbAgBr_6$ also supported by experimental work [85]. Even though theoretical results show the instability of Cs_2AgBiI_6 but colloidal nanocrystal of this have been synthesized by Creutz et al.

Group-13 and Group-15:

Zhao et al. have done first principal study of $Cs_2B(I)B'(III)X_6$ (where B = In and Tl, B'= Sb and Bi X = F, Cl, Br and I) to find out band gap, electron and hole mobility, binding energy and formation enthalpy by employing the HSE hybrid functional containing 25% of the exact Fock exchange [77]. They have found that $Cs_2GaSbCI_6$, $Cs_2GaBiCI_6$, $Cs_2GaBiBr_6$, Cs_2InSbI_6, $Cs_2InBiCl_6$, $Cs_2TlSbCl_6$, $Cs_2TlSbBr_6$, Cs_2TlSbl_6, $Cs_2TlBiCl_6$, $Cs_2TlBiBr_6$, Cs_2TlBil_6 have compatible band gap, electron, and hole effective mass required for an efficient solar cell [77]. The promising photovoltaic properties in the case of In come from the high-energy-lying unoccupied $5s^2$ orbital. But this $5s^2$ orbital must be unstable against oxidation and decomposition. Xiao et. al. [64] has theoretically found that In^{2+} easily oxidized to In^{3+} by Sb or Bi [64].

In this class of perovskite, both B(I) and B'(III) have a similar electronic structure with an outermost cell of unoccupied s orbital like Pb^{2+} ion in $APbX_3$ perovskite. The band edge of this perovskite is also quite similar [53]. VBM is located at Gamma points due to not reducing the electronic symmetry because of having the same electronic configurations of both B(I) and B'(III) [86]. The electronic configuration of B(I) and B'(III) are $d^{10}s^2$ and $d^{10}s^2$ respectively. So, all the perovskite in this group has a direct band gap due to having the same electronic configurations [40]. The VBM is mainly derived from the anti-bonding hybridization between the s orbital of B(I) and the p orbital of X and The CBM is mainly derived from the hybridization among the p orbital of B(I), the p orbital of B'(III) and p orbital of X. The effective carrier mass of both electron and hole is smaller due to large dispersion of both VBM and CBM resulting in strong delocalization of wave-function of the band edges that are good for carrier extraction.

From this review, it is found that group-1-group-13, group11-group-13 and group-13-group-15 have direct band gap due to having the same electronic configuration. It is found that a group of direct band gap perovskite, Rb_2MInX_6, from group-1-group-13 still remains unexplored. The properties of similar types of perovskites, based on Cesium, were not only explored theoretically but also experimentally, and found that those have suitable properties for optoelectronic and photovoltaic applications.

CHAPTER 3: THEORY

This chapter contains a brief history of quantum mechanics and an overview of the fundamental of density functional theory (DFT). In addition to that implementation of those theory for practical purposes will also be discussed. Some of those theories will be utilized in the thesis.

3.1 A BRIEF HISTORY OF QUANTUM MECHANICS

Due to the effort of the greatest physicists, the most significant concepts of classical physics were discovered and advanced to a high level of complexity by the end of the nineteenth century. The start of the 20th century was an exciting time for revolutionary discoveries that had a major influence on the fields of physics, chemistry, and biology as well as engineering and technology. This revolution was sparked by the development of the theory of relativity and quantum mechanics, which together make up what is now known as contemporary physics. Modern physics has fundamentally changed the way we perceive the world. Quantum mechanics was first established to provide better understanding on the behavior of systems at atomic and subatomic scales, particularly the light spectra radiated by various atomic species. After many years of progress, quantum mechanics now not only has a significant impact on physics but also has a wide range of uses in chemistry.

The charge and mass of the electron were determined in 1897 by British physicist Joseph John Thomson, who carried out a forerunner of Millikan's well-known oil drop experiment. The investigation did reveal that a subatomic particle exists that is significantly lighter than the lightest atom, even though his estimations of charge and mass had almost 50% error.

In 1877, Ludwig Boltzmann proposed that a physical system's energy levels might be discrete, following Gustav Kirchhoff's investigation of the black body radiation problem in 1859. The discrete energies of the black body were finally given a mathematical expression by German scientist Max Planck in 1900:

$$\varepsilon = nh\nu \quad \ldots\ldots\ldots\ldots 3.1$$

Where, h is a constant, v is the frequency, and n is an integer. However, most scientists at the time rejected Planck's idea as being too radical. A few years later, in 1905, Einstein used Plank's notion to describe the photoelectric effect and came up with an estimate of h that was remarkably similar to Planck's estimate. He went on to demonstrate in 1907 that atoms' mechanical vibrations within crystals are similarly quantized. The concept of a quantization condition has now evolved into a contentious concept. Niels Bohr created a hydrogen atom model that was well-congruent with the line spectrum in an attempt to describe it. Bohr's hypothesis, however, was unable to be properly expanded to account for some phenomena, such as the spectrum that results from a magnetic field. In 1923, de Broglie postulated that electrons and other particles have waves associated with them and the wavelength is given by:

$$\lambda = \frac{h}{p} \quad \ldots\ldots\ldots \quad 3.2$$

where p is the momentum of the particle. George Paget Thomson provided the first experimental evidence of the electron acting like a wave in 1926. In 1926, Schrödinger discovered a wave equation that describes the behavior of atomic and subatomic particles as they were revealed to exhibit both particle-like and wave-like characteristics.

One of the most fundamental equations in quantum mechanics is the Schrödinger's equation. The solution of this equation is called wavefunction. The fundamental equation for a single particle is as follows:

$$i\hbar \frac{\partial}{\partial t}\Psi(r,t) = \hat{H}\Psi(r,t) = -\frac{\hbar^2}{2m}\nabla^2\Psi(r,t) + V(r)\Psi(r,t) \quad \ldots\ldots\ldots \quad 3.3$$

where $\Psi(r,t)$ is the wavefunction, r is the position in three-dimensional space, $\hat{H}$ is the Hamiltonian operator, m is the mass and V(r) is the potential at point r. The time independent Schrödinger's equation can be written as:

$$E\psi(r) = -\frac{\hbar^2}{2m}\nabla^2\psi(r) + V(r)\psi(r) \quad \ldots\ldots\ldots \quad 3.4$$

There was a statement that chemistry has finally come to an end since all of the chemistry could be completely included in the powerful equation immediately after Schrödinger's equation for the electronic wavefunction was proven for basic tiny systems like H_2 and the many-electron atom He. The quantum mechanical equation is typically far too complex to be solved precisely, therefore

obtaining a good approximation to Schrödinger's equation became a natural and simple answer. In fact, the whole science of computational chemistry was founded on approximations in the decades after the discovery of Schrodinger's equation. While some of these solutions are rather rudimentary, others are anticipated to be more precise than any previous experiment. The key to selecting a method is understanding each assumption and how precise the findings have to be. For generating incredibly exact findings, supercomputers or other extremely powerful computers are often required. In generally, the calculation costs increase with the size of the system (more particles).

3.2 DENSITY FUNCTIONAL THEORY

Over the past few decades, density functional theory (DFT) has become the most widely used method in the field computational physics and quantum chemistry for the determining the stability, properties and characteristics of materials and designing potential new materials. That can be use not only for the simple bulk system but also more complex structure like nano particles, nano-flowers, nano-sheets, interphases, etc. DFT uses particles' density of many bodies interacting system instead of the many body wavefunctions that makes the system of 3N degree of freedom of N body system to system of only 3 degrees of freedom through three spatial coordinates of its particle density. And so, the computation becomes less vigorous and can be done easily without much time consuming. It stands on the basis of the Hohenberg–Kohn theorems [87], the first theorem states that 'the ground state of any interacting many particle system with a given fixed inter-particle interaction is a unique functional of the electron density n(r)' and the second Hohenberg–Kohn theorem defines an important property of the functional and states that 'the electron density that minimizes the energy of the overall functional is the true electron density corresponding to the full solutions of the Schrödinger equation'. Together with the Born-Oppenheimer (BO) approximation [88] and Kohn-Sham (KS) ansatz [89], DFT analysis can be done preciously by taking appropriate exchange correlation (XC) potential. XC potential states the effects of the Pauli principle and the Coulomb potential beyond a pure electrostatic interaction of the electrons. The exact value of XC potential cannot determine accurately.

With improved approximations for the XC energy functional during the 1990s, the results of DFT calculations for the systems often coincided pretty adequately with experimental results. Additionally, compared to earlier approaches that relied on the complex many-electron wavefunction, such Hartree-Fock theory [90] [91], the computing costs were comparatively modest. The use of DFT to accurately describe intermolecular interactions, charge transfer excitations, transition states, global potential energy surfaces, some other strongly correlated systems, and calculations of the band gap of some semiconductors remains challenging despite advancements in the technique.

3.2.1 The Many-Body System and Born-Oppenheimer (BO) Approximation

The key of the many body problem is the coulombic interaction between the atomic nuclei and electrons of the system. Hamiltonian of a many-body system can be expressed as:

$$H_{tot} = -\sum_{I} \frac{\hbar^2}{2M_I} \nabla_{R_I}^2 - \sum_{i} \frac{\hbar^2}{2m_e} \nabla_{r_i}^2 + \frac{1}{2} \sum_{\substack{I,J \\ I \neq J}} \frac{Z_I Z_J e^2}{|R_I - R_J|} + \frac{1}{2} \sum_{\substack{i,j \\ i \neq j}} \frac{e^2}{|r_i - r_j|} - \sum_{\substack{I,j \\ I \neq j}} \frac{Z_I e^2}{|R_I - r_j|}$$

… …. … 3.5

where the indexes I, J run on nuclei, i and j on electrons, R_I and M_I are positions and masses of the nuclei, ri and me of the electrons, Z_I the atomic number of nucleus I. The first two terms stand respectively for the kinetic energy of nuclei and electrons and the remaining three terms for the potential energy. 3rd term represents the coulombic interaction between the nuclei, 4th term represents the coulombic interaction between the electrons and the last one for the potential energy of nucleus-electron Coulomb interaction. The time-independent Schrodinger equation can be expressed as:

$$H_{tot}\, \psi\, (\{R_I\}, \{r_i\}) = E \psi\, (\{R_I\}, \{r_i\}) \; \ldots \ldots \ldots 3.6$$

where $\psi\, (\{R_I\}, \{r_i\})$ is the total wavefunction of the system. Everything of a system can be determine by solving this equation. The properties of small system with one or two electrons can be identified by solving this. Large system with more particles, however, is practically impossible to solve this equation. A so called Born-Oppenheimer (BO) [88] approximation was proposed by

Born and Oppenheimer [88] in 1927. In which it is assumed that the position of nucleus can be taken as fixed due to having much slower movement of nucleus compared to the electron. Thus, the total wavefunction can be represented as:

$$\psi\left(\{R_I\},\{r_i\}\right) = \Theta(\{R_I\})\emptyset(\{r_i\};\{R_I\}) \quad \ldots\ldots\ldots 3.7$$

where Θ({RI}) represent the nuclei and φ({ri}; {RI}) the electrons. By using Born-Oppenheimer (BO) time-independent Schrodinger equation can be divided into two Schrödinger equations those are given below:

$$H_e\ \emptyset(\{r_i\};\{R_I\}) = V(\{R_I\})\emptyset(\{r_i\};\{R_I\}) \quad \ldots\ldots\ldots 3.8$$

Where,

$$H_{tot} = -\sum_i \frac{\hbar^2}{2m_e}\nabla_{r_i}^2 + \frac{1}{2}\sum_{\substack{I,J \\ I\neq J}} \frac{Z_I Z_J e^2}{|R_I - R_J|} + \frac{1}{2}\sum_{\substack{i,j \\ i\neq j}} \frac{e^2}{|r_i - r_j|} - \sum_{\substack{I,j \\ I\neq j}} \frac{Z_I e^2}{|R_I - r_j|}$$

$$\ldots\ldots\ldots 3.9$$

And

$$\left[-\sum_I \frac{\hbar^2}{2M_I}\nabla_{R_I}^2 + V\left(\{R_I\}\right)\right]\Theta\{R_I\} = E'(\{R_i\})$$

$$\ldots\ldots\ldots 3.10$$

Eq. is purely for the electronic problem with fixed nuclei positions. The eigenvalue of the energy $V\left(\{R_I\}\right)$ depends on the positions of the nuclei. The value of $V\left(\{R_I\}\right)$ can be determined by solving the eq. 8 and we can construct the Hamiltonian for the nuclei,

$$H_n = -\sum_I \frac{\hbar^2}{2M_I}\nabla_{R_I}^2 + V(R_I)$$

$$\ldots\ldots\ldots 3.11$$

By separating the movement of electrons from the nuclei, BO approximation enables to think the movements of electrons in a static external potential $V_{ext}(r)$ formed by the nuclei. This is the beginning of new computational theory, DFT.

Bohn and Huang expanded the BO approximation, that is widely known as Born-Huang (BH) approximation [6]. That allows more nonadiabatic effects in the electronic Hamiltonian than in BO approximation.

3.2.2 Thomas-Fermi-Dirac Approximation

Thomas-Fermi (TF) model proposed by Thomas [92] and Fermi [93] was the antecedent of the DFT in which electron density n(r) is used as a basic variable instead of wavefunction. In a field of external applied potential $V_{ext}(r)$, total energy of a system can be expressed as a functional of the electron density n(r). The potential of the frozen nuclei can also be assumed as the external applied potential $V_{ext}(r)$ and this can be written as:

$$E_{TF}[n(r)] = A_1 \int n(r)^{\frac{5}{3}} dr + \int n(r)\, V_{ext}(r) dr + \frac{1}{2} \int\int \frac{n(r)n(r')}{|r-r'|}\, dr dr' \quad \ldots\ldots\ldots 3.12$$

First term contains the kinetic energy of non-interacting electron in a homogeneous electron gas (HEG). Where,

$$A_1 = \frac{3}{10} (3\pi^2)^{3/2} \ldots\ldots\ldots 3.13$$

The kinetic energy of a HEG is found by summing up all of the energy state of free-electron $\varepsilon_k = k^2/2$ upto the fermi wavevector $kF = [3\pi^2 n(r)]^{2/3}$. The second one represents the interactions between electron-nucleus. The last one is the interaction among the electrons or the Hartree energy.

Dirac added a new term to this equation in 1930 [9], that is known as local exchange term and the equation have taken the new form as:

$$E_{TF}[n(r)] = A_1 \int n(r)^{\frac{5}{3}} dr + \int n(r)\, V_{ext}(r) dr + \frac{1}{2} \int\int \frac{n(r)n(r')}{|r-r'|}\, dr dr' + A_2 \int n(r)^{4/3} dr$$

$$\ldots\ldots\ldots 3.14$$

At this moment, the ground state density and so the ground state energy of the system can be determined by minimizing the total energy under the normalized conditions. The solution at the stationary condition can be determined by using the Lagrange multipliers techniques:

$$\delta\{E_{TFD}[n(r)] - \mu(\int n(r) dr - N)\} = 0 \ldots\ldots\ldots 3.15$$

Where, μ is constant that termed as Lagrange multiplier, the physical meaning of this is the chemical potential (or Fermi energy at T=0 K). That makes the Eq. 14 to ThomasFermi-Dirac equation,

$$\frac{5}{3}A_1\, n(r)^{\frac{2}{3}} + V_{ext}(r) + \int \frac{n(r')}{|r-r'|}\, dr' + \frac{4}{3}\, n(r)^{4/3} - \mu = 0$$

… …. … 3.16

The ground state density can be determined directly by solving this.

The Thomas-Fermi-type approach has a lot of issues with the most serious one is the failing to describe the bonding of atoms in molecule. Thus, according to this model the molecules and solids are not the practical things. Although it falls short of adequately describing electrons in matter, the idea of using electron density as the fundamental variable serves to demonstrate how DFT operates.

3.2.3 The Hohenberg-Kohn (HK) Theorems

Hohenberg and Kohn [86] demonstrated the accuracy of DFT as a theory of many-body systems in 1964. Instead of being used only on the condensed matter system with fixed nuclei, this can be applied more generally to any system of interacting particles in an external potential $V_{ext}(r)$. The theory consists of two theorems that makes the backbone of DFT.

3.2.3.1 The HK theorem I:

In any system of interacting particles, the external potential $v_{ext}(r)$ is uniquely determined (up to a constant) by the ground state particle density $n_0(r)$ [86].

With the exception of a constant energy shift, the whole Hamiltonian is determined by the ground state particle density. Th ground and excited states as well as all other states of the many-body wavefunctions are theoretically calculable. This indicates that every characteristic of the system is entirely determined by the ground state particle density.

Proof of the HK theorem I:

For avoiding the complexity, the ground state of the system is considered as nondegenerate. The minimal energy concept provides the basis for the proof. In which two external potential, $V_{ext}(r)\ and\ V'_{ext}(r)$, with differing by a constant are taken, that lead to the same ground state density $n_0(r)$. Even though, those two different external potentials have same ground sate density $n_0(r)$ but would give two different Hamiltonians, $\hat{H}$ and $\hat{H}'$ and would have different ground state wavefunctions, Ψ and Ψ', with $\hat{H}\,\Psi = E_0\Psi$ and $\hat{H}'\psi' = E'_0\,\psi'$. Since $\psi'$is not the ground state of $\hat{H}$, this follows that

$$\begin{aligned} E_0 &< \langle\psi'|\hat{H}|\psi'\rangle \\ &< \langle\psi'|\hat{H}'|\psi'\rangle + \langle\psi'|\hat{H} - \hat{H}'|\psi'\rangle \\ &< E'_0 + \int n_0(r)[V_{ext}(r) - V'_{ext}(r)dr \end{aligned} \qquad \ldots\ldots 3.18$$

Similarly,

$$\begin{aligned} E'_0 &< \langle\psi'|\hat{H}|\psi'\rangle \\ &< \langle\psi'|\hat{H}'|\psi'\rangle + \langle\psi'|\hat{H}' - \hat{H}|\psi'\rangle \\ &< E_0 + \int n_0(r)[V'_{ext}(r) - V_{ext}(r) \end{aligned} \qquad \ldots\ldots 3.19$$

Adding Eq. 18 and 19 lead to the contradiction

$$E'_0 + E_0 < E_0 + E'_0 \qquad \ldots\ldots\ldots 3.20$$

That's why, it can be said that no different external potentials $V_{ext}(r)$can give the same ground state density $n_0(r)$ or in other word, the ground state density determines the external potential $V_{ext}(r)$, except for a constant. So that it can be said that there is a one-to-one between ground state density $n_0(r)$ and external potentials $V_{ext}(r)$ even though the exact formula is unknown.

3.2.3.2 The HK theorem II:

For any $v_{ext}(r)$ we can define a functional for the energy in terms of particle density E[n(r)]. The density that minimizes this functional is the correct ground state density $n_0(r)$[86].

Proof of the HK theorem II:

The universal functional can be written as

$$F[n(r)] \equiv T[n(r)] + E_{int}[n(r)] \quad \ldots\ldots\ldots 3.21$$

Where, the first term, T[n(r)], represents the kinetic energy and the second term, $E_{int}[n(r)]$, represents the interaction energy of the particles. For any wavefunction ψ', The energy function can be expressed as:

$$E[\psi'] \equiv \langle \psi' | \check{T} + \tilde{V}_{int} + \hat{V}_{ext} | \psi' \rangle \quad \ldots\ldots\ldots 3.22$$

This has has its global minimum value only when Ψ' is the ground state wavefunction Ψ_0,

with the constraint that the total number of the particles is conserved. According to HK theorem I, Ψ' must correspond to a ground state with particle density n ′ (r) and external potential V'_{ext} (r), then E[Ψ'] is a functional of n ′ (r). According to variational principle:

$$= E[n'(r)]$$

$$= \int n'(r) V'_{ext}(r) dr + F[n'(r)]$$

$$> E[\Psi_0]$$

$$= n_0(r) V_{ext}(r) dr + F[n_0(r)]$$

$$= E[n_0(r)]$$

Thus, the energy functional

$$E[n(r)] \equiv \int n(r)\, V_{ext}(r) dr + F[n(r)] \quad \ldots\ldots\ldots 3.25$$

Evaluated for the correct ground state density $n_0(r)$, for which the energy functional has lower value than any other density n(r). Hence the ground state density and so the ground state energy can be determined by minimizing the system energy functional with respect to density variation in the density n(r).

The universal functional F[n(r)] is undetermined, thus even if HK theorems employ particle density n(r) as the fundamental variable, it remains impossible to generate any system property.

Kohn and Sham [89] overcame this challenge in 1965 by proposing the well-known Kohn-Sham theorem.

3.2.4 The Kohn-Sham (KS) Ansatz

Kohn and Sham's method [89] entails reformulating the multi-body Hamiltonian into an independent particle system that yields the same ground state density. The electrons are essentially presumed to be uncorrelated aside from what is necessary to meet the exclusion principle. The consequences of many-body correlation are thus approximated by an effective potential that is only dependent on particle density; nonetheless, the Hamiltonian does not explicitly incorporate an interaction term. Instead of particle wavefunctions, the densities are now the focus of our issue.

It can be demonstrated that the interacting many-body system's ground state density may be produced from a more basic system of independent particles, which is the key insight in this case. All multibody interactions are beyond consideration for the effective potential in which electrons move. That makes SEs for a set of independent particles that can be solved exactly

$$\left(-\frac{\hbar^2}{2m}\nabla^2 + v_{eff}\right)\phi_i = \epsilon_i\phi_i \quad \ldots\ldots\ldots 3.26$$

Where the independent particle orbitals are represented by φ_i. If a system has N number of electrons, in the ground state, all the orbitals will have lowest energy. The density of the system can be found from summation over each orbital.

$$n(r) = \sum_i^N |\phi_i(r)|^2$$

$\ldots\ldots\ldots 3.27$

The many-body HK energy functional can be reconstructed for independent-particle form as like below

$$E_{KS}[n] = T_s[n] + \int d^3\, r v_{ext}(r)n(r) + E_H[n] + E_{XC}[n] \quad \ldots\ldots\ldots 3.28$$

where Ts[n], the independent particle kinetic energy, can be expressed as like below:

$$T_s[n] = \sum_{i=1}^{N} \left\langle \phi_i \right| - \frac{\hbar}{2m} \nabla^2 \left| \phi_i \right\rangle$$

… … … 3.29

And the multibody electron-electron interaction energy E_{int} can be broken into a classical coulomb self-interaction term, or Hartree energy $E_H[n]$:

$$E_H[n] = \frac{1}{2} \int d^3r d^3 r' \frac{n(r)n(r')}{|r-r'|} \quad \ldots \ldots \ldots 3.30$$

all the many-body quantum mechanical effects of exchange and correlation are included in E_{XC} that can be redefine as like below by solving the energy functionals in Eq. 3.28:

$$E_{XC}[n] = (T_e[n] - T_s[n]) + (E_{int}[n] - E_H[n]) \quad \ldots \ldots \ldots 3.31$$

This is the residue e kinetic and potential energy in approximating the fully interacting many-body system as a system of independent-particles. This energy (and its associated potential) are the only unknowns in the KS approach.

CHAPTER 4: COMPUTATIONAL DETAILS

The Vienna Ab Initio Simulation Package (VASP) code [94] is used to perform the First principles Density Functional Theory (DFT) calculations. VASP implemented projector augmented wave (PAW) method [95] was taken to consider the interaction between the valence electrons and core ions that was generated by G. Kresse [96] [97]and was first suggested and used by Peter Blöchl [95]. The considered valence electron configurations were $4s^2 4p^6 5s^1$ for Rb, $2p^6 3s^1$ for Na, $3p^6 4s^1$ for K, $5s^2 5p^1$ for In, and $ns^2 np^5$ for Halogen (X). The generalized gradient approximation (GGA) [98] with the Revised PBE for solids (PBEsol) functional [99] was taken to determine the electronic exchange and correlation energy. For all calculations in this study, the cutoff energy for the plane-wave basis set was 520 eV and an automatically generated gamma-centered k-points grid was used that was generated by the Monkhorst–Pack scheme [100] [101]. This k-points sampling in reciprocal space was done by taking 0.02 $\boldsymbol{\pi}$/Å between the 2 nearest points. For Geometry optimization, the structure was relaxed until the energy changes and forces on each atom were less than 10^{-8} eV and 0.001 eV respectively.

For a VASP calculation, 4 input files are required- INCAR, POSCAR, POTCAR and KPOINTS.

4.1 INCAR

The INCAR file serves as the primary input for VASP and controls what should be done and how. The parameters and algorithms chosen by VASP for the computation are set by the INCAR tags supplied in the INCAR file. VASP utilizes sensible default settings, thus it is advised to use them if you are unsure. However, the INCAR file settings are the primary cause of problems and incorrect results, thus it is advised that we thoroughly examine the significance of the specified INCAR tags. Each statement in the format has the following components: the name of a tag, the equal sign =, and the values that have been given to the tag (tag = values).

4.1.1The INCAR file for the ionic relaxation calculation

Global Parameters

ISTART = 0 (Read existing wavefunction; if there)

ISPIN = 1 (Non-Spin polarised DFT)

ICHARG = 2 (Non-self-consistent: GGA/LDA band structures)

LREAL = .FALSE. (Projection operators: automatic)

ENCUT = 520 (Cut-off energy for plane wave basis set, in eV)

PREC = Normal (Precision level)

LWAVE = .TRUE. (Write WAVECAR or not)

LCHARG = .TRUE. (Write CHGCAR or not)

ADDGRID= .TRUE. (Increase grid; helps GGA convergence)

LVTOT = .TRUE. (Write total electrostatic potential into LOCPOT or not)

LVHAR = .TRUE. (Write ionic + Hartree electrostatic potential into LOCPOT or not)

NELECT = (No. of electrons: charged cells; be careful)

LPLANE = .TRUE. (Real space distribution; supercells)

NPAR = 4 (Max is no. nodes; don't set for hybrids)

NWRITE = 2 (Medium-level output)

KPAR = 2 (Divides k-grid into separate groups)

NGX = 500 (FFT grid mesh density for nice charge/potential plots)

NGY = 500 (FFT grid mesh density for nice charge/potential plots)

NGZ = 500 (FFT grid mesh density for nice charge/potential plots)

Electronic Relaxation

ISMEAR = 0 (Gaussian smearing; metals:1)

SIGMA = 0.05 (Smearing value in eV; metals:0.2)

NELM = 60 (Max electronic SCF steps)

NELMIN = 6 (Min electronic SCF steps)

EDIFF = 1E-08 (SCF energy convergence; in eV)

GGA = PS (PBEsol exchange-correlation)

Ionic Relaxation

NSW = 100 (Max ionic steps)

IBRION = 2 (Algorithm: 0-MD; 1-Quasi-New; 2-CG)

ISIF = 3 (Stress/relaxation: 2-Ions, 3-Shape/Ions/V, 4-Shape/Ions)

EDIFFG = -1E-03 (Ionic convergence; eV/AA)

ISYM = 2 (Symmetry: 0=none; 2=GGA; 3=hybrids)

Command Paralleling the work

NCORE = 4

KPAR = 8

4.1.2 The INCAR file for the SCF run

Global Parameters

ISTART = 1 (Read existing wavefunction, if there)

ISPIN = 1 (Non-Spin polarised DFT)

ICHARG = 11 (Non-self-consistent: GGA/LDA band structures)

LREAL = .FALSE. (Projection operators: automatic)

ENCUT = 600 (Cut-off energy for plane wave basis set, in eV)

PREC = Accurate (Precision level: Normal or Accurate, set Accurate when perform structure lattice relaxation calculation)

LWAVE = .TRUE. (Write WAVECAR or not)

LCHARG = .TRUE. (Write CHGCAR or not)

ADDGRID= .TRUE. (Increase grid, helps GGA convergence)

LVTOT = .TRUE. (Write total electrostatic potential into LOCPOT or not)

LVHAR = .TRUE. (Write ionic + Hartree electrostatic potential into LOCPOT or not)

NELECT = (No. of electrons: charged cells, be careful)

LPLANE = .TRUE. (Real space distribution, supercells)

NWRITE = 2 (Medium-level output)

KPAR = 2 (Divides k-grid into separate groups)

NGXF = 300 (FFT grid mesh density for nice charge/potential plots)

NGYF = 300 (FFT grid mesh density for nice charge/potential plots)

NGZF = 300 (FFT grid mesh density for nice charge/potential plots)

Static Calculation

ISMEAR = 0 (gaussian smearing method)

SIGMA = 0.03 (please check the width of the smearing)

LORBIT = 11 (PAW radii for projected DOS)

NEDOS = 2001 (DOSCAR points)

NELM = 60 (Max electronic SCF steps)

EDIFF = 1E-08 (SCF energy convergence, in eV)

Dielectric Constant Calculation

LOPTICS = T

CSHIFT = 0.1

NCORE = 4

4.2 POSCAR

A necessary VASP input file is the POSCAR file. It is a simple text file that at least includes the ionic positions and the lattice structure. It is also possible to specify initial velocities for a molecular-dynamics simulation here.

4.2.1 POSCAR for $Rb_2NaInCl_6$

Primitive Cell

1.00000000000000

-0.0000000000000000 5.3108151047336145 5.3108151047336145

5.3108151047336145 -0.0000000000000000 5.3108151047336145

5.3108151047336145 5.3108151047336145 0.0000000000000000

Rb Na In Cl

2 1 1 6

Direct

0.7500000000000000 0.7500000000000000 0.7500000000000000

0.2500000000000000 0.2500000000000000 0.2500000000000000

-0.0000000000000000 0.0000000000000000 0.0000000000000000

0.5000000000000000 0.5000000000000000 0.5000000000000000

0.7394615699607804 0.2605384300392196 0.2605384300392196

0.2605384300392196 0.2605384300392196 0.7394615699607804

0.2605384300392196 0.7394615699607804 0.7394615699607804

0.2605384300392196 0.7394615699607804 0.2605384300392196

0.7394615699607804 0.2605384300392196 0.7394615699607804

0.7394615699607804 0.7394615699607804 0.2605384300392196

4.2.2 POSCAR for $Rb_2NaInBr_6$

Primitive Cell

1.000000

0.00000000000000 5.62798492556762 5.62798492556762

5.62798492556762 0.00000000000000 5.62798492556762

5.62798492556762 5.62798492556762 0.00000000000000

Rb Na In Br

2 1 1 6

Direct

0.7500000000000000	0.7500000000000000	0.7500000000000000	Rb1
0.2500000000000000	0.2500000000000000	0.2500000000000000	Rb2
0.0000000000000000	0.0000000000000000	0.0000000000000000	Na1
0.5000000000000000	0.5000000000000000	0.5000000000000000	In1
0.7404391662789891	0.2595608337210109	0.2595608337210109	Br1
0.2595608337210109	0.2595608337210109	0.7404391662789891	Br2
0.2595608337210109	0.7404391662789891	0.7404391662789891	Br3
0.2595608337210109	0.7404391662789891	0.2595608337210109	Br4
0.7404391662789891	0.2595608337210109	0.7404391662789891	Br5
0.7404391662789891	0.7404391662789891	0.2595608337210109	Br6

4.2.3 POSCAR for Rb_2NaInI_6

Primitive Cell

1.00000000000000

0.0000000000000000	6.0978791430040200	6.0978791430040200
6.0978791430040200	0.0000000000000000	6.0978791430040200
6.0978791430040200	6.0978791430040200	0.0000000000000000

Rb	**Na**	**In**	**I**
2	1	1	6

Direct

0.7500000000000000	0.7500000000000000	0.7500000000000000
0.2500000000000000	0.2500000000000000	0.2500000000000000
0.5000000000000000	0.5000000000000000	0.5000000000000000
0.0000000000000000	0.0000000000000000	0.0000000000000000
0.7586729222907778	0.2413270777092222	0.2413270777092222
0.2413270777092222	0.2413270777092222	0.7586729222907778
0.2413270777092222	0.7586729222907778	0.7586729222907778

0.2413270777092222 0.7586729222907778 0.2413270777092222

0.7586729222907778 0.2413270777092222 0.7586729222907778

0.7586729222907778 0.7586729222907778 0.2413270777092222

4.3 KPINTS

The Bloch vectors (k points) used to sample the Brillouin zone are described in the KPOINTS file. One of the crucial computations in many electronic minimization calculations is the convergence of this sampling. The most typical method to choose k points is to use a regular mesh.

4.3.1 KPOINTS for Optimization, DOS and different properties calculation

Auto-generated KPOINTS by using Monkhorst-Pack Scheme with a spacing 0.015

K-Spacing Value to Generate K-Mesh: 0.015

0

Monkhorst-Pack

9 9 9

0.0 0.0 0.0

4.3.1 KPOINTS for Band structure calculation

k points along high symmetry lines with 50 number of points per line

K-Path Generated by VASPKIT.

50

Line-Mode

Reciprocal

0.0000000000 0.0000000000 0.0000000000 Gamma

0.5000000000 0.0000000000 0.5000000000 X

0.5000000000 0.0000000000 0.5000000000 X

0.6250000000 0.2500000000 0.6250000000 U

0.3750000000 0.3750000000 0.7500000000 K
0.0000000000 0.0000000000 0.0000000000 Gamma

0.0000000000 0.0000000000 0.0000000000 Gamma
0.5000000000 0.5000000000 0.5000000000 L

0.5000000000 0.5000000000 0.5000000000 L
0.5000000000 0.2500000000 0.7500000000 W

0.5000000000 0.2500000000 0.7500000000 W
0.5000000000 0.0000000000 0.5000000000 X

4.4 POTCAR

The pseudopotential for each atomic species utilized in the computation is essentially included in the POTCAR file. Additionally, the POTCAR file includes details on the atoms, such as their mass POMASS, the number of valence electrons ZVAL, the energy of the reference configuration for which the pseudopotential was generated, etc. It is no longer essential to mention ENCUT in the INCAR file as the POTCAR files also include default energy cutoffs (ENMAX and ENMIN).

CHAPTER 5: RESULT AND DISCUSSIONS

In this chapter, I will discuss about all the outcomes of this theoretical study. It starts from the structural insight of Rb_2MInX_6. Structural, thermodynamic and mechanical stability is reported before the properties identification. After that, it represents the powder diffraction pattern and bond properties. This also contains the mechanical, electronic, dielectric and optical properties of proposed perovskites and some applications of those.

5.1 STRUCTURE of Rb_2MInX_6

It is found that Rb_2NaInX_6 belongs to cubic double perovskite groups, which have an $Fm\bar{3}m$ space group. In which two different octahedra, MX_6 formed by Na^+/K^+ with six surrounding halogen (X) ions and InX_6 formed by In^{3+} with six surrounding halogen (X) ions, alternate in space to form a corner connecting three-dimensional (3D) networks as seen in Fig. 5-1. Similar to Na^+ and Cl^- in rock salt, one MX_6 octahedron is surrounded by six InX_6 octahedra and vice versa. The cesium cation has four adjacent octahedra. Those two types of octahedra are formed by two different hetero-charged cations (Na^+/K^+ and In^{3+}) at the center that have different electronegativity. The bond lengths of Na-X and In-X are different, so they form octahedrons of two different sizes. This reduces the symmetry of the system of double halide perovskite to that of single perovskite, in which only one type of octahedron forms the corner connecting 3D networks.

GGA-PBEsol methods is used to find the lattice parameter. This process can approximate the lattice parameter nearly to its experimental values [102]. Fig. 5-2. shows the change in total energy with respect to the lattice parameter. The lattice parameter of a unit cell corresponds to the lowest energy of the system on which it is most stable. The lattice parameter, as well as other structural information, is listed in Table 5-1. It is clear that as the compound's halide component switches from Cl to Br and then to I, the lattice parameter increases. The lengths of the In-X and M-X bonds (listed in Table 1) also increase in a similar way. This is due to the fact that as we move from Cl to Br to I, the ionic radius of halogen increases.

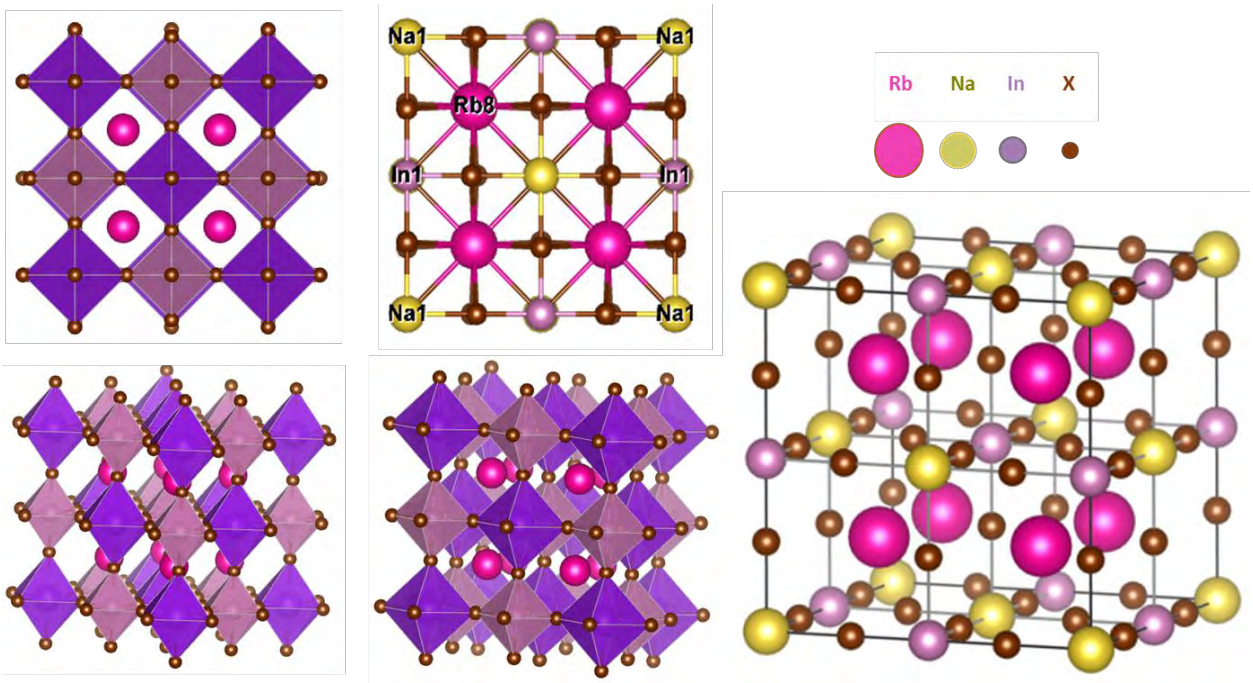

Figure 5-1: Structural configuration of the proposed perovskite group

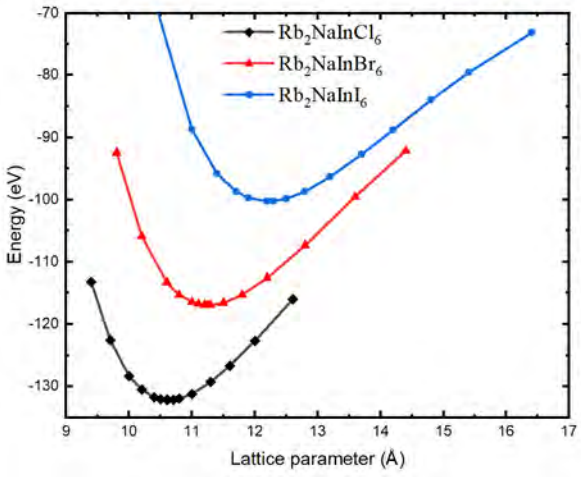

Figure 5-2 Energy vs. lattice parameter from DFT simulations.

Table 5-1. Structural properties of the proposed perovskite unit cells

Compound	Lattice parameter (Å)	Volume (Å^3)	In-X (Å)	Na/K-X (Å)	Rb-X (Å)	Edge length in Na polyhedron	Edge length in In polyhedron
$Rb_2NaInCl_6$	10.614	1195	2.543	2.767	3.757	3.914	3.597
$Rb_2NaInBr_6$	11.256	1426	2.706	2.921	3.981	4.131	3.827
Rb_2NaInI_6	12.914	2153	2.943	3.154	4.313	4.461	4.162
$Rb_2KInCl6$	11.053	1350	2.540	2.986	3.914	4.223	3.593
Rb_2KInBr_6	11.681	1593	2.703	3.137	4.136	4.437	3.823
Rb_2KInI_6	12.610	2005	2.938	3.367	4.464	4.762	4.156

5.2 STRUCTURAL STABILITY

Two empirical formulas called the octahedral factor (μ) [103] and Goldschmidt Tolerance factor (t) [104] can be used to predict the stability of the cubic phase of 3D perovskites with high symmetric octahedron without twisting and tilting. Historically, not only for halides but also for oxides and chalcogenides, this formula has been used to predict the cubic structure of perovskite [105].

Generally, for the ideal case, the Goldschmidt Tolerance Factor has the value of unity for a stable cubic phase but, we can expect good stability of the cubic phase of perovskite when the 't' value is between 0.81 and 1.11. Compounds that have values outside those two constraints may not form stable cubic perovskite, and the symmetry of the perovskite will be reduced. A tetragonal or orthorhombic phase transition may take place for a smaller value of t, and that phase may be discovered to be stable at room temperature [106]. A layer structure rather than a three-dimensional structure may be formed by distortion in cubic perovskite for larger values of t [107].

The octahedral factor is used to determine whether the B or B' ion is fitted in the octahedron perfectly. The acceptable 'μ' value is taken between 0.44 and 0.90 [103]. For Double Perovskite with $A_2B(I)B'(III)X_6$ structure,

$$\textit{Octahedral factor, } \mu = (R_{B(I)} + R_{B(III),})/2R_X \quad 5.1$$

$$\textit{Goldschmidt Tolerance Factor, } t = (R_A+R_X)/(\sqrt{2}\{((R_B+R_X)/2) + R_X\}) \quad 5.2$$

where the respective Shannon effective ionic radii [108] of the A, B(I), B'(III), and X ions are represented by R_A, $R_{B(I)}$, $R_{B'(III)}$, and R_X respectively.

The ionic radii of elements depend on the coordination number and ionic state of the materials in the compound. Structural analysis from this first principles calculations it showed that Rb^+ has a coordination number of 12 while Na^+, $In^{3+,}$ and X^- have a coordination number of 6. The Shannon ionic radius for those elements for these specific conditions is given in Table. 5-2. Table 5-3 and figure 5-3 shows that, with the exception of Rb_2LiInX_6 and Rb_2NaInI_6, all of those compounds satisfied the requirements for the octahedral factor and the Goldschmidt tolerance factor in order to maintain the stable cubic phase of the perovskite. Despite the fact that Rb_2NaInI_6 does not meet the octahedral factor requirement, this value is still close to the stable limit for this empirical formula for the stability of cubic perovskites. For that reason, this wasn't completely ruled out of consideration. But Lithium based perovskites, Rb_2LiInX_6, are further from the stability limit in consideration of octahedral factor, that's why those are completely ruled out for the further analysis.

Table 5-2. Structural properties of the proposed perovskite unit cells

Element	Ionic state	Co-ordination Number	Ionic radius
Rb	+1	12	172pm
Li	+1	6	76pm

Na	+1	6	102pm
K	+1	6	138pm
Cl	-1	6	181pm
Br	-1	6	196pm
I	-1	6	220pm
In	+3	6	80pm

Table 5-3. Calculated Octahedral Factor and Goldschmidt tolerance factor of the proposed perovskites

Perovskite	Octahedral Factor	Tolerance factor
$Rb_2LiInCl_6$	0.39	0.96
$Rb_2LiInBr_6$	0.37	0.94
Rb_2LiInI_6	0.35	0.93
$Rb_2NaInCl_6$	0.50	0.92
$Rb_2NaInBr_6$	0.46	0.91
Rb_2NaInI_6	0.41	0.89
Rb_2KInCl_6	0.60	0.86
Rb_2KInBr_6	0.56	0.85
Rb_2KInI_6	0.50	0.84

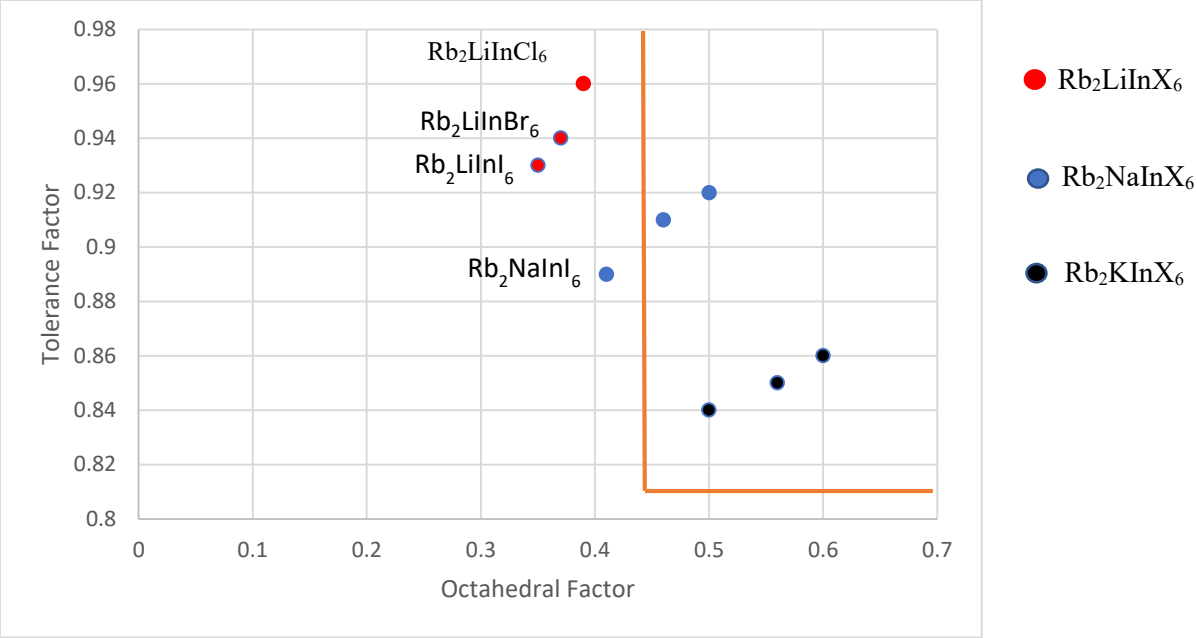

Figure 5-3. Octahedral factor and tolerance factor

5.3 MECHANICAL STABILITY AND MECHANICAL PROPERTIES

Mechanical properties and mechanical stability of the perovskites had been determined by the strain-energy method, in which a small strain was applied on the lattice to deform the structure, and the energy of the distorted phase is calculated, from which second-order non-generative elastic constants are predicted that follows the Born stability criterion [109]. Hooke's law determines the elastic responses of the material in the elastic region with an applied strain, and the Voigt notation [110] shown below is a straightforward way to express these responses.

$$\sigma_i = \sum_{j=1}^{6} C_{ij}\varepsilon_j$$

Where, both the stress and strain are represented by a matrix with six components and C_{ij} is the second order elastic stiffness tensor expressed by a 6 x 6 matrix. The elastic stiffness tensor matrix only has 3 identical components for the cubic phase.

Stiffness Tensor matrix C_{ij} for materials of cubic unit cell:

C11	C12	C12	0	0	0
C12	C11	C12	0	0	0
C12	C12	C11	0	0	0
0	0	0	C44	0	0
0	0	0	0	C44	0
0	0	0	0	0	C44

The cubic structure of the perovskites is stable only when the deformed structure has more energy than the cubic phase. To form a mechanically stable cubic phase, the following 5 constraints must be met: $C_{11} - C_{12} > 0$, $C_{11} > 0$, $C_{44} > 0$, $C_{11} + 2C_{12} > 0$, and $C_{12} < B < C_{11}$ [111] [112]. These are summarized in table 5-16 and figure 5-29. It has been found that those conditions are met by all the Na-based perovskites, but K-based perovskites fail to meet the C44 >0 criterion and as a result, Na- based perovskites are mechanically stable but K-based perovskites are not. That's why K-based perovskites will not be considered for the properties analysis. The mechanical properties of the considered materials like Bulk Modulus B (GPa), Young's Modulus E (GPa), Shear Modulus G (GPa), Poisson's Ratio v, etc. are calculated by using Voigt, Reuss, and Hill approximations by using the stiffness tensor [110]. The average bulk modulus (B) and shear modulus (G) can be taken as the arithmetic means of the Voigt and Reuss modulus [113], and the Poisson's ratio v and young's modulus (E) can be expressed as given below:

$$E = \frac{9BG}{3B+G}$$

$$\nu = \frac{3B-E}{6B}$$

Table 5-4 elastic tensor matrix (in GPa) of $Rb_2NaInCl_6$

36.7277	10.0663	10.0663	0.0000	0.0000	0.0000
10.0663	36.7277	10.0663	0.0000	0.0000	0.0000
10.0663	10.0663	36.7277	0.0000	0.0000	0.0000
0.0000	0.0000	0.0000	7.8090	0.0000	0.0000
0.0000	0.0000	0.0000	0.0000	7.8090	0.0000
0.0000	0.0000	0.0000	0.0000	0.0000	7.8090

Table 5-5. Average Mechanical properties of Rb2NaInCl6 in Voigt, Reuss and Hill method

Averaging scheme	**Bulk modulus (GPa)**	**Young's modulus (GPa)**	**Shear modulus (GPa)**	**Poisson's ratio**	**Vickers Hardness (GPa)**
Voigt	K_V = 18.953	E_V = 25.551	G_V = 10.018	V_V = 0.275	*Hv =2.28*
Reuss	K_R = 18.953	E_R = 24.110	G_R = 9.359	V_R = 0.288	*H_R =2.01*
Hill	K_H = 18.953	E_H = 24.834	G_H = 9.689	V_H = 0.282	*H_H= 2.14*

Table 5-6 Eigenvalues of the stiffness matrix of $Rb_2NaInCl_6$

λ_1	λ_2	λ_3	λ_4	λ_5	λ_6
7.809 GPa	7.809 GPa	7.809 GPa	26.661 GPa	26.661 GPa	56.86 GPa

Table 5-7. Variations of the elastic moduli and anisotropy in different mechanical properties of $Rb_2NaInCl_6$:

	Young's modulus **(GPa)**		Linear compressibility **(TPa^{-1})**		Shear modulus **(GPa)**		Bulk modulus **(GPa)**		Poisson's ratio	
	Min	Max	Min	Max	Min	Max	Min	Max	Min	Max
Value	20.60	32.40	17.59	17.59	7.81	13.33	18.95	18.95	0.15	0.45
Anisotropy	1.57		1.00		1.71		1.00		2.99	

Visual representations of mechanical properties in different directions can be drawn by using ELATE software [112]. The young's modulus, linear compressibility, shear modulus and poison's ratio are drawn in 3D and 2D for XY, YZ and ZX planes. Figures 5-3, 5-13 and 5-20 show the spatial dependence of Young's modulus of Rb2NaInCl6, Rb2NaInBr6 and Rb2NaInI6 respectively on XY, YZ and XZ plane. Figures 5-5, 5-14 and 5-22 show linear compressibility, figures 5-7, 5-16 and 5-24 show shear modulus and figures 5-9, 5-18 and 5-26 show Poisson's ratio of proposed perovskite as the same order as before on XY, YZ and ZX planes. The spatial dependence of Young's modulus is drowned in three dimensions in figure 5-4 for Rb2NaInCl6, figure 5-14 for Rb2NaInBr6 and figure 5-21 for Rb2NaInI6. Spatial dependence of linear compressibility is drowned in three dimensions in figure 5-6 for Rb2NaInCl6, figure 5-15 for Rb2NaInBr6 and figure 5-23 for Rb2NaInI6. The spatial dependence of shear modulus is drowned in three dimensions in figure 5-8 for Rb2NaInCl6, figure 5-17 for Rb2NaInBr6 and figure 5-25 for Rb2NaInI6. The spatial dependence of Poisson's ratio is drowned in three dimensions in figure 5-10 for Rb2NaInCl6, figure 5-19 for Rb2NaInBr6 and figure 5-27 for Rb2NaInI6. From this, it can be visualized how the mechanical properties are changed in space with direction, in other words, directional dependence of mechanical properties can be identified more easily.

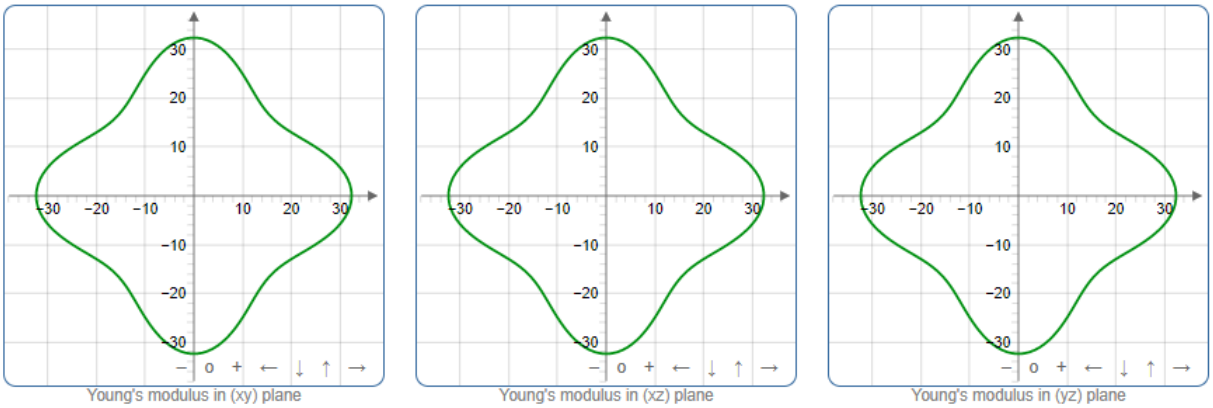

Figure 5-4 Spatial dependence of Young's modulus of $Rb_2NaInCl_6$, at XY, YZ and ZX plane

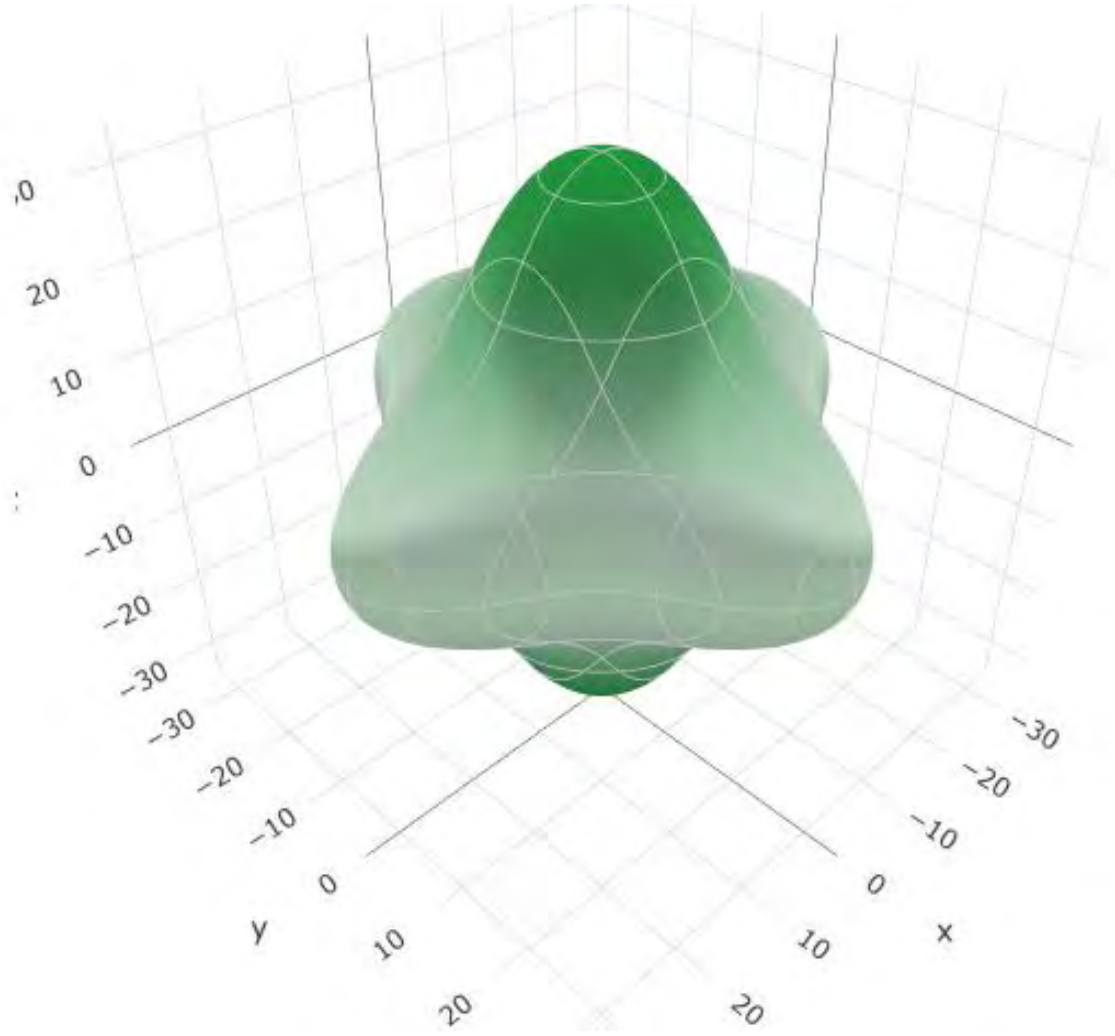

Figure 5-5 Spatial dependence of Young's modulus of $Rb_2NaInCl_6$ in three dimensions

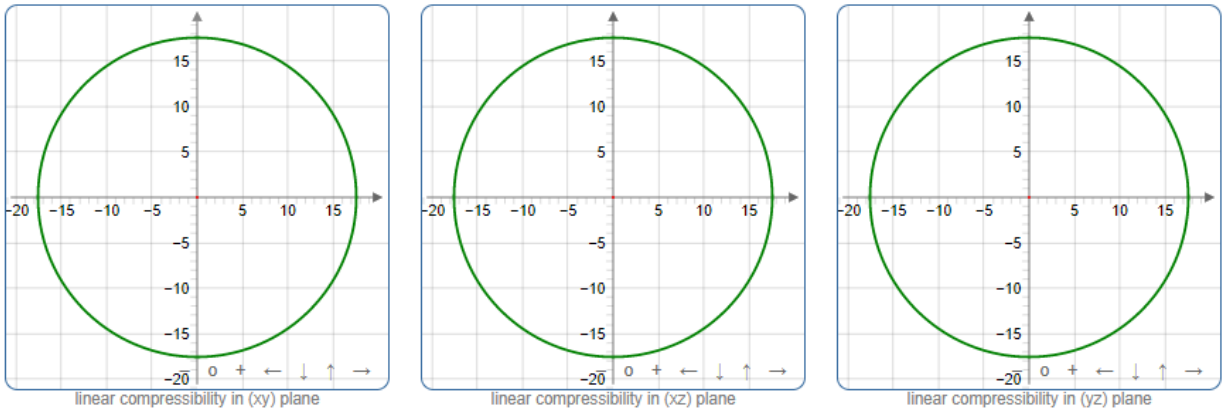

Figure 5-6 Spatial dependence of linear compressibility of $Rb_2NaInCl_6$, at XY, YZ and ZX plane

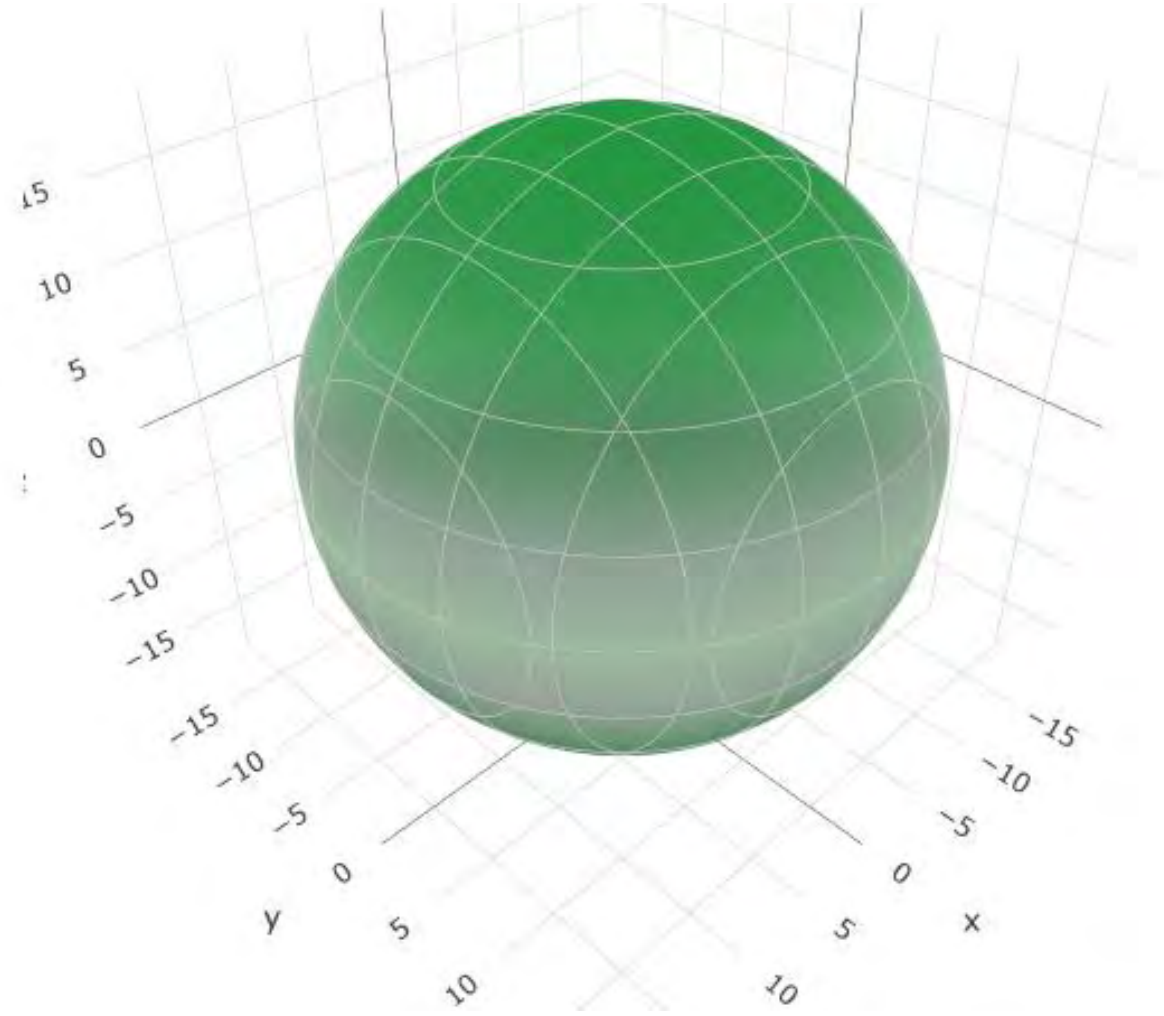

Figure 5-7 Spatial dependence of linear compressibility of $Rb_2NaInCl_6$ in three dimensions

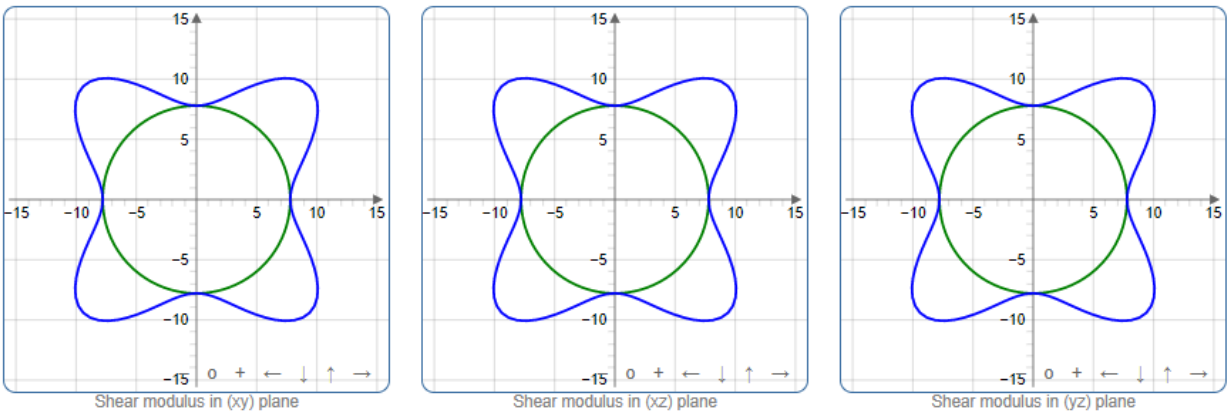

Figure 5-8 Spatial dependence of shear modulus of $Rb_2NaInCl_6$, at XY, YZ and ZX plane

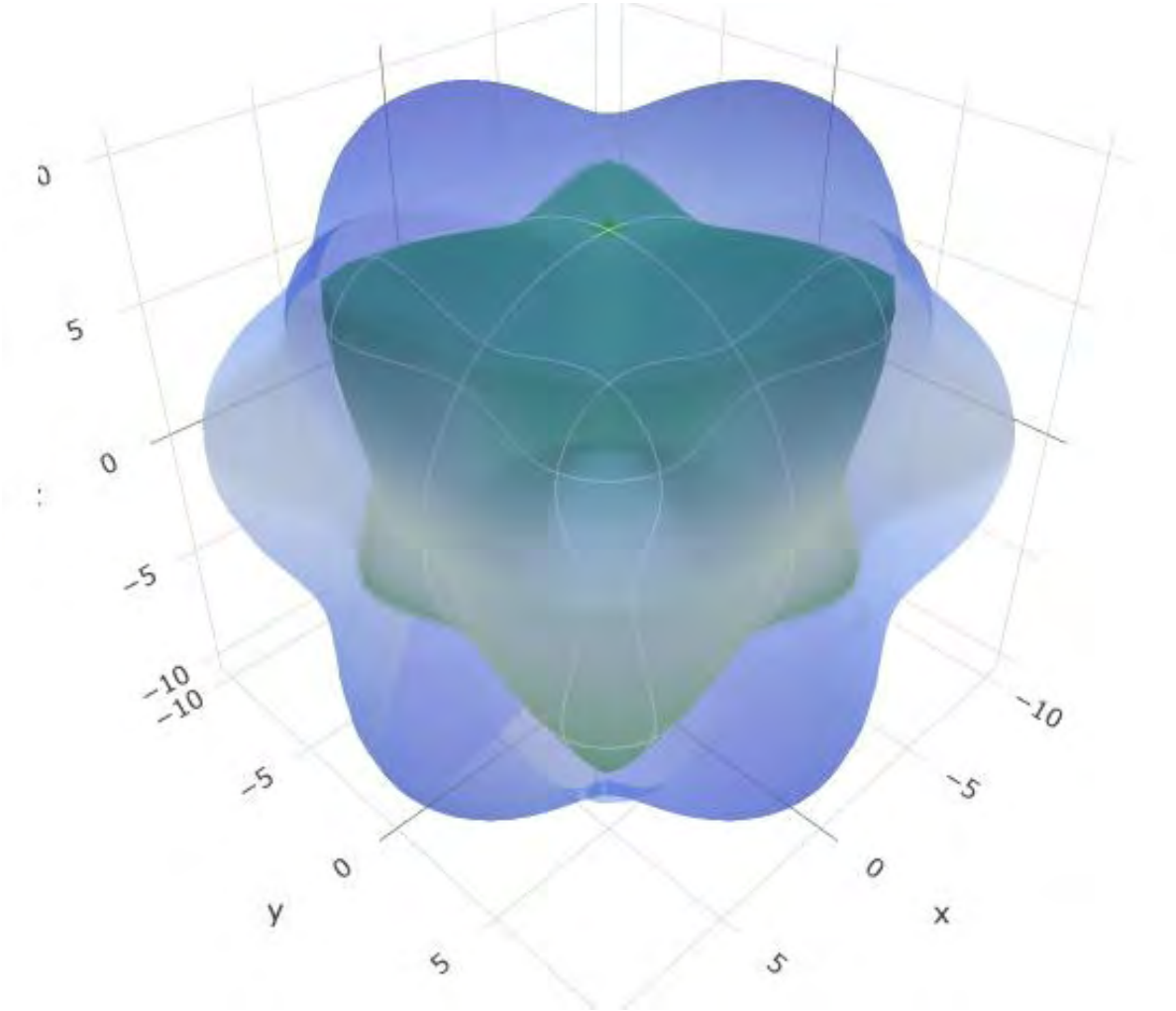

Figure 5-9 Spatial dependence of shear modulus of $Rb_2NaInCl_6$ in three dimensions

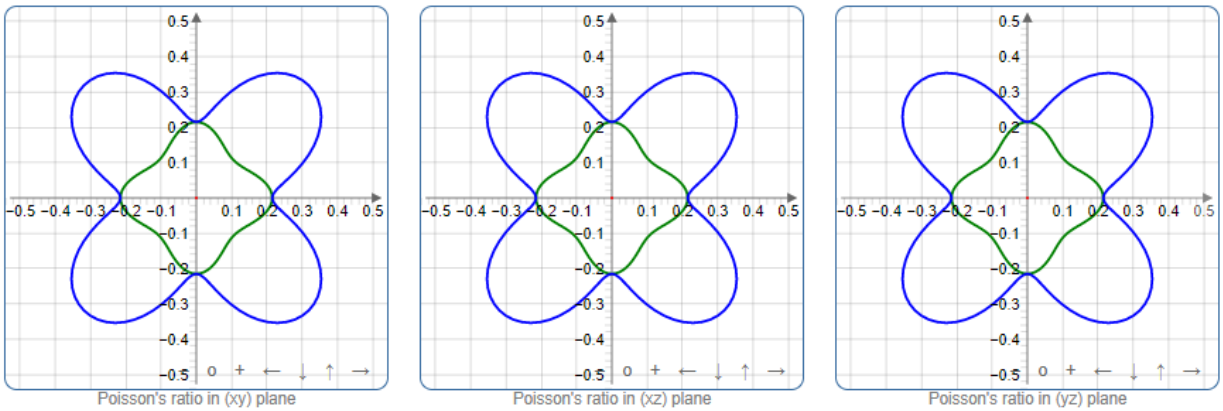

Figure 5-10 Spatial dependence of Poisson's ratio of $Rb_2NaInCl_6$, at XY, YZ and ZX plane

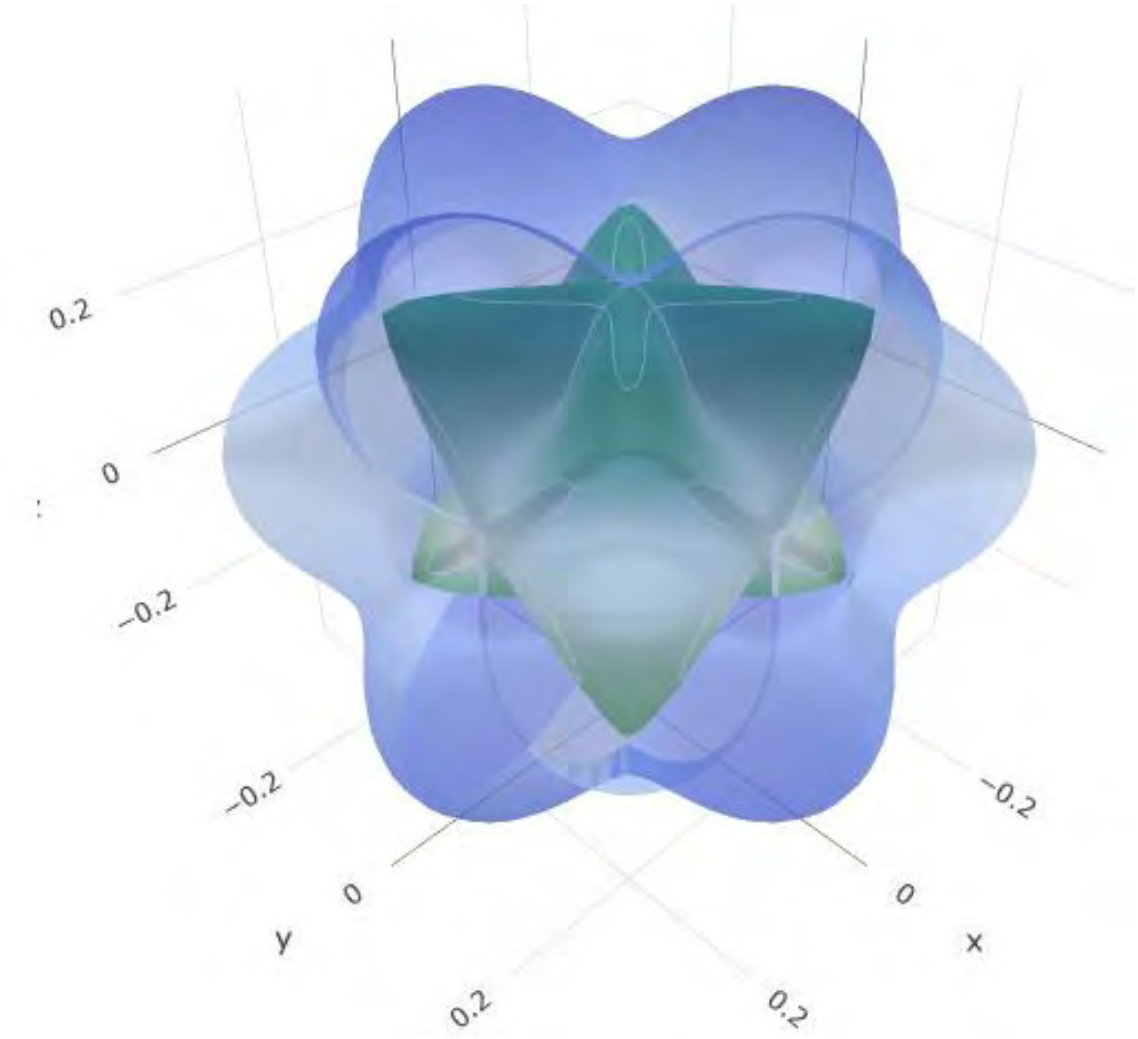

Figure 5-11 Spatial dependence of Poisson's ratio of $Rb_2NaInCl_6$ in three dimensions

From figures 5-3 to 5-11, it is found that the young modulus, shear modulus and Poisson's ratio of $Rb_2NaInCl_6$ show directional properties but linear compressibility is isotropic. For young's modulus, its highest value is along three crystal axial directions such as [0 0 1] direction and the lowest value is through the corners of the cube such as [1 1 1] direction shown in fig. 5-12. For the Poisson's ration and shear modulus, the maximum and minimum are at just reverse direction (min at the axial direction and maximum through the corner).

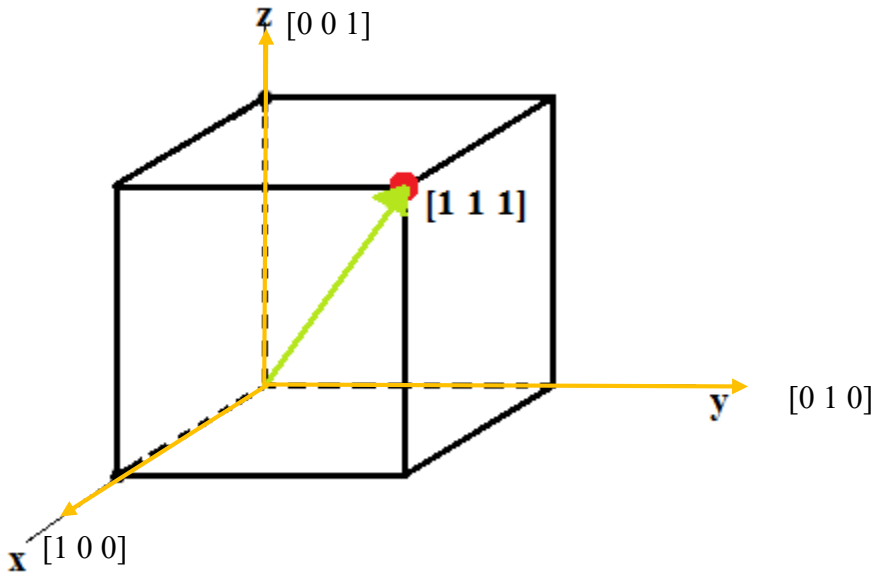

Figure 5-12 different directions in a cubic unit cell

Table 5-8 elastic tensor matrix (in GPa) of $Rb_2NaInBr_6$

30.694	8.228	8.228	0.000	0.000	0.000
8.228	30.694	8.228	0.000	0.000	0.000
8.228	8.228	30.694	0.000	0.000	0.000
0.000	0.000	0.000	5.333	0.000	0.000
0.000	0.000	0.000	0.000	5.333	0.000
0.000	0.000	0.000	0.000	0.000	5.333

Table 5-9 Average Mechanical properties of $Rb_2NaInBr_6$ in Voigt, Reuss and Hill method

Averaging scheme	Bulk modulus (GPa)	Young's modulus (GPa)	Shear modulus (GPa)	Poisson's ratio	Vickers hardness (GPa)
Voigt	K_V = 15.717	E_V = 19.842	G_V = 7.693	ν_V = 0.289	*1.73*
Reuss	K_R = 15.717	E_R = 17.717	G_R = 6.751	ν_R = 0.312	*1.36*
Hill	K_H = 15.717	E_H = 18.789	G_H = 7.222	ν_H = 0.301	*1.54*

Table 5-10 Eigenvalues of the stiffness matrix of $Rb_2NaInBr_6$

λ_1	λ_2	λ_3	λ_4	λ_5	λ_6
5.333 GPa	5.333 GPa	5.333 GPa	22.466 GPa	22.466 GPa	47.15 GPa

Table 5-11 Variations of the elastic moduli and anisotropy in different mechanical properties of $Rb_2NaInBr_6$:

	Young's modulus (GPa)		Linear compressibility (TPa^{-1})		Shear modulus (GPa)		Bulk Modulus (GPa)		Poisson's ratio	
	Min	Max	Min	Max	Min	Max	Min	Max	Min	Max
Value	14.73	27.22	21.21	21.21	5.33	11.23	15.72	15.72	0.13	0.53
Anisotropy	1.89		1.00		2.11		1.00		4.17	

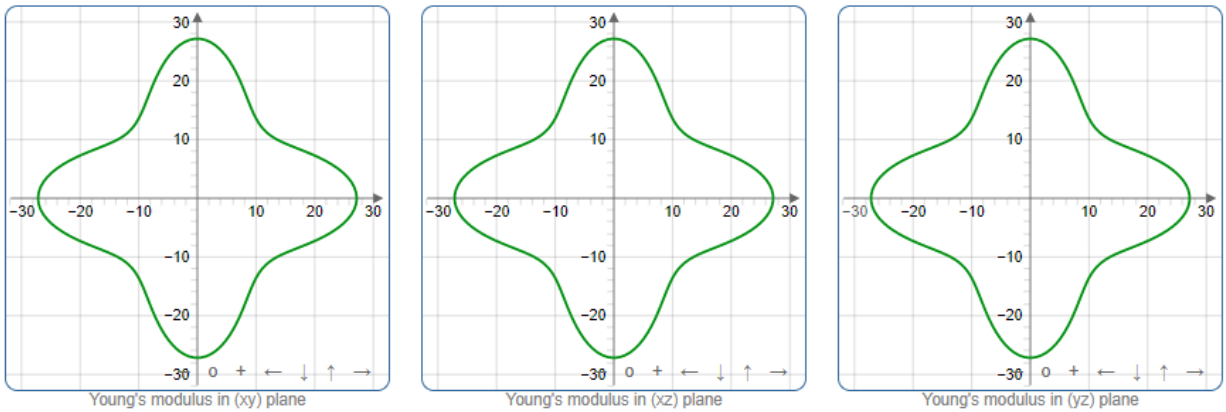

Figure 5-13 Spatial dependence of Young's modulus of $Rb_2NaInBr_6$, at XY, YZ and ZX plane

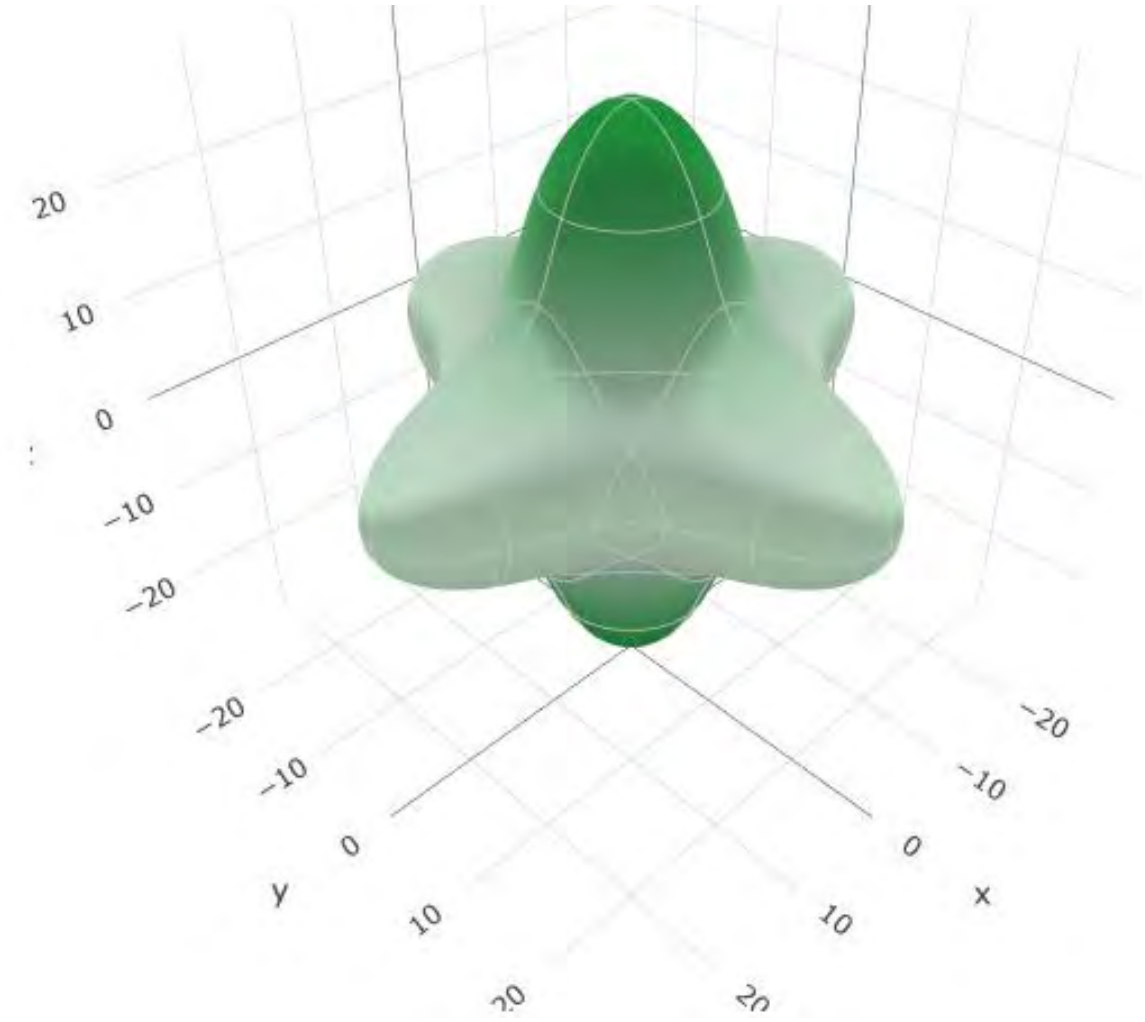

Figure 5-14 Spatial dependence of Young's modulus of $Rb_2NaInBr_6$ in three dimensions

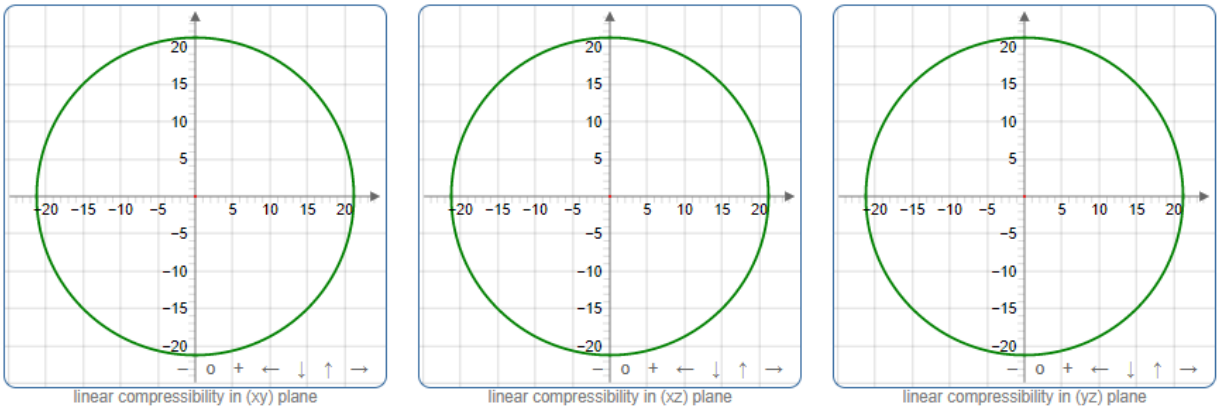

Figure 5-15 Spatial dependence of linear compressibility of $Rb_2NaInBr_6$, at XY, YZ and ZX plane

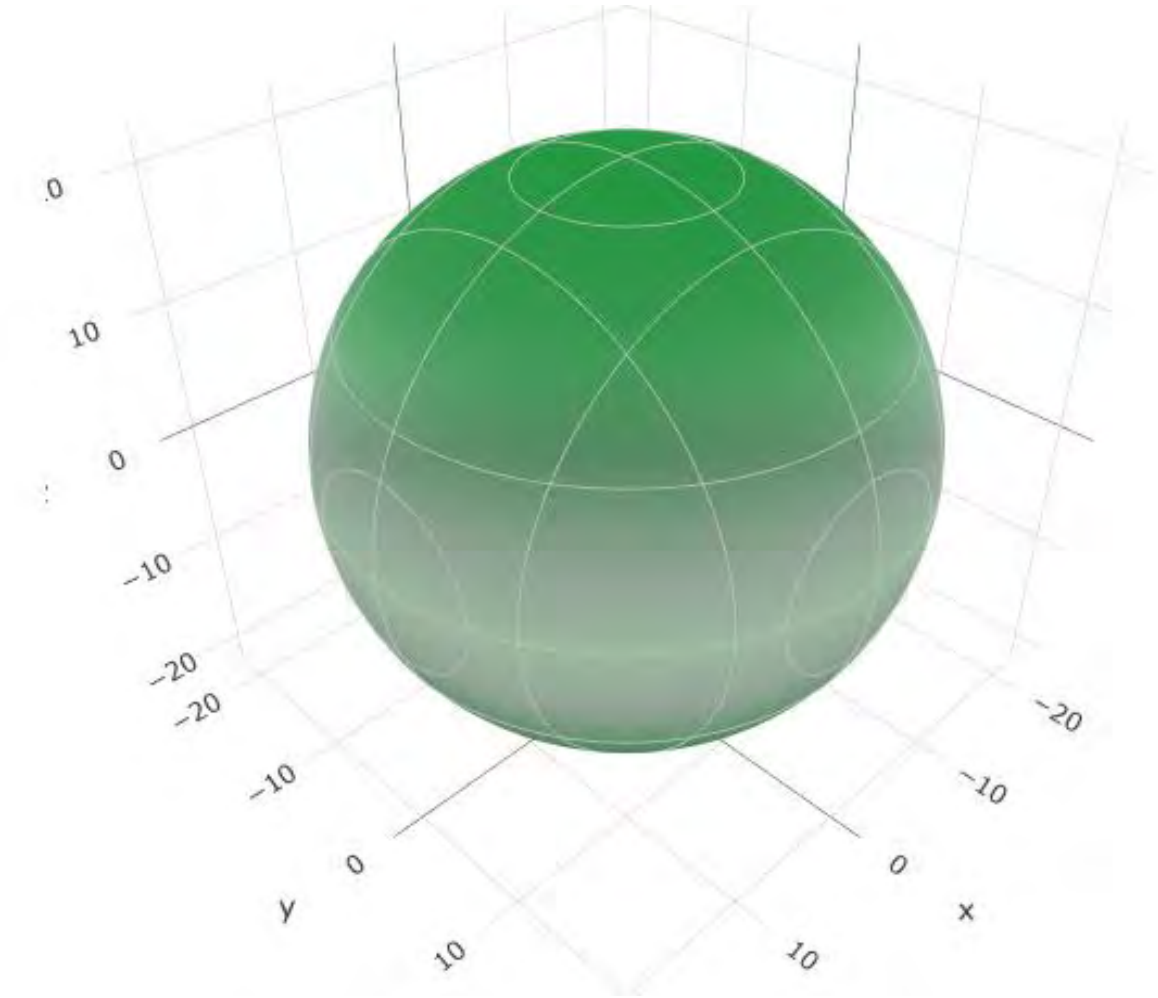

Figure 5-16 Spatial dependence of linear compressibility of $Rb_2NaInBr_6$ in three dimensions

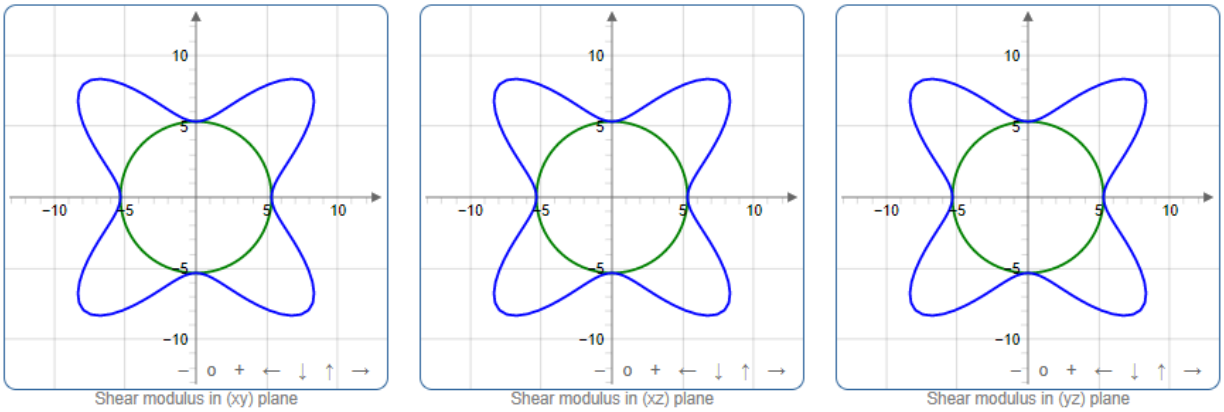

Figure 5-17 Spatial dependence of shear modulus of $Rb_2NaInBr_6$, at XY, YZ and ZX plane

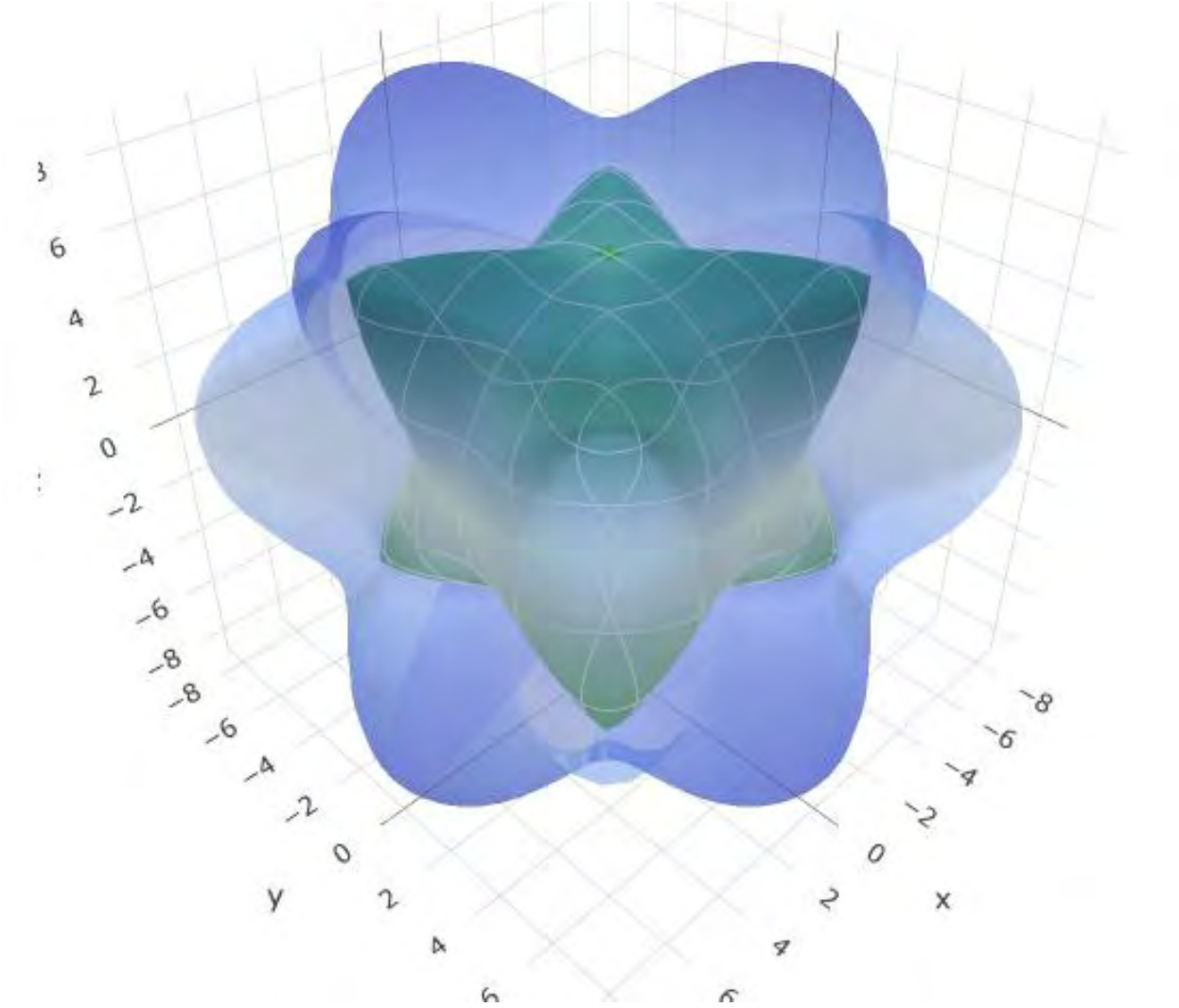

Figure 5-18 Spatial dependence of shear modulus of $Rb_2NaInBr_6$ in three dimensions

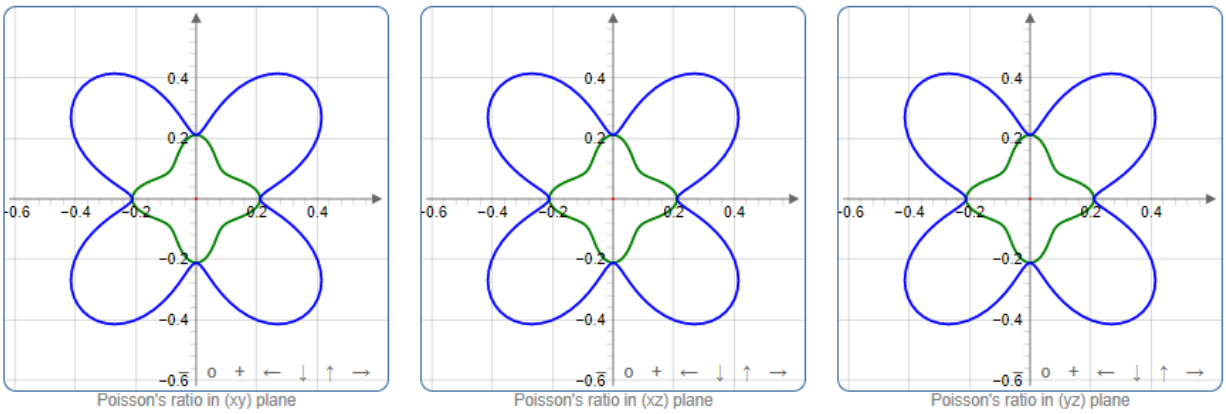

Figure 5-19 Spatial dependence of Poisson's ratio of Rb2NaInBr6, at XY, YZ and ZX plane

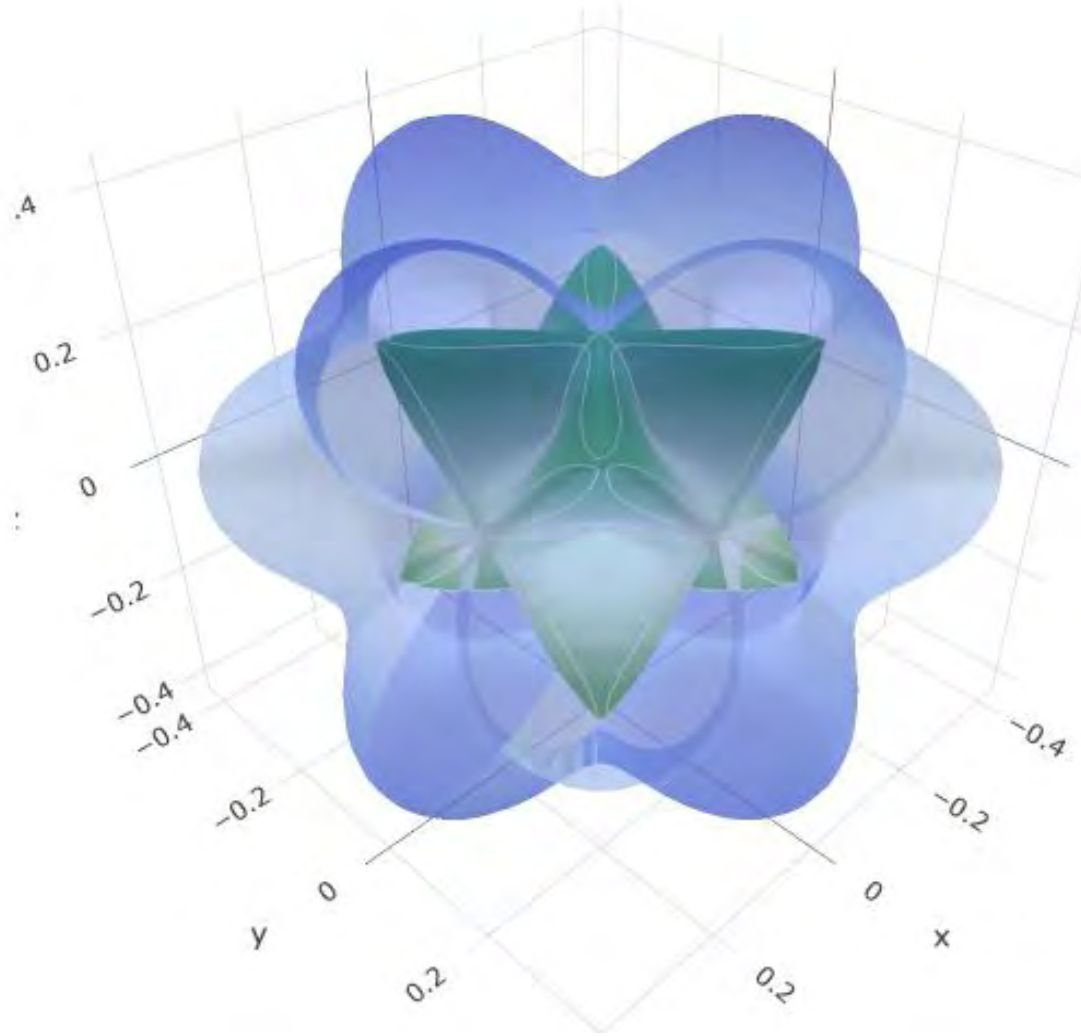

Figure 5-20 Spatial dependence of Poisson's ratio of $Rb_2NaInBr_6$ in three dimensions

From the figures of Spatial dependence of mechanical properties for $Rb_2NaInBr_6$, figures 5-13 to 5-20, it is found that this perovskite also shows the same type of mechanical properties in space. But the directional dependence of the young's modulus, shear modulus and Poisson's ratio are more intensive for Rb_2NaInI_6 than $Rb_2NaInBr_6$ and $Rb_2NaInCl_6$ and this also has lower young's modulus, shear modulus, bulk modulus but higher value of Poisson's ratio.

Table 5-12 elastic tensor matrix (in GPa) of Rb_2NaInI_6

22.844	6.898	6.898	0.000	0.000	0.000
6.898	22.844	6.898	0.000	0.000	0.000
6.898	6.898	22.844	0.000	0.000	0.000
0.000	0.000	0.000	3.087	0.000	0.000
0.000	0.000	0.000	0.000	3.087	0.000
0.000	0.000	0.000	0.000	0.000	3.087

Table 5-13 Average Mechanical properties of Rb_2NaInI_6 in Voigt, Reuss and Hill method

Averaging scheme	Bulk modulus (GPa)	Young's modulus (GPa)	Shear modulus (GPa)	Poisson's ratio	Vickers Hardness (GPa)
Voigt	K_V = 12.213	E_V = 13.295	G_V = 5.041	ν_V = 0.318	*1.06*
Reuss	K_R = 12.213	E_R = 11.036	G_R = 4.089	ν_R = 0.349	*0.72*
Hill	K_H = 12.213	E_H = 12.179	G_H = 4.565	ν_H = 0.334	*0.88*

Table 5-14 Eigenvalues of the stiffness matrix of Rb_2NaInI_6

λ_1	λ_2	λ_3	λ_4	λ_5	λ_6
3.087 GPa	3.087 GPa	3.087 GPa	15.946 GPa	15.946 GPa	36.64 GPa

Table 5-15 Variations of the elastic moduli and anisotropy in different mechanical properties of Rb_2NaInI_6

	Young's modulus (GPa)		Linear compressibility (TPa^{-1})		Shear modulus (GPa)		Bulk Modulus (GPa)		Poisson's ratio	
	Min	Max	Min	Max	Min	Max	Min	Max	Min	Max
Value	8.54	19.64	27.29	27.29	3.08	7.97	12.21	12.21	0.12	0.61
Anisotropy	2.30		1.00		2.58		1.00		5.20	

Table 5-16 Calculated mechanical stability of the proposed perovskites

Perovskite	**C11 (Gpa)**	**C12 (GPa)**	**C44 (GPa)**	**Bulk modulus (B in GPa)**
$Rb_2NaInCl_6$	36.73	10.07	7.81	18.95
$Rb_2NaInBr_6$	30.73	8.21	5.33	15.72
Rb_2NaInI_6	22.88	6.90	3.09	12.21
Rb_2KInCl_6	28.71	6.51	-1.12	16.78
Rb_2KInBr_6	30.10	5.27	-1.77	13.55
Rb_2KInI_6	29.32	4.61	-1.97	9.88

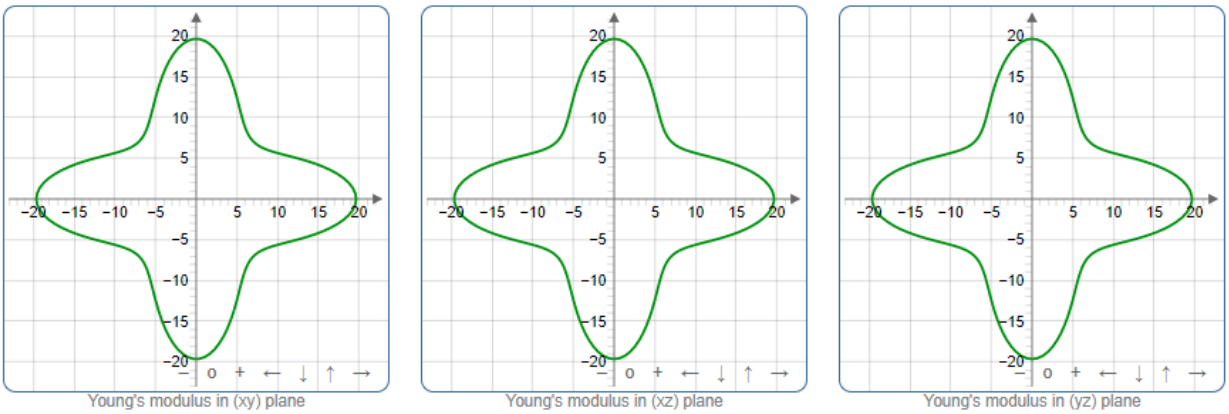

Figure 5-21 Spatial dependence of Young's modulus of Rb_2NaInI_6, at XY, YZ and ZX plane

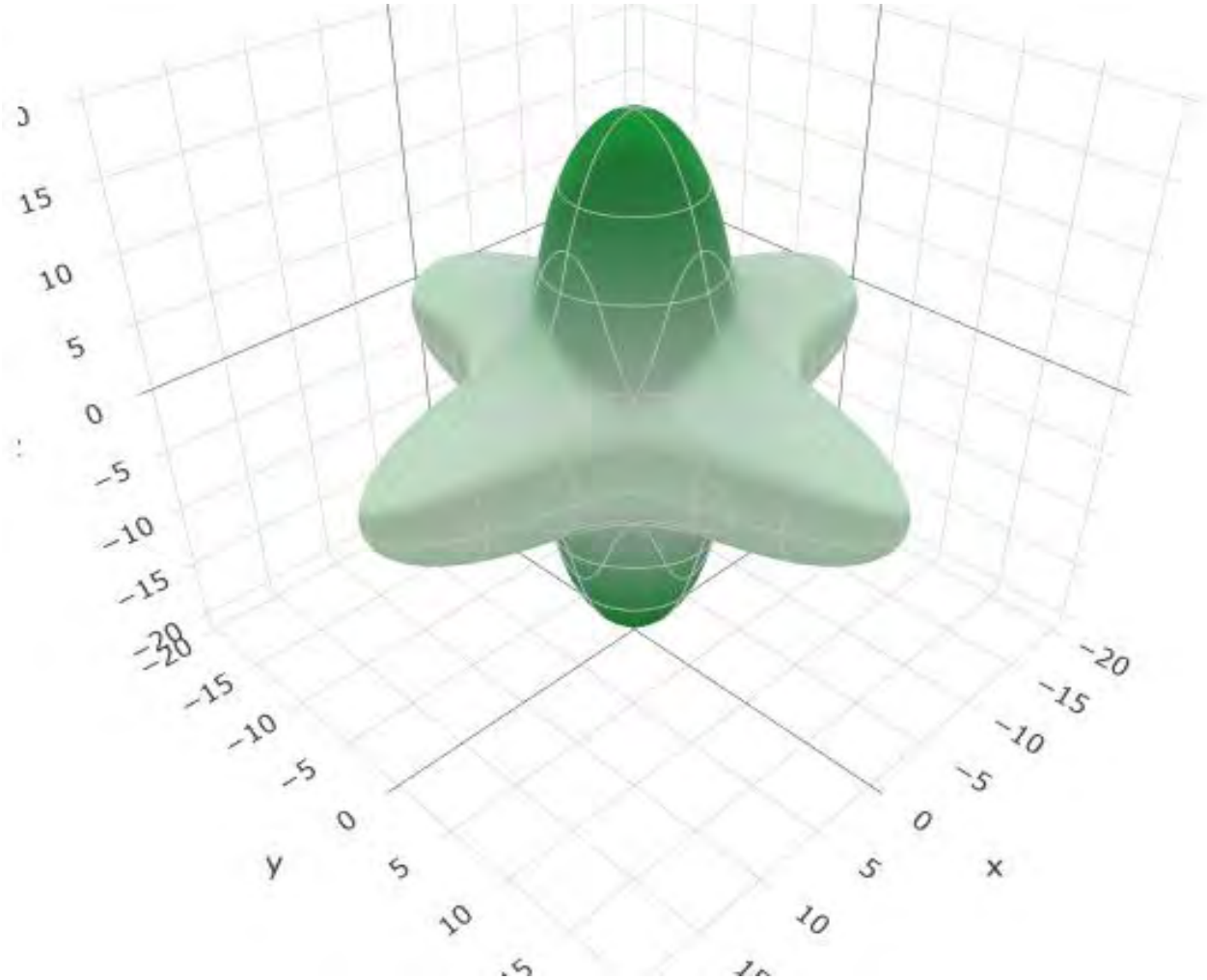

Figure 5-22 Spatial dependence of Young's modulus of Rb_2NaInI_6 in three dimensions

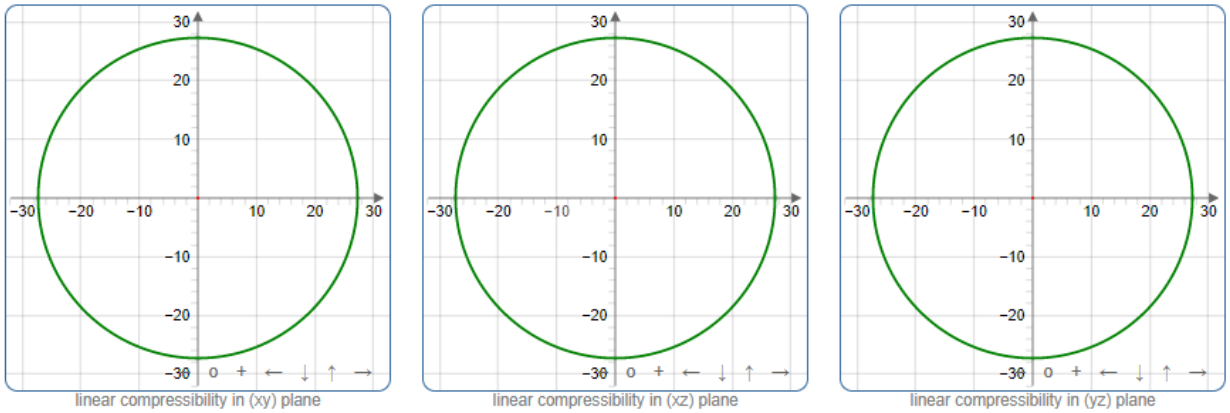

Figure 5-23 Spatial dependence of linear compressibility of Rb_2NaInI_6, at XY, YZ and ZX plane

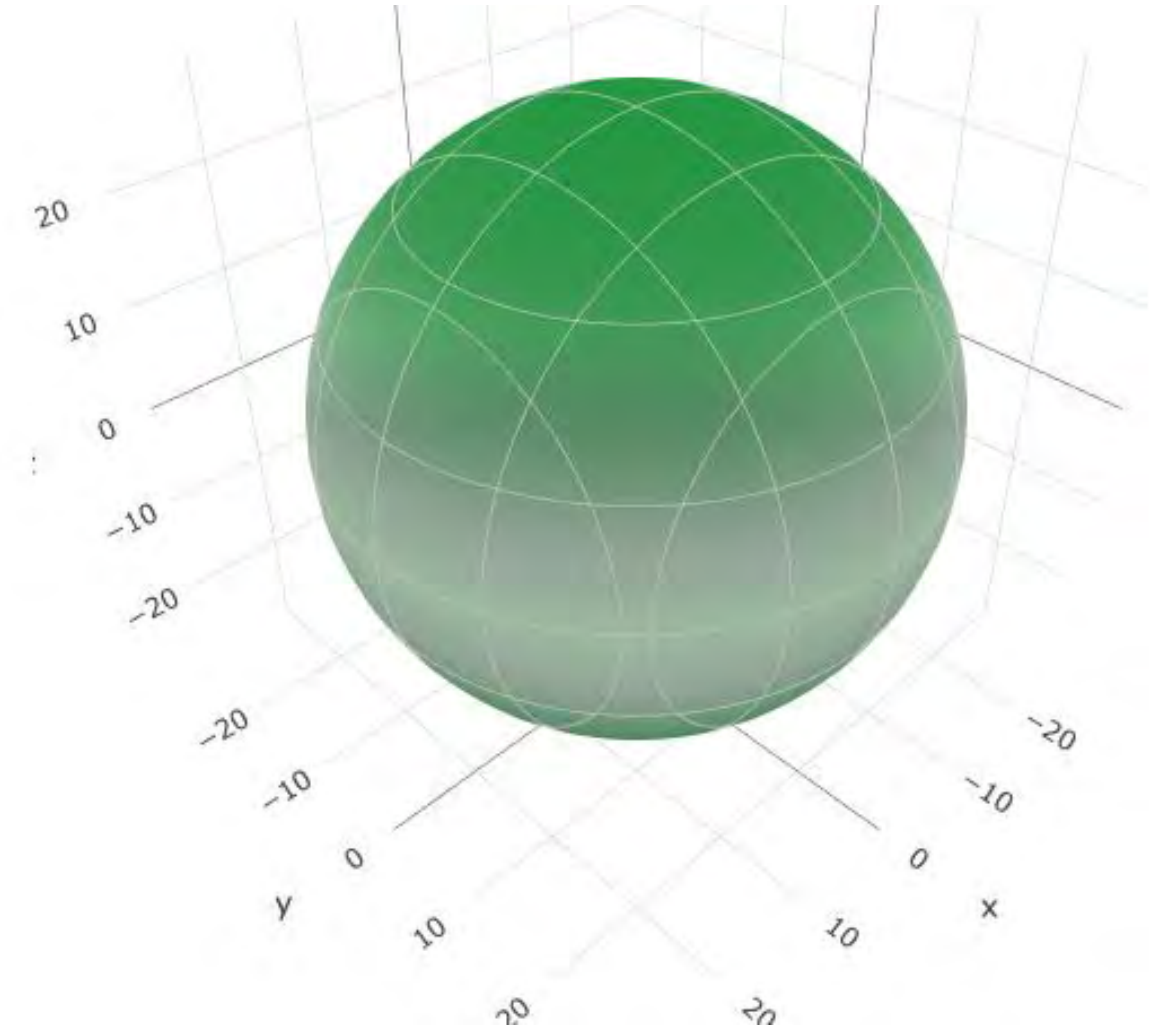

Figure 5-24 Spatial dependence of linear compressibility of Rb_2NaInI_6 in three dimensions

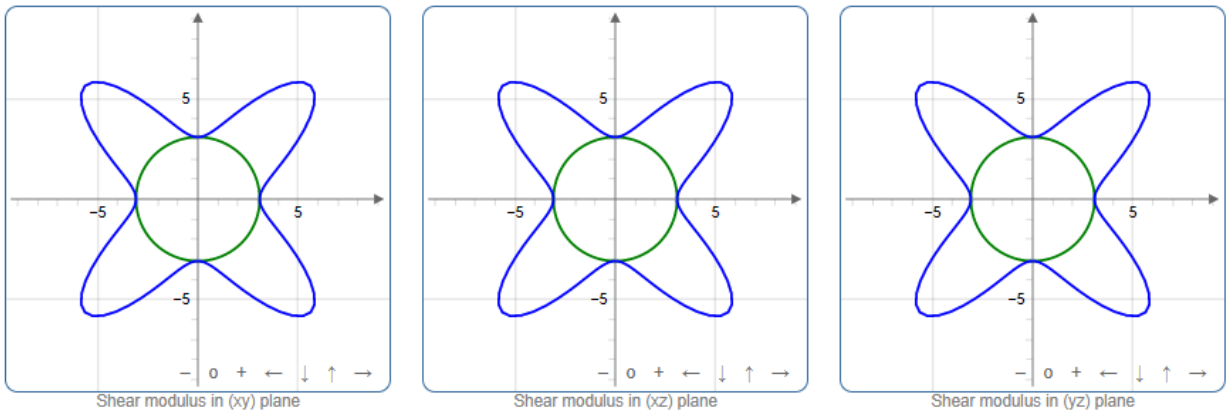

Figure 5-25 Spatial dependence of shear modulus of Rb_2NaInI_6, at XY, YZ and ZX plane

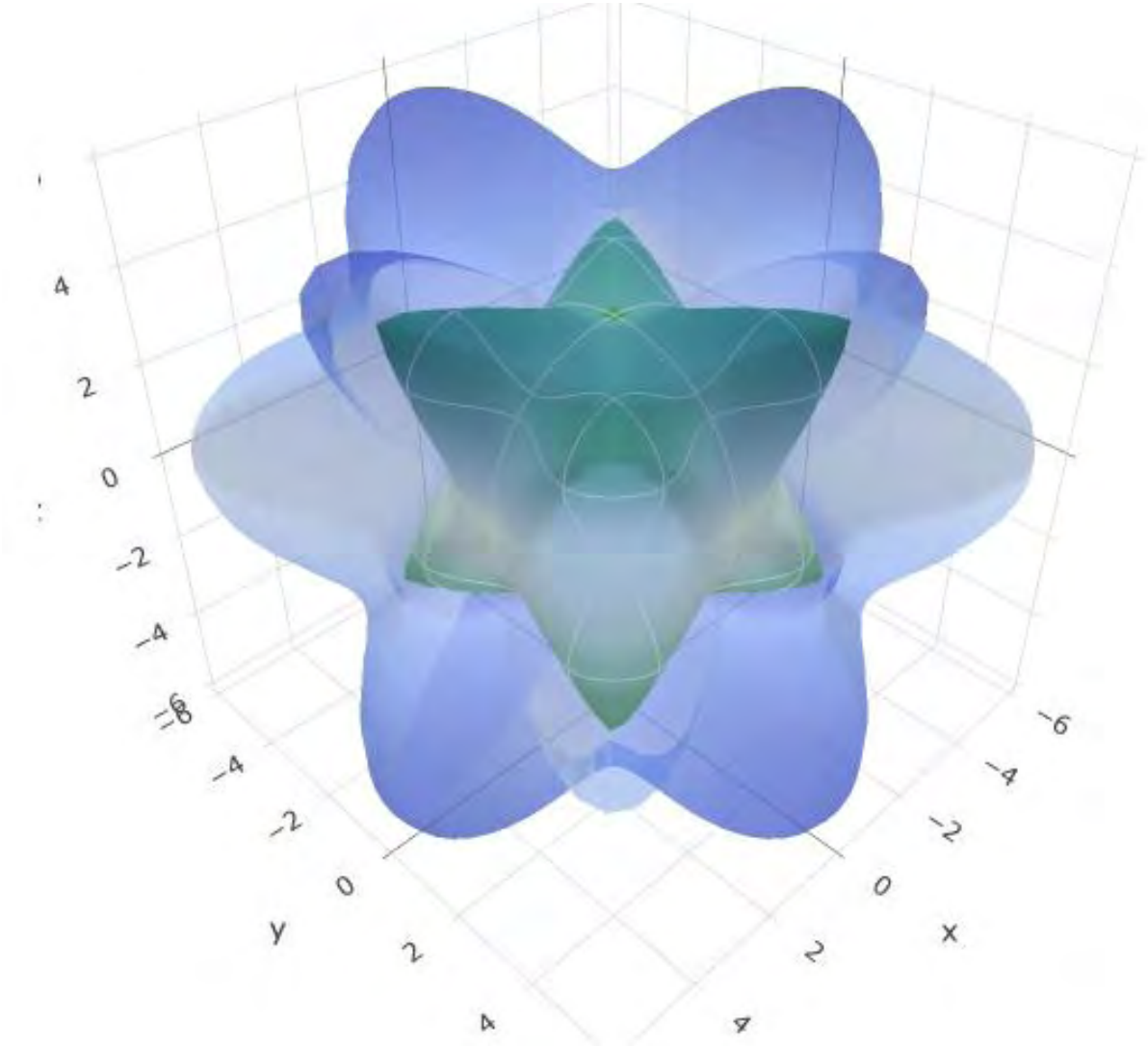

Figure 5-26 Spatial dependence of shear modulus of Rb_2NaInI_6 in three dimensions

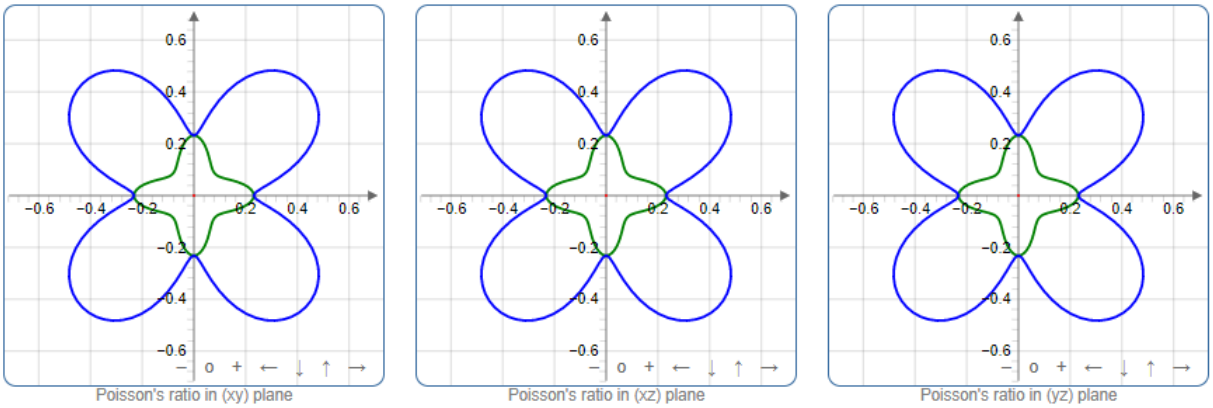

Figure 5-27 Spatial dependence of Poisson's ratio of Rb_2NaInI_6, at XY, YZ and ZX plane

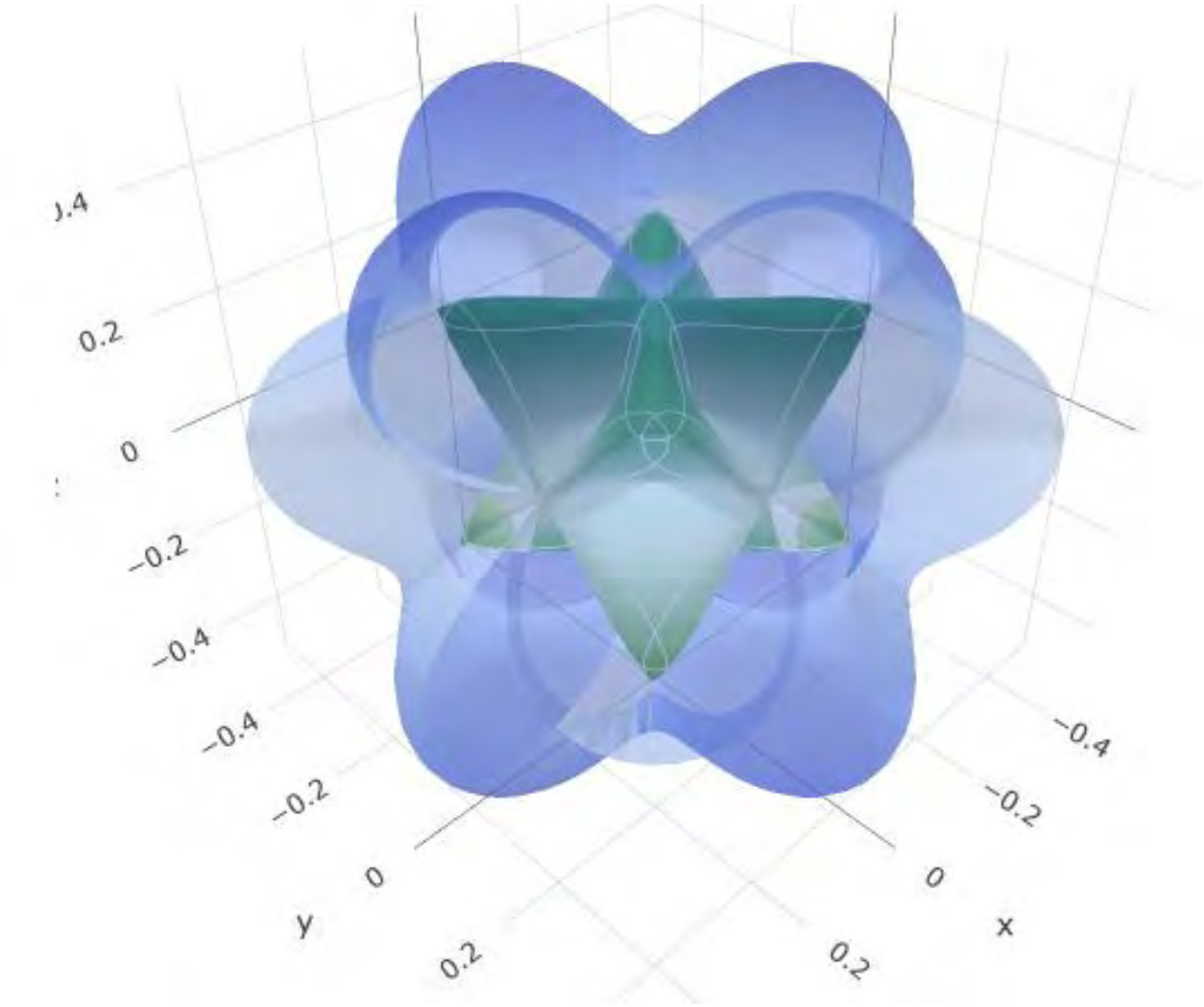

Figure 5-28 Spatial dependence of Poisson's ratio of Rb_2NaInI_6 in three dimensions

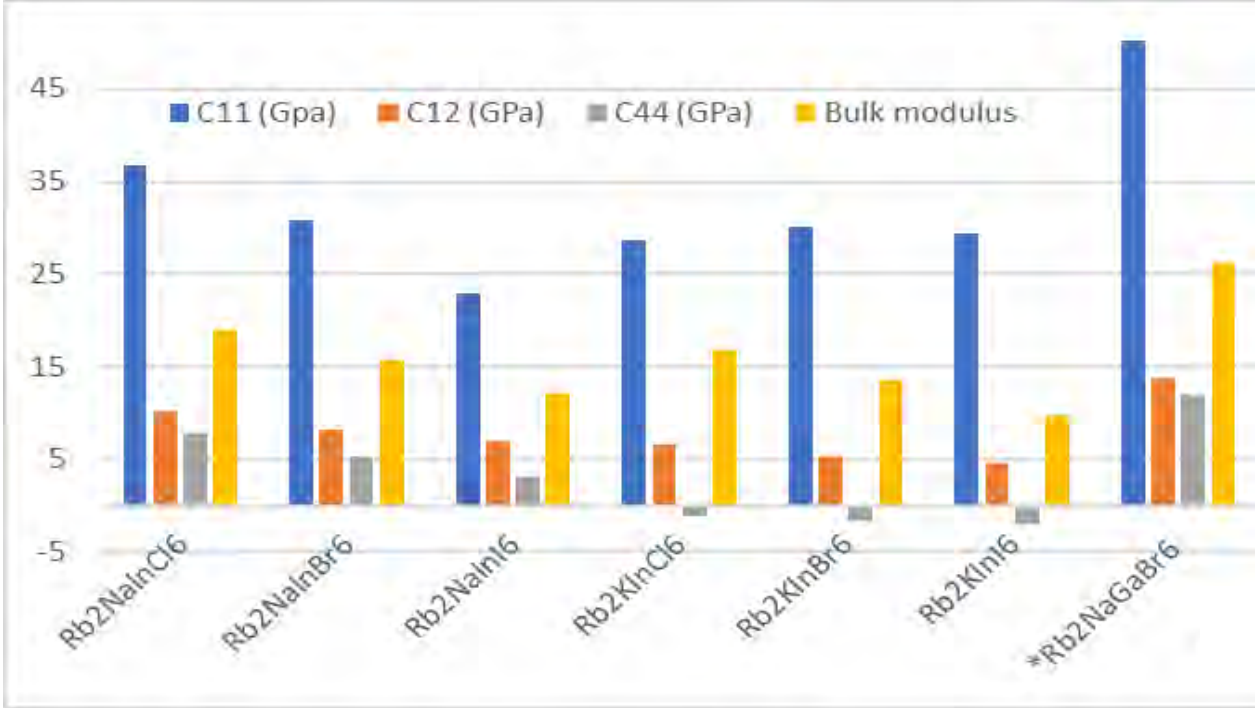

Figure 5-29 C11, C12, C44 and Bulk Modulus of structural and thermodynamically stable perovskites.

All the mechanical properties of those perovskites are summarized in Table 5-17. By analyzing those it is said that the Bulk modulus(B), Young's Modulus (E), and Shear Modulus (G) are decreasing from $Rb_2NaInCl_6$ to $Rb_2NaInBr_6$ to Rb_2NaInI_6. Young's Modulus (E), Shear Modulus (G), and Poisson's ratio (v) are different in different directions that represent the anisotropic behavior of those properties. From table 5-7, it is found that anisotropy in Young's Modulus (E), Shear Modulus (G), and Poisson's ratio (v) are 1.57, 1.71, and 2.99 respectively for $Rb_2NaInCl_6$. From table 5-11, it is found that anisotropy in Young's Modulus (E), Shear Modulus (G), and Poisson's ratio (v) are 1.89, 2.11, and 4.17 respectively for $Rb_2NaInBr_6$. From table 5-15, it is found that anisotropy in Young's Modulus (E), Shear Modulus (G), and Poisson's Ratio (v) are 2.30, 2.58, and 5.20 respectively for Rb_2NaInI_6. However, for all perovskites, bulk modulus (B) and linear compressibility have the same value of anisotropy that is 1. The isotropic behavior is represented by the value 1 and the deviation from this represents anisotropy. So, the calculated perovskites show isotropic bulk modulus and linear compressibility but anisotropy in Young's Modulus (E), Shear Modulus (G), and Poisson's Ratio (v). The Poisson's Ratio exhibits greater anisotropy. For $Rb_2NaInCl_6$, $Rb_2NaInBr_6$, and Rb_2NaInI_6, the corresponding universal elastic anisotropy [114] values are 0.35, 0.70, and 1.1 respectively. A pure anisotropic material has a

universal elastic anisotropy value of 1 and an isotropic material has a value of 0 [114]. So, these perovskites show universal anisotropic elastic properties, and the anisotropy increases from $Rb_2NaInCl_6$ to $Rb_2NaInBr_6$ to Rb_2NaInI_6.

Tables 5-16 and 5-17 show that all perovskites have a C_{11} value that is higher than their C_{12} and C_{44} values, and that the bulk modulus (B) is higher than the shear modulus (G), indicating that the perovskites are more resistant to volume deformation than shape deformation.

The failure mode of the materials and their suitability for use and handling are determined by the materials' ductility. By using the Pugh's Ratio (B/G) [115], Poisson's Ratio (v) [116], and Cauchy pressure [117] ($CP = C_{12} - C_{44}$), it is possible to predict the ductility of the materials. To be ductile, a material must have a Pugh's Ratio of greater than 1.75 [118], a Poisson's Ratio of greater than 0.26 [116], and a Cauchy pressure of greater than zero [117]. All of the perovskites have index values above the limit, making them all ductile. Table 5-17 reflects the progression of ductility from $Rb_2NaInCl_6$ to $Rb_2NaInBr_6$ to Rb_2NaInI_6.

Cauchy Pressure (C_{12}-C_{44}) can be used to determine whether covalent-like bonding (C_{12}-C_{44} <0) or ionic-like bondings (C_{12}-C_{44} >0) are formed [119]. The non-negative values indicate the ionic-like bond formation in the proposed perovskites groups. Kleinman's parameter determines whether or not the bond bending is dominant [120]. A value of less than 0.5 denotes the bonds' dominance in bending. Kleinman's parameter for all perovskites is close to 0.5, indicating intermediate properties.

Longitudinal wave velocity (v_l) and transverse wave velocity (v_t) are calculated for all perovskites by using the following equations [121]:

$$v_l = \sqrt{\frac{3B+4G}{3\rho}} \qquad v_t = \sqrt{\frac{G}{\rho}}$$

The mean value of sound velocity is then calculated as follows:

$$v_m = \left[\frac{1}{3}\left(\frac{2}{v_t^3} + \frac{1}{v_l^3}\right)\right]^{-1/3}$$

Many physical properties of the materials like specific heat, melting temperature, and elastic properties are related to the Debye Temperature (θ_D) [114] which can be calculated using the following equation [123]:

$$\theta_D = \frac{\hbar}{k_B}\left(\frac{3nN_A\rho}{4\pi M}\right)^{1/3} v_m$$

Where ħ is Planck's constant, kB is Boltzmann's constant, N_A is Avogadro's number, ρ is the density, n is the number of atoms in a perovskite molecule, and M is the molecular weight of the perovskite. The sound velocity and Debye temperature represent the authenticity of the anisotropy present in the perovskites, and the high value of Debye temperature indicates the thermal stability of those perovskites at high temperatures.

Table 5-17 Calculated mechanical properties of the proposed perovskites

Parameters	$Rb_2NaInCl_6$	$Rb_2NaInBr_6$	Rb_2NaInI_6
Bulk modulus (B in GPa)	18.95	15.72	12.21
Shear modulus (G in GPa	9.68	7.23	4.56
Young's modulus (Y)	24.83	18.8	12.16
Pugh's ratio (B/G)	1.96	2.17	2.68
Poisson's ratio (σ)	0.28	0.3	0.33
Cauchy pressure	2.3	2.9	3.8
Vickers Hardness (GPa)	2.14	1.55	0.89
Kleinman's parameter	0.49	0.48	0.53
Universal Elastic Anisotropy	0.35	0.7	1.1
Longitudinal wave velocity (m/s)	3320	2628	2161
Transverse wave velocity (m/s)	1830	1403	1079
Mean sound velocity (VD in m/s)	2040	1567	1211
Debye temperature (θD in K)	195.6	141.8	101.1

5.4 THERMODYNAMIC STABILITY

The perovskites must have thermodynamic stability to form stable compounds. Thermodynamic stability is determined by formation energy and decomposition energy. A stable perovskite must have negative formation energy and positive decomposition energy for all the possible decomposition pathways. The formation energy (E_f) of the perovskite can be determined by the following equation:

$$E_f = E_{Rb2M(I)M'(III)X6-} - n_{Rb} \times E_{Rb} - n_{M(I)} \times E_{M(I)} - n_{M'(III)} \times E_{M'(III)} - n_X \times E_X$$

Where, $E_{Rb2M(I)M'(III)X6}$ is the total energy of perovskites, E_{Rb}, $E_{M(I)}$, $E_{M'(III)}$, E_X are the energy of Rb, M(I), M'(III) metals and halogen respectively. The value of 'n' will be the total number of atoms present in the calculated cell.

For this case, formation energy per atom, $E_f = \{E_{Rb2M(I)M'(III)X6} - [\, 2E_{Rb} + E_{M(I)} + E_{M'(III)} + 6 E_X \,]\} /10$

All of those perovskites' formation energies are discovered to be negative which indicates formability of these perovskites. The greater the formation energy's negative value, the more stable the perovskite is. From this, it was seen that Perovskites with Cl have more negative formation energy and thus higher stability compared to Br or I. By comparing the formation energies of the perovskites, it is discovered that they are more stable than MAPbI3 (0.51 eV/atom), since the calculated perovskites have more negative formation energies.

To further confirm the stability, we also calculated the decomposition energies of those perovskites through a potential pathway as follows:

$Rb_2M(I)M'(III)X_6 \longrightarrow 2\ RbX + M(I)X + M'(III)X_3$

The decomposition energy for this case can be determined by the equations given below:

Pathway-1:

$E_{D1} = [\, 2E_{RbX} + E_{M(I)X} + E_{M'(III)X3} \,] - E_{Rb2M(I)M'(III)X6}$

Where, $E_{\mathrm{Cs/Rb2M(I)M'(III)X6}}$ is the total energy of perovskites, E_{RbX}, $E_{M(I)X}$, $E_{M'(III)X3}$, $E_{Rb3M'2(III)X9}$ are the energy of RbX, M(I)X M'(III)X_3 and Rb_3M'(III)X_9 respectively.

The calculated formation and decomposition energies for all those compounds is given in Table 5-18 and figure 5-30. All of the perovskites have demonstrated positive decomposition energy, which makes them resistant to decomposition in this pathway and thermodynamically stable. Chlorine-based perovskites have a higher positive energy of decomposition than bromine and iodine-based perovskites, indicating a higher stability for Rb_2KInCl_6 and a lower stability for Rb_2NaInI_6 and the thermodynamic stability decreases from Cl-based to Br-based to I-based perovskites. Additionally, this is consistent with the formation energy calculated earlier.

Table 5-18 Calculated formation and decomposition energies of the proposed perovskites

Perovskite	Formation Energy (eV)	Per Atom (eV)	Decomposition Energy (eV)	Decomposition Energy Per Atom (eV)
$Rb_2NaInCl_6$	-16.0	-1.60	6.75	0.675
$Rb_2NaInBr_6$	-13.4	-1.34	5.32	0.532
Rb_2NaInI_6	-9.98	-0.998	3.98	0.398
Rb_2KInCl_6	-16.1	-1.61	6.52	0.652
Rb_2KInBr_6	-13.6	-1.36	5.10	0.510
Rb_2KInI_6	-10.2	-1.02	3.76	0.376

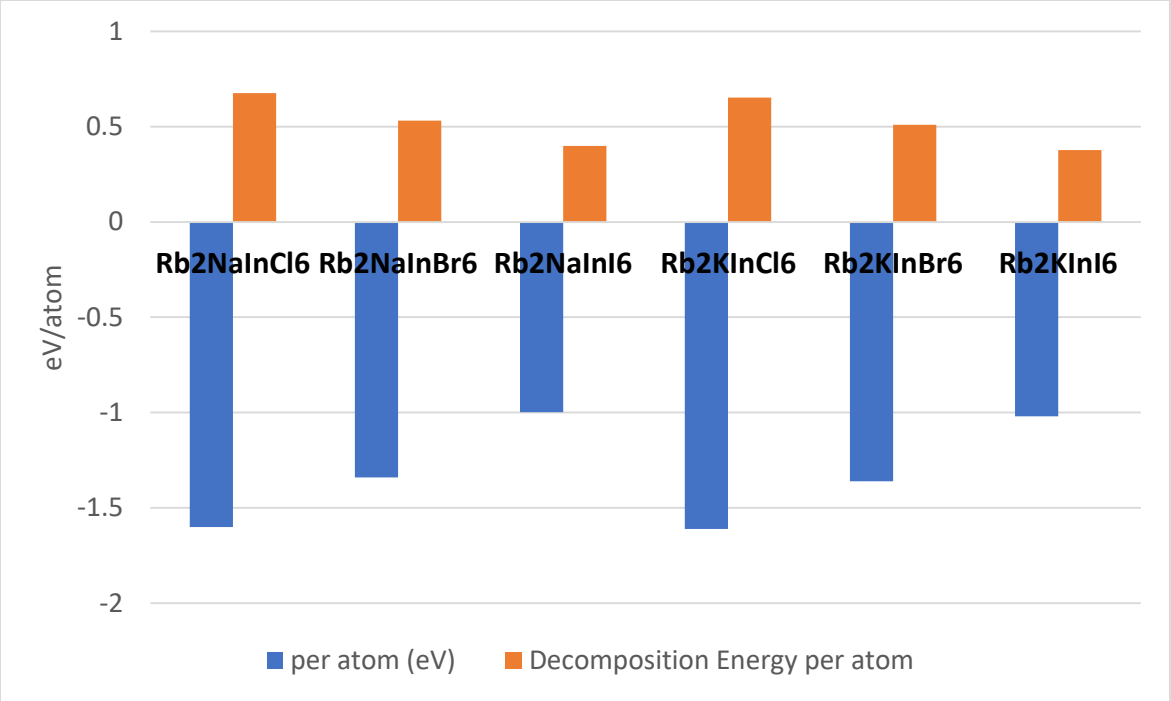

Figure 5-30. Thermodynamic stability of proposed perovskites

5.5 CRYSTALLOGRAPHIC PROPERTIES

Crystallographic properties of this group of perovskites were determined by powder diffraction pattern simulation in VESTA as shown in Fig. 5-31. The fact that all of the perovskites display similar Miller indices on the diffraction pattern, indicates that they all have similar structural characteristics.

Calculations of the electron localization function (ELF) were used to determine the nature of chemical bonds which is shown in Fig. 5-32. The projection in the [010] direction on (0 0 2) plane was chosen because it comprehensively reflects the bonding properties of all the different atoms. Low localization of electrons is indicated by the ELF's small values (~0). When this occurs between two atoms, it means that there has been very little electron localization between the atoms, indicating that they are ionic and forming an ionic bond. The covalent nature of the bond between the atoms is indicated by the electrons being localized within the two atoms with a high density as the ELF value approaches 1.

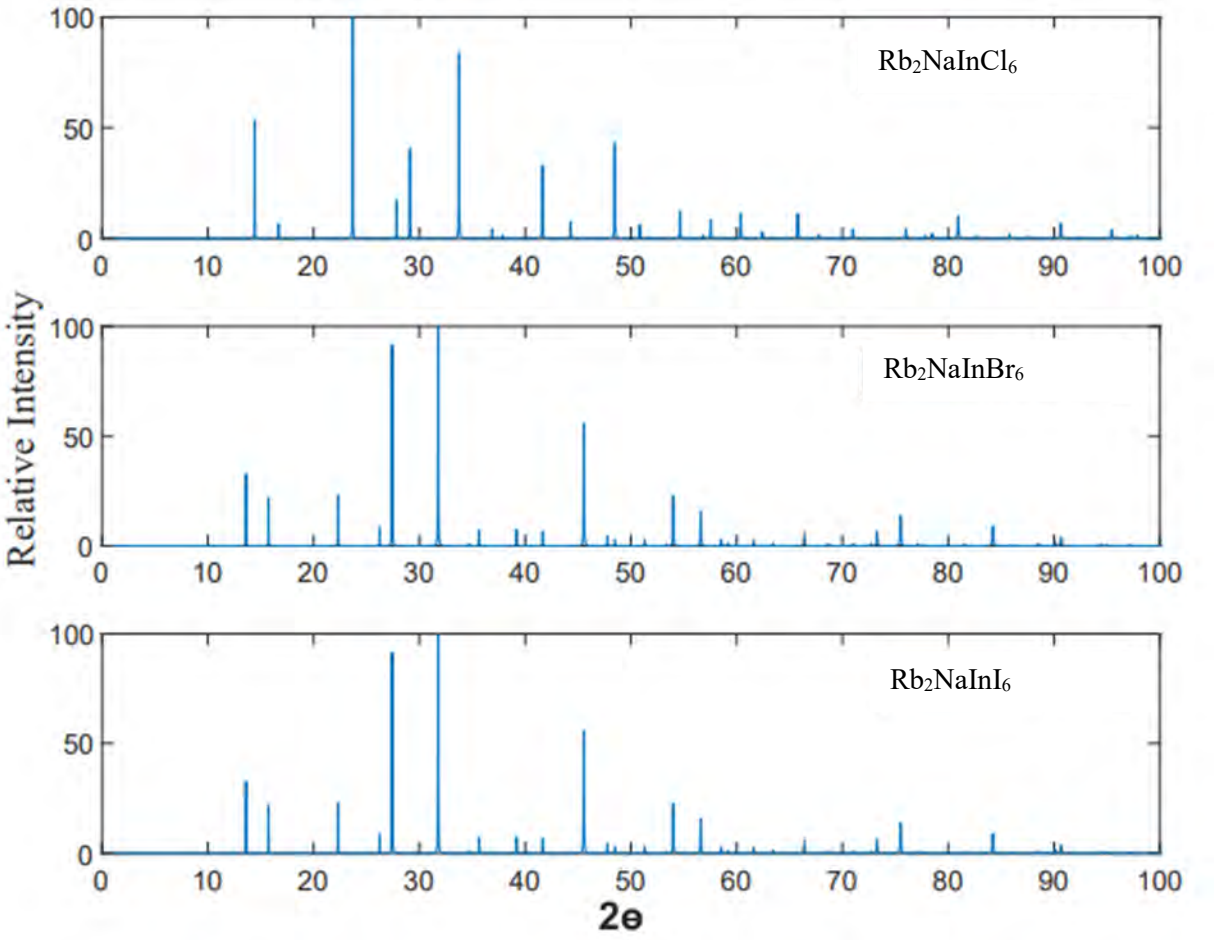

Figure 5-31 Calculated powder diffraction pattern

As shown in Fig. 5-32, it is discovered that the localization of electrons between In and Halogen points to the In-X bond's covalent nature. This improves both the electron transport property and structural stability. Since the localization increases from Cl to Br to I, the covalent nature of the In-X bonds shows the following trend: In-I > In-Br > In-Cl . No electron localization between Na and a halogen indicates that the Na-X bonds are ionic. Further, it can be concluded that all of the perovskites in this group have similar types of bonding between similar atoms.

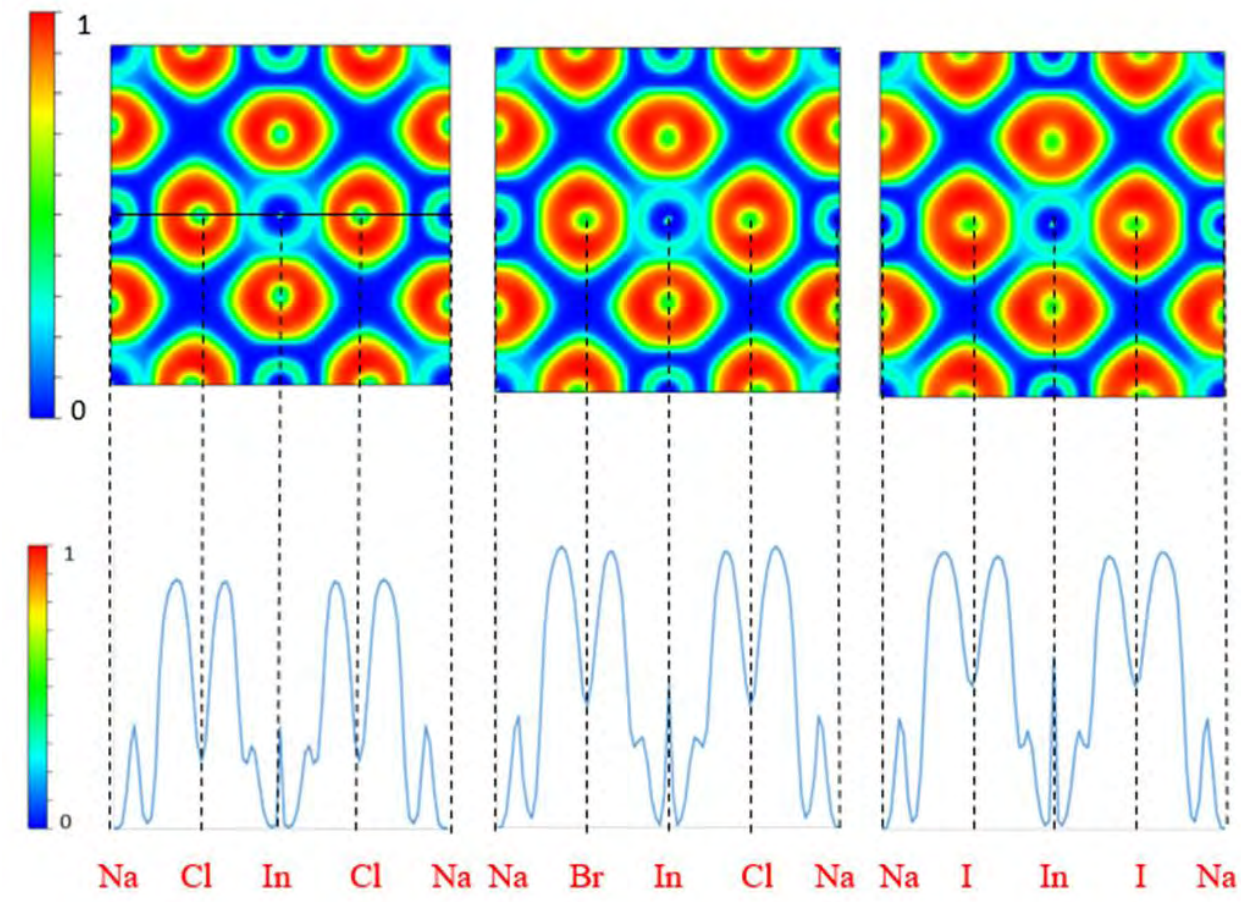

Figure 5-32 Calculated electron localization function (ELF) projected in the (002) plane and [010] direction.

5.6 ELECTRONIC STRUCTURE

The calculated band structure and density of states (DOS) is shown in Fig. 5-33 and Fig. 5-34 respectively. It can be seen in the band structure that both the conduction band minima (CBM) and valence band maxima (VBM) are located at Γ point and both the conduction band and valance band are split. The splitting of VB and CB is caused by the substantial electronegativity difference between In (1.78) and Na (0.93). Compared to valence bands, conduction bands have a much wider energy gap between two adjacent energy levels.

To understand the band structure and the contribution of each element and its orbitals at different energies, the projected density of states (PDOS) has also been calculated (shown in Fig. 5-34).

According to the PDOS, halogen (X) alone contributes to VBM, while X and indium (In) both contribute to CBM. To determine the orbital contributions in the band, additional PDOS calculations are made for various orbitals of X and In. It is found that hybridization between the X-nP orbital and the In-5s orbital makes up the lower portion of the conduction band. Rubidium has no contribution to CBM and contributes to higher energy levels. The higher conduction band is made up of Na, Rb, and In 5p states. The energy position of the conduction band depends on the hybridization level. The lower portion of the conduction band for all the compounds has nearly the same width, and with respect to the fermi energy level, they are positioned around energies between 3 and 4.5 eV for $Rb_2NaInCl_6$, 1.8 and 3.5 eV for $Rb_2NaInBr_6$ and 0.65 and 2.0 eV for Rb_2NaInI_6. Due to strong hybridization between Cl 3p and In 5s orbitals, the CBM of $Rb_2NaInCl_6$ is positioned at a higher energy level compared to Rb2NaInBr6 that has a less strong hybridization between Br 4p and In 5s orbitals. In case of Rb_2NaInI_6, the hybridization between I 5p and In 5s is weak and thus the CBM is positioned at even a lower energy level. To further confirm this trend, the absolute energy position was calculated with respect to vacuum, which is given in Table 5-19.

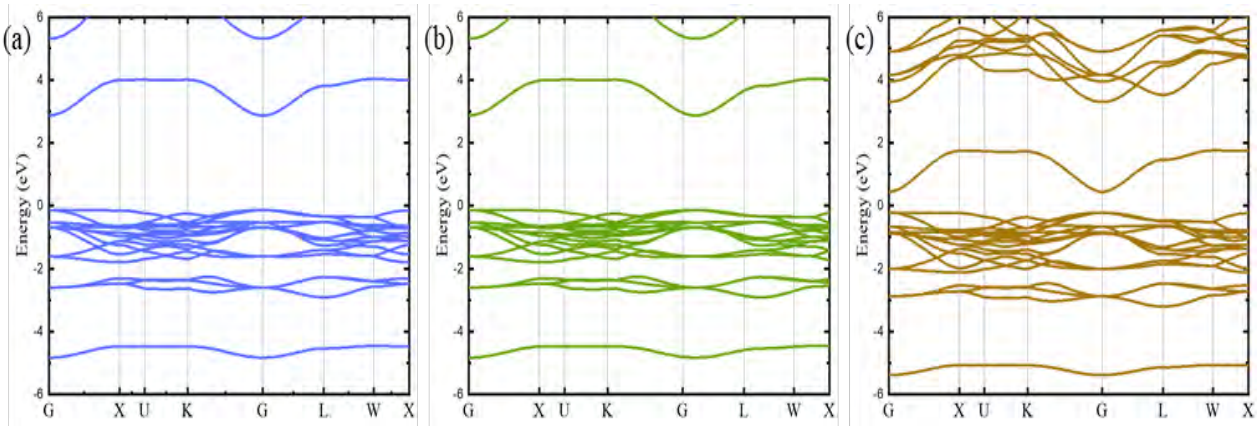

Figure 5-33 Calculated electronic band structures of $Rb_2NaInCl_6$, $Rb_2NaInBr_6$ and Rb_2NaInI_6 respectively. (The VBM energy level is shifted to zero)

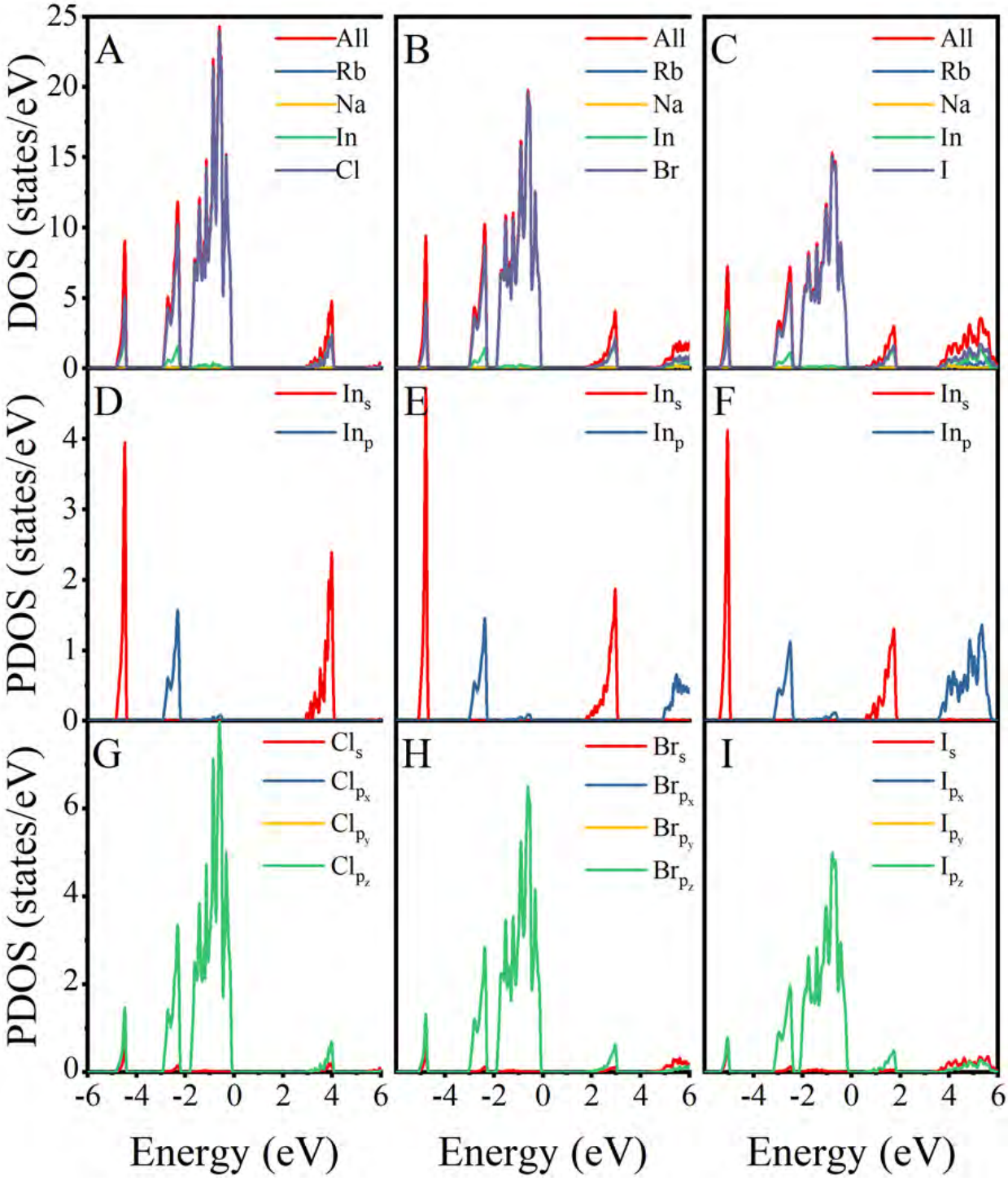

Figure 5-34 Calculated Density of States (DOS) and Projected Density of states (PDOS) of the perovskites. (The VBM energy level is shifted to zero)

Table 5-19 Calculated Fermi energy, valence band maxima (VBM), and conduction band minima (CMB) with respect to vacuum for the proposed perovskites.

Perovskite	Location of VBM	Location of CBM	Nature of band gap	Band gap (eV)	Fermi Energy position	VBM Energy position	CBM Energy position
$Rb_2NaInCl_6$	Gamma	Gamma	Direct	3.01	-5.58	-5.81	-2.80
$Rb_2NaInBr_6$	Gamma	Gamma	Direct	1.81	-4.76	-4.98	-3.18
Rb_2NaInI_6	Gamma	Gamma	Direct	0.66	-4.37	-4.52	-3.86

The valence band is split into three different portions. The top portion of the valence band is mainly contributed by the Cl-3p, Br-4p, and I-5p orbitals for $Rb_2NaInCl_6$, $Rb_2NaInBr_6$ and Rb_2NaInI_6 respectively and has a width of about 2 eV for all of the perovskites. Because of the gradual rise in p orbital energy from Cl to Br to I, the energy level of the VBM is gradually lifted. The hybridization of In-5p with Cl-3p, Br-4p, and I-5p orbitals for $Rb_2NaInCl_6$, $Rb_2NaInBr_6$ and Rb_2NaInI_6r respectively creates the middle portion of the valence band that has narrow width of approximately 1 eV. The deepest portion of the valence band is formed by the hybridization of In-5s with Cl-3p, Br-4p, and I-5p orbitals for $Rb_2NaInCl_6$, $Rb_2NaInBr_6$ and Rb_2NaInI_6r respectively but with a very narrow width compared to the other two portions.

Hybridization between In-5s and X-p solely forms the conduction band minima with the following trend in the hybridization strength, In-5s:Cl-3p > In-5s:Br-4p > In-5s:I-5p. No contribution from Na makes the CBM at the gamma point while VBM is located at the gamma point as a result of being formed solely by the np orbital of the halogen without any hybridization. This makes all the proposed perovskites direct band gap materials.

So, we can observe two main causes for the band gap value to decrease as the ionic size of the halide increases (Cl < Br < I). The first is the rise in the VBM level as a result of an increase in the p orbital energy, while the second is the decrease in CBM energy as a result of weak hybridization between In-5s and X-np orbitals as it walks from Cl to Br to I.

5.7 EFFECTIVE MASS AND MOBILITY

The carrier effective masses can be calculated from the second order parabolic curve fitting at the edge of the VBM and CBM by using the following equation:

$$\frac{1}{m^*} = \frac{1}{h^2} \cdot \frac{\partial^2 E(k)}{\partial k^2}$$

Where, m* is the effective mass, k is the wave-vector and E(k) is the eigenvalue. In this study, the effective mass is calculated by parabolic fitting the band edges in the three following directions, Γ > X, Γ> L and Γ > K and is given in Table 5-20. These perovskites all have low electron effective masses (less than 1 m_0), which indicates that photo-generated electrons have high mobility and are suitable for solar cells. However, they have a slightly higher hole effective mass (greater than 1 m_0), which indicates poor photo-generated hole mobility and is not good for solar cells. Low electron effective mass comes from a steeper band at CBM due to strong hybridization between In-5s and X-np states. On the other hand, because there is no hybridization at VBM, the flat valence band dispersion leads to the higher hole effective mass. The electron and hole effective masses decrease from $Rb_2NaInCl_6$ to $Rb_2NaInBr_6$ to Rb_2NaInI_6, just like band gaps. All of these perovskites have lower electron effective masses but much higher hole effective masses than that of $MAPbI_3$.

Table 5-20 Calculated electron and hole effective masses at different directions for the proposed perovskites.

Perovskite	Directions					
	Γ > X		Γ > L		Γ > K	
	Electron effective mass	Hole effective mass	Electron effective mass	Hole effective mass	Electron effective mass	Hole effective mass
$Rb_2NaInCl_6$	0.525	-3.180	0.525	-3.497	0.525	-3.629
$Rb_2NaInBr_6$	0.349	-2.926	0.349	-3.233	0.349	-3.361
Rb_2NaInI_6	0.274	-2.171	0.274	-2.411	0.274	-2.513

5.8 DIELECTRIC AND OPTICAL PROPERTIES

Frequency dependent dielectric properties of all the perovskites were calculated using VASP. The ab-initio program calculates this property after determining the electronic ground state. The sum of the following equation over the empty states yields the imaginary portion of the dielectric constant.

$$\varepsilon^2_{\alpha\beta}(\omega) = \frac{4\pi^2 e^2}{\Omega} \lim_{q\to 0} \frac{1}{q^2} \sum_{c,v,k} 2w_k \delta(\varepsilon_{ck} - \varepsilon_{vk} - \omega) \, X \, \langle u_{ck+e_\alpha q} | u_{vk} \rangle \langle u_{ck+e_\beta q} | u_{vk} \rangle^*$$

Where the indexes c and v stand for conduction band states and valence band states, respectively, and u_{ck} is the cell periodic portion of the orbitals at the k-point k, ω denotes the angular frequency

of electromagnetic (EM) radiations. The imaginary part of the dielectric constant, ε2(ω), is related to the light absorption behavior of the materials.

To calculate the real part of the dielectric function, Kramers-Kronig correlation [124] is used which represents the degree of polarization of a medium under the application of an external field and is shown in the following equation:

$$\varepsilon^1_{\alpha\beta}(\omega) = 1 + \frac{2}{\pi} P\int_0^{\infty} \frac{\varepsilon^2_{\alpha\beta}(\omega')\omega'}{\omega'^2 - \omega^n + i\eta}\, d\omega'$$

The total dielectric constant is complex and can be calculated as follows [125]:

$$\varepsilon\ (\omega) = \varepsilon^1_{\alpha\beta}(\omega) + i\ \varepsilon^2_{\alpha\beta}(\omega)$$

Fig. 5-35a and 5-35b show the real part, $\varepsilon_1(\omega)$ and imaginary part, $\varepsilon_2(\omega)$ of the dielectric constant respectively. For Rb2NaInCl6, Rb2NaInBr6, and Rb2NaInI6, the static dielectric constants—or the values of the real part of the dielectric constant at zero frequency, $\varepsilon_1(0)$—are 2.0647, 2.4783, and 3.2146, respectively. As the band gap decreases, the static dielectric constant, $\varepsilon_1(0)$ rises from $Rb_2NaInCl_6$ to $Rb_2NaInBr_6$ to Rb_2NaInI_6. This increasing of $\varepsilon_1(0)$ can be explained by the Penn's model in which static value $\varepsilon_1(0)$ and band gap (E_g)are related according to the following equation.

$$\varepsilon_1(0) \approx 1 + (\frac{\hbar\omega_p}{E_g})^2$$

Where, ω_p is plasma frequency and ħ is reduced Planck constant. For all perovskites, ε1(ω) increases with increasing the value of energy and the maximum dispersion of light at resonance frequency for energies of 3.52 eV/5.93 eV, 2.83 eV/4.83 eV and 1.15eV/ 3.82 eV $Rb_2NaInCl_6$, $Rb_2NaInBr_6$ and Rb_2NaInI_6 respectively. The peak value increases from $Rb_2NaInCl_6$ to $Rb_2NaInBr_6$ to Rb_2NaInI_6 but the energy position for the maximum value decreases. After reaching the maximum value, it rapidly decreases until it reaches a minimum in the negative range before bouncing back to the unit value at high energy.

The frequency-dependent linear optical properties like absorption coefficient α(ω), refractive index n(ω), extinction coefficient κ(ω), reflectivity R(ω), and energy-loss function L(ω) for all the

perovskites in this group were calculated from the real ε1(ω) and ε2(ω) parts of the dielectric function [124]as shown in Fig. 5-35.

The optical absorption of a material depends on the interaction between the valence band electrons and phonons. When light rays pass through a material, the absorption coefficient determines the thickness of the material needed to absorb a specific amount of light with a specific energy. For a solar absorber to absorb at least 80% of the light incident within a thickness of 1 μm, the absorption coefficient must be greater than 10^4 cm^{-1}.

As seen in Fig. 5-35c, starting at energies of 3.03 eV, 1.85 eV, and 0.88 eV for $Rb_2NaInCl_6$, $Rb_2NaInBr_6$ and Rb_2NaInI_6 respectively, the absorption coefficient value rises quickly from the absorption edge to reach a maximum and then drops again to a value close to 0. The conduction band splitting is the cause of this abrupt decrease in the absorption coefficient. Both $Rb_2NaInBr_6$ and Rb_2NaInI_6 have weak absorption at their absorption edges, which causes them to have poor absorption in this region. The absorption of $Rb_2NaInCl_6$ begins just at the end of the visible range. So, this will not absorb light in this region. The perovskites, however, have high UV absorption. The beginning of the absorption and its shape also support the perovskites' band structure and band gap. Compared to $MAPbI_3$, these perovskites have a different absorption shape.

We calculate the refractive index of the perovskite, and the complex refractive index is represented by $\dot{n} = n(\omega) + ik(\omega)$, where n(ω) is the refractive index of the perovskites that determine the dispersion of the incident light, and the complex part, k(ω), is the extinction coefficient. The n(ω) and k(ω) follow similar trends as the $\varepsilon_1(\omega)$ and $\varepsilon_2(\omega)$ respectively as shown in Fig. 5-35d and 5-35e. The refractive index increases with energy and reaches a maximum with an interim downfall and then starts to increase again reaching a steady value at high energy. The frequency or energy position of the maxima decreases while maxima increases as moving from $Rb_2NaInCl_6$ to $Rb_2NaInBr_6$ to Rb_2NaInI_6r. The region where the refractive index value is less than the extinction coefficient value indicates that there is no photon transmission in this energy range within the material. The static refractive index n(0) of the perovskites have a value of 2.56, 2.98 and 3.63 for $Rb_2NaInCl_6$, $Rb_2NaInBr_6$ and Rb_2NaInI_6 respectively.

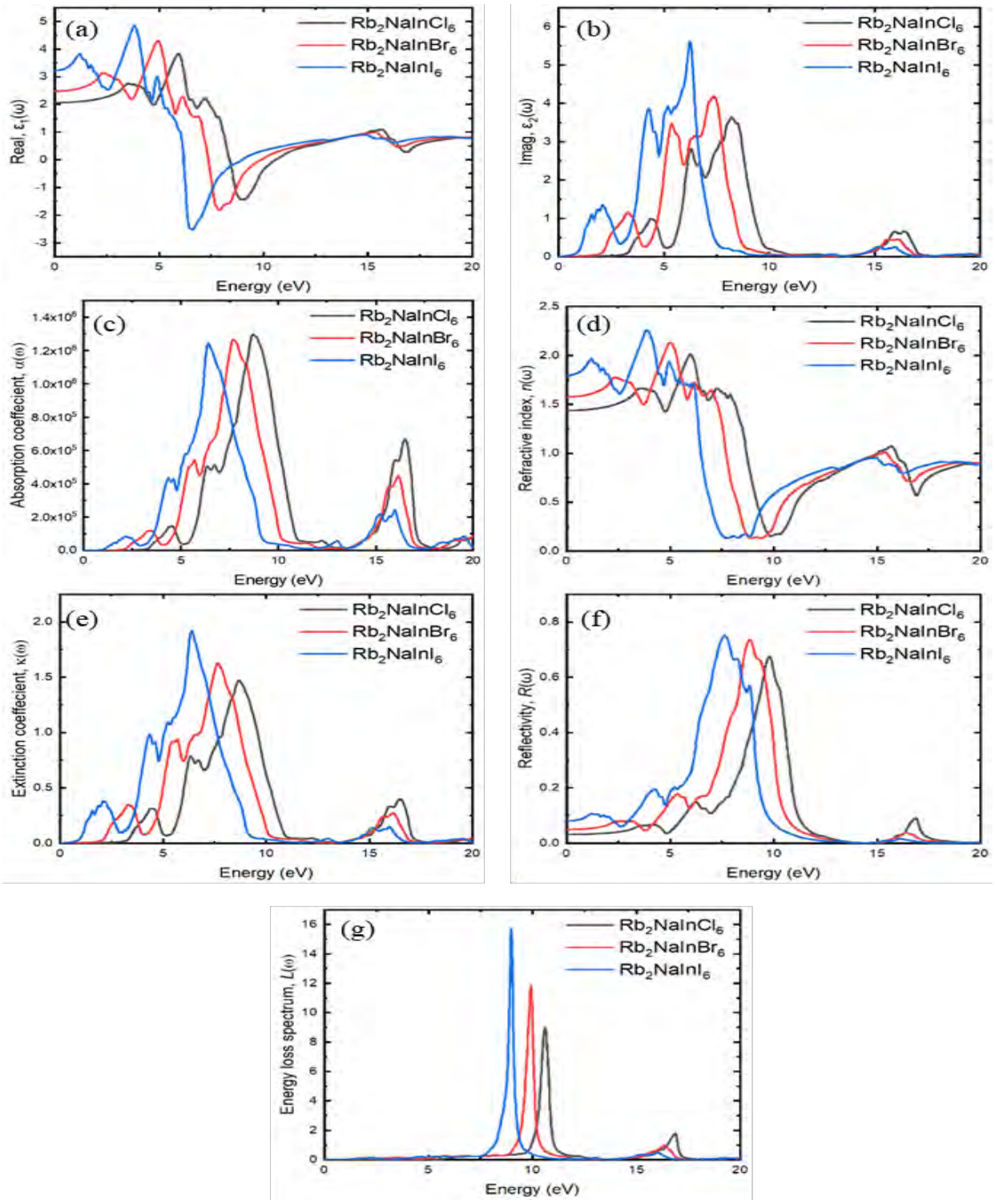

Figure 5-35 . Calculated optical properties of the perovskites. Here (a) and (b) real and imaginary part of the dielectric respectively, (c) absorption coefficient, (d) refractive index, (e) extinction coefficient, (f) reflectivity and (g) energy loss spectrum.

Fig. 5-35f shows the reflectivity of the perovskites in different energy ranges. As can be seen, the maximum reflectivity for $Rb_2NaInCl_6$, $Rb_2NaInBr_6$ and Rb_2NaInI_6 was found at energies around 9.87 eV, 8.95 eV, and 7.73 eV, respectively, while the reflectivity at the visible range was below 5%, 8%, and 11%. This is consistent with the refractive index and extinction coefficient shown in Fig. 5-35d and Fig. 5-35e. Maximum values of the reflectivity in the range 0 to 6 eV is below 25%, which indicates that most of the photons with energy in this region will be absorbed or transmitted through the materials.

Fig. 5-35g. shows the energy loss spectrum of the perovskites in different energy ranges, which reveals the loss of a electron's energy as it passes through the respected perovskite. Maximum loss is discovered to occur for $Rb_2NaInCl_6$, $Rb_2NaInBr_6$ and Rb_2NaInI_6 at energies between 10 and 11 eV, 9 to 10.5 eV, and 8 to 9.5 eV, respectively. The highest value below 7 eV is found to be around 0.25. This indicates a very small energy loss at lower energy levels.

5.10 PHOTOCATALYSIS

Photocatalytic water splitting, which generates H_2 as a clean and renewable energy source, is another way to use solar energy. The majority of H_2 is currently produced using fossil fuels, which results in CO_2 emissions as a byproduct [126]. If the cost of photocatalytic water splitting can be decreased by developing new materials, it may eventually replace other methods of producing H_2.

Photocatalytic actions of a materials are also held as like solar cell mechanism. For a semiconductor to function as a photocatalyst, incident photons must have an energy (v) greater than the band gap (Eg) of the materials. This incident ray (photons) will interact with the electron and lift it to the conduction band to produce a free electron in the conduction band leaving behind a hole in the valence band. This electron and hole will transport to the photocatalyst surfaces and participate in photo-oxidation and reduction, respectively.

To complete this photo-induced redox reaction, the energy positions of the VBM and CBM must be compatible with the absolute redox potentials of the oxidation and reduction reactions, respectively. The redox potential of water splitting reactions depends on the P^H value [127] [128]. The energy of the photoexcited electron must be higher than the redox potential of the photo-

oxidation reaction on the absolute vacuum scale for spontaneous reaction, and the energy position (with respect to vacuum) of the VB edge must be lower (more negative) than the redox potential of the photo-reduction reaction. The following two equations can be used to determine the P^H-dependent standard redox potential of the oxidation and reduction reaction in water splitting reaction:

$$E^{red}_{H^+/H_2} = -4.44\ eV + P^H \text{ X } 0.059 \text{ eV}$$

$$E^{ox}_{O_2/H_2O} = -5.67\ eV + P^H \text{ X } 0.059 \text{ eV}$$

The calculated oxidation and reduction potentials and the viability of photocatalysis of the proposed perovskites is shown in Fig. 5-37.

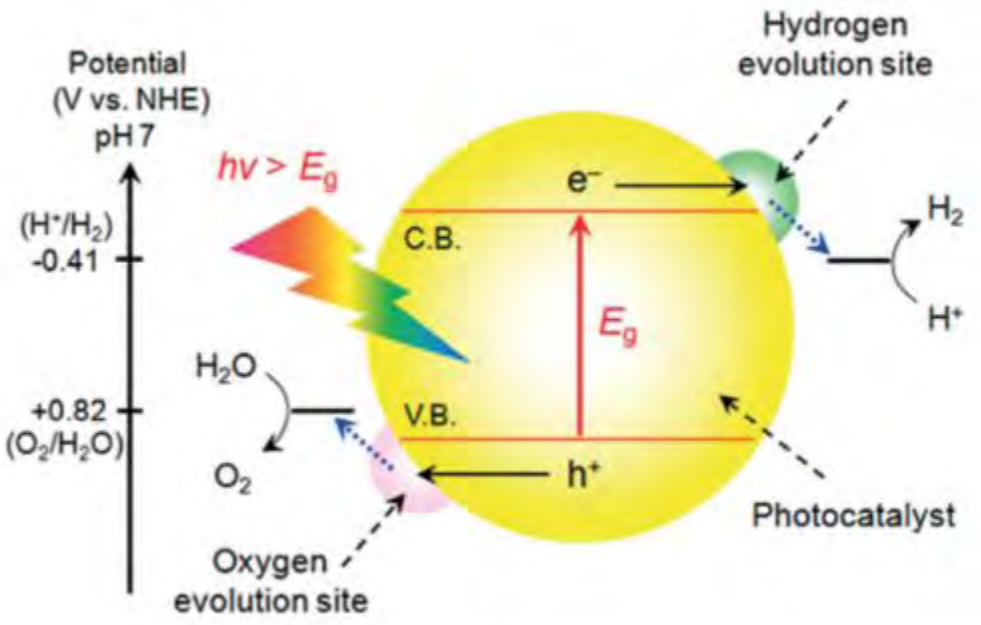

Figure 5-36 Mechanism of Photocatalysis.

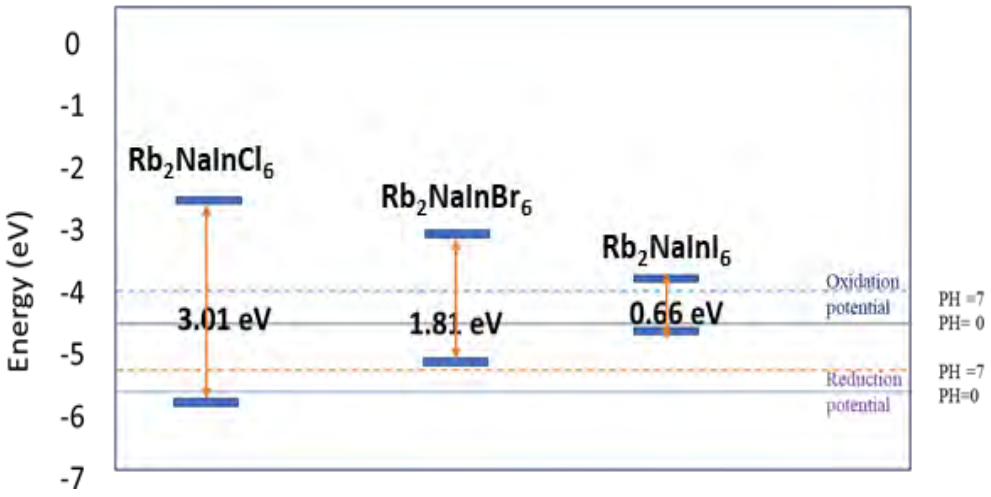

Figure 5-37 viability of Photocatalysis for the proposed perovskite group.

From figure 5-37, it is found that $Rb_2NaInCl_6$ can be used as a photocatalyst in both neutral or acidic condition due to having favorable VBM and CBM energies for spontaneous reaction. Both $Rb_2NaInBr_6$ and Rb_2NaInI_6 have has favorable CBM energy for spontaneous photo-oxidation reaction in water splitting, however, the VBM energy cannot lead to a spontaneous photo-reduction reaction. That's why $Rb_2NaInBr_6$ and Rb_2NaInI_6 may not be used solely as a photocatalyst in a Hydrogen evolution from water splitting but can be used by coupling with others.

CAPTER 6: CONCLUSION

6.1 CONCLUSION

The structural, mechanical, electronic, dielectric and optical properties are calculated for the mechanically and thermodynamically stable cubic perovskites of Rb_2MInX_6 (where, M = Li, Na, K and X= Cl, Br, I), by using the First Principle DFT analysis in GGA-PBE method. To the best knowledge of the author, the theoretical analysis of Rb_2MInX_6 perovskites has been done for the first time. Any theoretical or experimental analysis has not been done before.

It is expected from this analysis, the cubic phase of Lithium (Li) based perovskites, Rb_2LiInX_6, aren't stable at room temperature due to failing to meet the critical values for the octahedral factor (found < 0.40 but expected value is 0.44-0.90). Noncubic perovskites have lower symmetry that affects the band structure and mobility of the perovskites and hampered the photovoltaic properties. Potassium-based perovskites, Rb_2KInX_6, are structurally and thermodynamically stable but don't have mechanical stability due to having negative value of C44 (expected value C44>0). But Sodium-based perovskites, Rb_2NaInX_6, satisfy the structural tolerance value that ensures the stable cubic phase of those perovskites, have negative formation energies and stability against decomposition that ensure thermodynamic stability and also satisfy the mechanical stability requirements. That indicates the best stability of Na-based perovskites.

That's why the structural, mechanical, electronic, dielectric, and optical properties are calculated only for the Rb_2NaInX_6, a stable noble nontoxic group of perovskites. It has been found that all perovskites in this group exhibit semiconducting behavior with a direct band gap and have favorable photovoltaic properties. All of them have a Paugh's ratio > 1.75, nonnegative Cauchy pressure, and position's ratio higher than 0.26, all of which point to the perovskites' ductility, while a higher Debye temperature value reveals the materials' stability at high temperatures. Both $Rb_2NaInBr_6$ and Rb_2NaInI_6 perovskites are suitable for use in tandem solar cells due to their strong light absorption, small effective electron mass for mobility, and suitable direct band gap (Eg <2.0 eV). Along with having a direct band gap of 3.01 eV, strong UV absorption, a suitable electron effective mass for mobility, and VBM and CBM energies matching the oxidation and reduction potentials of water splitting, $Rb_2NaInCl_6$ is a candidate for use as a photocatalyst in the production of hydrogen from water splitting.

6.2 SCOPE FOR FUTURE INVESTIGATIONS

The following recommendations for future research work may be suggested:

- DFT analysis of those perovskites to determine the suitability of the perovskite to be used as Scintillator, Light emitter, etc.
- Modification of those perovskites by doping to modify the electronic properties to improve hole mobility
- Interface analysis of those to investigate the interfacial analysis and charge transfer through the interface and finding out of the interfacial properties
- Full cell simulation in SCAPS by taking those perovskites as a light absorber.

References:

[1] W. A. Hermann, "Quantifying global exergy resources," *Energy*, vol. 31, no. 12, pp. 1685–1702, 2006.

[2] R. E. H. Sims, H.-H. Rogner, and K. Gregory, "Carbon emission and mitigation cost comparisons between fossil fuel, nuclear and renewable energy resources for electricity generation," *Energy Policy*, vol. 31, no. 13, pp. 1315–1326, Oct. 2003, doi: 10.1016/S0301-4215(02)00192-1.

[3] L. Zheng *et al.*, "A universal all-solid synthesis for high throughput production of halide perovskite," *Nat. Commun.*, vol. 13, no. 1, Art. no. 1, Dec. 2022, doi: 10.1038/s41467-022-35122-7.

[4] N.-G. Park, M. Grätzel, T. Miyasaka, K. Zhu, and K. Emery, "Towards stable and commercially available perovskite solar cells," *Nat. Energy*, vol. 1, no. 11, Art. no. 11, Oct. 2016, doi: 10.1038/nenergy.2016.152.

[5] T. M. Brenner, D. A. Egger, L. Kronik, G. Hodes, and D. Cahen, "Hybrid organic—inorganic perovskites: low-cost semiconductors with intriguing charge-transport properties," *Nat. Rev. Mater.*, vol. 1, no. 1, Art. no. 1, Jan. 2016, doi: 10.1038/natrevmats.2015.7.

[6] S. De Wolf *et al.*, "Organometallic Halide Perovskites: Sharp Optical Absorption Edge and Its Relation to Photovoltaic Performance," *J. Phys. Chem. Lett.*, vol. 5, no. 6, pp. 1035–1039, Mar. 2014, doi: 10.1021/jz500279b.

[7] L. Yue, B. Yan, M. Attridge, and Z. Wang, "Light absorption in perovskite solar cell: Fundamentals and plasmonic enhancement of infrared band absorption," *Sol. Energy*, vol. 124, pp. 143–152, Feb. 2016, doi: 10.1016/j.solener.2015.11.028.

[8] S. D. Stranks *et al.*, "Electron-Hole Diffusion Lengths Exceeding 1 Micrometer in an Organometal Trihalide Perovskite Absorber," *Science*, vol. 342, no. 6156, pp. 341–344, Oct. 2013, doi: 10.1126/science.1243982.

[9] C. Wehrenfennig, G. E. Eperon, M. B. Johnston, H. J. Snaith, and L. M. Herz, "High Charge Carrier Mobilities and Lifetimes in Organolead Trihalide Perovskites," *Adv. Mater.*, vol. 26, no. 10, pp. 1584–1589, 2014, doi: 10.1002/adma.201305172.

[10] L. M. Herz, "Charge-Carrier Mobilities in Metal Halide Perovskites: Fundamental Mechanisms and Limits," *ACS Energy Lett.*, vol. 2, no. 7, pp. 1539–1548, Jul. 2017, doi: 10.1021/acsenergylett.7b00276.

[11] R. E. Brandt, V. Stevanović, D. S. Ginley, and T. Buonassisi, "Identifying defect-tolerant semiconductors with high minority-carrier lifetimes: beyond hybrid lead halide perovskites," *MRS Commun.*, vol. 5, no. 2, pp. 265–275, Jun. 2015, doi: 10.1557/mrc.2015.26.

[12] A. Walsh, D. O. Scanlon, S. Chen, X. G. Gong, and S.-H. Wei, "Self-Regulation Mechanism for Charged Point Defects in Hybrid Halide Perovskites," *Angew. Chem. Int. Ed.*, vol. 54, no. 6, pp. 1791–1794, 2015, doi: 10.1002/anie.201409740.

[13] K. Ren *et al.*, "Metal halide perovskites for photocatalysis applications," *J. Mater. Chem. A*, vol. 10, no. 2, pp. 407–429, 2022, doi: 10.1039/D1TA09148D.

[14] L. Chu *et al.*, "Lead-Free Halide Double Perovskite Materials: A New Superstar Toward Green and Stable Optoelectronic Applications," *Nano-Micro Lett.*, vol. 11, no. 1, p. 16, Dec. 2019, doi: 10.1007/s40820-019-0244-6.

[15] J. D. Majher, M. B. Gray, T. A. Strom, and P. M. Woodward, "Cs2NaBiCl6:Mn2+—A New Orange-Red Halide Double Perovskite Phosphor," *Chem. Mater.*, vol. 31, no. 5, pp. 1738–1744, Mar. 2019, doi: 10.1021/acs.chemmater.8b05280.

[16] S. D. Stranks and H. J. Snaith, "Metal-halide perovskites for photovoltaic and light-emitting devices," *Nat. Nanotechnol.*, vol. 10, no. 5, pp. 391–402, May 2015, doi: 10.1038/nnano.2015.90.

[17] X. Hu *et al.*, "High-Performance Flexible Broadband Photodetector Based on Organolead Halide Perovskite," *Adv. Funct. Mater.*, vol. 24, no. 46, pp. 7373–7380, 2014, doi: 10.1002/adfm.201402020.

[18] Y. Zhou, J. Chen, O. M. Bakr, and O. F. Mohammed, "Metal Halide Perovskites for X-ray Imaging Scintillators and Detectors," *ACS Energy Lett.*, vol. 6, no. 2, pp. 739–768, Feb. 2021, doi: 10.1021/acsenergylett.0c02430.

[19] "Halide perovskite memristors as flexible and reconfigurable physical unclonable functions | Nature Communications." https://www.nature.com/articles/s41467-021-24057-0 (accessed Dec. 01, 2022).

[20] A. Kojima, K. Teshima, Y. Shirai, and T. Miyasaka, "Organometal Halide Perovskites as Visible-Light Sensitizers for Photovoltaic Cells," *J. Am. Chem. Soc.*, vol. 131, no. 17, pp. 6050–6051, May 2009, doi: 10.1021/ja809598r.

[21] H. Min *et al.*, "Perovskite solar cells with atomically coherent interlayers on SnO2 electrodes," *Nature*, vol. 598, no. 7881, Art. no. 7881, Oct. 2021, doi: 10.1038/s41586-021-03964-8.

[22] T. A. Berhe *et al.*, "Organometal halide perovskite solar cells: degradation and stability," *Energy Environ. Sci.*, vol. 9, no. 2, pp. 323–356, 2016, doi: 10.1039/C5EE02733K.

[23] B. Park and S. I. Seok, "Intrinsic Instability of Inorganic–Organic Hybrid Halide Perovskite Materials," *Adv. Mater.*, vol. 31, no. 20, p. 1805337, May 2019, doi: 10.1002/adma.201805337.

[24] M. Saliba *et al.*, "Incorporation of rubidium cations into perovskite solar cells improves photovoltaic performance," *Science*, vol. 354, no. 6309, pp. 206–209, Oct. 2016, doi: 10.1126/science.aah5557.

[25] F. Ünlü *et al.*, "Understanding the interplay of stability and efficiency in A-site engineered lead halide perovskites," *APL Mater.*, vol. 8, no. 7, p. 070901, Jul. 2020, doi: 10.1063/5.0011851.

[26] J. K. Nam, D. H. Chun, R. J. K. Rhee, J. H. Lee, and J. H. Park, "Methodologies toward Efficient and Stable Cesium Lead Halide Perovskite-Based Solar Cells," *Adv. Sci.*, vol. 5, no. 8, p. 1800509, 2018, doi: 10.1002/advs.201800509.

[27] M. Wang *et al.*, "Lead-Free Perovskite Materials for Solar Cells," *Nano-Micro Lett.*, vol. 13, no. 1, p. 62, Jan. 2021, doi: 10.1007/s40820-020-00578-z.

[28] M. Zhang *et al.*, "Recent progress in inorganic tin perovskite solar cells," *Mater. Today Energy*, vol. 23, no. 100891, Jan. 2022, doi: 10.1016/j.mtener.2021.100891.

[29] S. Ghosh, H. Shankar, and P. Kar, "Recent developments of lead-free halide double perovskites: a new superstar in the optoelectronic field," *Mater. Adv.*, vol. 3, no. 9, pp. 3742–3765, 2022, doi: 10.1039/D2MA00071G.

[30] H. Lei, D. Hardy, and F. Gao, "Lead-Free Double Perovskite Cs2AgBiBr6: Fundamentals, Applications, and Perspectives," *Adv. Funct. Mater.*, vol. 31, no. 49, p. 2105898, 2021, doi: 10.1002/adfm.202105898.

[31] Z. Zhang *et al.*, "Hydrogenated Cs2AgBiBr6 for significantly improved efficiency of lead-free inorganic double perovskite solar cell," *Nat. Commun.*, vol. 13, no. 1, Art. no. 1, Jun. 2022, doi: 10.1038/s41467-022-31016-w.

[32] S. Ghosh, G. K. Nim, H. Shankar, and P. Kar, "Probing the emissive behaviour of the lead-free Cs2AgBiCl6 double perovskite with Cu(II) doping," *New J. Chem.*, vol. 45, no. 48, pp. 22691–22696, Dec. 2021, doi: 10.1039/D1NJ04518K.

[33] J. E. F. S. Rodrigues *et al.*, "Experimental and Theoretical Investigations on the Structural, Electronic, and Vibrational Properties of Cs2AgSbCl6 Double Perovskite," *Ind. Eng. Chem. Res.*, vol. 60, no. 51, pp. 18918–18928, Dec. 2021, doi: 10.1021/acs.iecr.1c02188.

[34] T. Zuo, F. Qi, C. Yam, and L. Meng, "Lead-free all-inorganic halide double perovskite materials for optoelectronic applications: progress, performance and design," *Phys Chem Chem Phys*, vol. 24, no. 44, pp. 26948–26961, 2022, doi: 10.1039/D2CP03463H.

[35] X. Cao, L. Kang, S. Guo, M. Zhang, Z. Lin, and J. Gao, "Cs2NaVCl6: A Pb-Free Halide Double Perovskite with Strong Visible and Near-Infrared Light Absorption," *ACS Appl. Mater. Interfaces*, vol. 11, no. 42, pp. 38648–38653, Oct. 2019, doi: 10.1021/acsami.9b11980.

[36] R. Zhang *et al.*, "All-Inorganic Rare-Earth Halide Double Perovskite Single Crystals with Highly Efficient Photoluminescence," *Adv. Opt. Mater.*, vol. 9, no. 19, p. 2100689, Oct. 2021, doi: 10.1002/adom.202100689.

[37] M.-M. Yao *et al.*, "Improving Lead-Free Double Perovskite Cs2NaBiCl6 Nanocrystal Optical Properties via Ion Doping," *Adv. Opt. Mater.*, vol. 8, no. 8, p. 1901919, 2020, doi: 10.1002/adom.201901919.

[38] H. Li *et al.*, "Double perovskite Cs2NaInCl6 nanocrystals with intense dual-emission via self-trapped exciton-to-Tb3+ dopant energy transfer," *J. Mater. Chem. C*, vol. 10, no. 29, pp. 10609–10615, Jul. 2022, doi: 10.1039/D2TC01067D.

[39] M. B. Gray, S. Hariyani, T. A. Strom, J. D. Majher, J. Brgoch, and P. M. Woodward, "High-efficiency blue photoluminescence in the Cs2NaInCl6:Sb3+ double perovskite phosphor," *J Mater Chem C*, vol. 8, no. 20, pp. 6797–6803, 2020, doi: 10.1039/D0TC01037E.

[40] M. Shahbazi and H. Wang, "Progress in research on the stability of organometal perovskite solar cells," *Sol. Energy*, vol. 123, pp. 74–87, Jan. 2016, doi: 10.1016/j.solener.2015.11.008.

[41] X. Liu *et al.*, "A high dielectric constant non-fullerene acceptor for efficient bulk-heterojunction organic solar cells," *J. Mater. Chem. A*, vol. 6, no. 2, pp. 395–403, Jan. 2018, doi: 10.1039/C7TA10136H.

[42] V. Tiong *et al.*, "Octadecylamine-functionalized single-walled carbon nanotubes for facilitating the formation of a monolithic perovskite layer and stable solar cells," *Adv. Funct. Mater.*, vol. 28, no. 10, Art. no. 10, 2018.

[43] P. Zhang, J. Yang, and S.-H. Wei, "Manipulation of cation combinations and configurations of halide double perovskites for solar cell absorbers," *J. Mater. Chem. A*, vol. 6, no. 4, pp. 1809–1815, Jan. 2018, doi: 10.1039/C7TA09713A.

[44] "Perovskites Solar Cell Structure, Efficiency & More," *Ossila*. https://www.ossila.com/pages/perovskites-and-perovskite-solar-cells-an-introduction (accessed Dec. 07, 2022).

[45] H.-R. Wenk and A. G. Bulakh, *Minerals: their constitution and origin*. Cambridge ; New York: Cambridge University Press, 2004.

[46] T. Baikie *et al.*, "Synthesis and crystal chemistry of the hybrid perovskite (CH3NH3)PbI3 for solid-state sensitised solar cell applications," *J. Mater. Chem. A*, vol. 1, no. 18, pp. 5628–5641, Apr. 2013, doi: 10.1039/C3TA10518K.

[47] "Unusual defect physics in CH3NH3PbI3 perovskite solar cell absorber: Applied Physics Letters: Vol 104, No 6." https://aip.scitation.org/doi/abs/10.1063/1.4864778 (accessed Dec. 07, 2022).

[48] H.-H. Fang *et al.*, "Ultrahigh sensitivity of methylammonium lead tribromide perovskite single crystals to environmental gases," *Sci. Adv.*, vol. 2, no. 7, p. e1600534, Jul. 2016, doi: 10.1126/sciadv.1600534.

[49] Q. Han *et al.*, "Single Crystal Formamidinium Lead Iodide (FAPbI3): Insight into the Structural, Optical, and Electrical Properties," *Adv. Mater. Deerfield Beach Fla*, vol. 28, no. 11, pp. 2253–2258, Mar. 2016, doi: 10.1002/adma.201505002.

[50] G. E. Eperon, S. D. Stranks, C. Menelaou, M. B. Johnston, L. M. Herz, and H. J. Snaith, "Formamidinium lead trihalide: a broadly tunable perovskite for efficient planar heterojunction solar cells," *Energy Environ. Sci.*, vol. 7, no. 3, pp. 982–988, Feb. 2014, doi: 10.1039/C3EE43822H.

[51] J. H. Noh, S. H. Im, J. H. Heo, T. N. Mandal, and S. I. Seok, "Chemical Management for Colorful, Efficient, and Stable Inorganic–Organic Hybrid Nanostructured Solar Cells," *Nano Lett.*, vol. 13, no. 4, pp. 1764–1769, Apr. 2013, doi: 10.1021/nl400349b.

[52] "Electron-Hole Diffusion Lengths Exceeding 1 Micrometer in an Organometal Trihalide Perovskite Absorber | Science." https://www.science.org/doi/10.1126/science.1243982 (accessed Dec. 01, 2022).

[53] W.-J. Yin, T. Shi, and Y. Yan, "Unique Properties of Halide Perovskites as Possible Origins of the Superior Solar Cell Performance," *Adv. Mater.*, vol. 26, no. 27, pp. 4653–4658, 2014, doi: 10.1002/adma.201306281.

[54] C. Motta, F. El-Mellouhi, S. Kais, N. Tabet, F. Alharbi, and S. Sanvito, "Revealing the role of organic cations in hybrid halide perovskite CH3NH3PbI3," *Nat. Commun.*, vol. 6, no. 1, p. 7026, Nov. 2015, doi: 10.1038/ncomms8026.

[55] J. M. Frost, K. T. Butler, F. Brivio, C. H. Hendon, M. van Schilfgaarde, and A. Walsh, "Atomistic Origins of High-Performance in Hybrid Halide Perovskite Solar Cells," *Nano Lett.*, vol. 14, no. 5, pp. 2584–2590, May 2014, doi: 10.1021/nl500390f.

[56] "Best Research-Cell Efficiency Chart." https://www.nrel.gov/pv/cell-efficiency.html (accessed Dec. 07, 2022).

[57] M. M. Lee, J. Teuscher, T. Miyasaka, T. N. Murakami, and H. J. Snaith, "Efficient hybrid solar cells based on meso-superstructured organometal halide perovskites," *Science*, vol. 338, no. 6107, pp. 643–647, Nov. 2012, doi: 10.1126/science.1228604.

[58] H.-S. Kim *et al.*, "Lead Iodide Perovskite Sensitized All-Solid-State Submicron Thin Film Mesoscopic Solar Cell with Efficiency Exceeding 9%," *Sci. Rep.*, vol. 2, no. 1, Art. no. 1, Aug. 2012, doi: 10.1038/srep00591.

[59] J. M. Ball, M. M. Lee, A. Hey, and H. J. Snaith, "Low-temperature processed meso-superstructured to thin-film perovskite solar cells," *Energy Environ. Sci.*, vol. 6, no. 6, pp. 1739–1743, May 2013, doi: 10.1039/C3EE40810H.

[60] H. Zhou *et al.*, "Interface engineering of highly efficient perovskite solar cells," *Science*, vol. 345, no. 6196, pp. 542–546, Aug. 2014, doi: 10.1126/science.1254050.

[61] J. Chen, S. Zhou, S. Jin, H. Li, and T. Zhai, "Crystal organometal halide perovskites with promising optoelectronic applications," *J. Mater. Chem. C*, vol. 4, no. 1, pp. 11–27, 2016, doi: 10.1039/C5TC03417E.

[62] Y. Wu, X. Li, and H. Zeng, "Lead-Free Halide Double Perovskites: Structure, Luminescence, and Applications," *Small Struct.*, vol. 2, no. 3, p. 2000071, 2021, doi: 10.1002/sstr.202000071.

[63] G. Volonakis *et al.*, "Lead-Free Halide Double Perovskites via Heterovalent Substitution of Noble Metals," *J. Phys. Chem. Lett.*, vol. 7, no. 7, pp. 1254–1259, Apr. 2016, doi: 10.1021/acs.jpclett.6b00376.

[64] Z. Xiao, K.-Z. Du, W. Meng, J. Wang, D. B. Mitzi, and Y. Yan, "Intrinsic Instability of Cs2In(I)M(III)X6 (M = Bi, Sb; X = Halogen) Double Perovskites: A Combined Density Functional Theory and Experimental Study," *J. Am. Chem. Soc.*, vol. 139, no. 17, pp. 6054–6057, May 2017, doi: 10.1021/jacs.7b02227.

[65] B. Yang *et al.*, "Lead-Free Silver-Bismuth Halide Double Perovskite Nanocrystals," *Angew. Chem. Int. Ed Engl.*, vol. 57, no. 19, pp. 5359–5363, May 2018, doi: 10.1002/anie.201800660.

[66] G. Volonakis *et al.*, "Cs2InAgCl6: A New Lead-Free Halide Double Perovskite with Direct Band Gap," *J. Phys. Chem. Lett.*, vol. 8, no. 4, pp. 772–778, Feb. 2017, doi: 10.1021/acs.jpclett.6b02682.

[67] F. Wei *et al.*, "The synthesis, structure and electronic properties of a lead-free hybrid inorganic–organic double perovskite (MA) $_2$ KBiCl $_6$ (MA = methylammonium)," *Mater. Horiz.*, vol. 3, no. 4, pp. 328–332, 2016, doi: 10.1039/C6MH00053C.

[68] Z. Deng, F. Wei, S. Sun, G. Kieslich, A. K. Cheetham, and P. D. Bristowe, "Exploring the properties of lead-free hybrid double perovskites using a combined computational-

experimental approach," *J. Mater. Chem. A*, vol. 4, no. 31, pp. 12025–12029, 2016, doi: 10.1039/C6TA05817E.

[69] G. Volonakis, A. A. Haghighirad, H. J. Snaith, and F. Giustino, "Route to Stable Lead-Free Double Perovskites with the Electronic Structure of $CH_3NH_3PbI_3$: A Case for Mixed-Cation $[Cs/CH_3NH_3/CH(NH_2)_2]_2InBiBr_6$," *J. Phys. Chem. Lett.*, vol. 8, no. 16, pp. 3917–3924, Aug. 2017, doi: 10.1021/acs.jpclett.7b01584.

[70] N. A. Noor *et al.*, "Analysis of direct band gap A2ScInI6 (A=Rb, Cs) double perovskite halides using DFT approach for renewable energy devices," *J. Mater. Res. Technol.*, vol. 13, pp. 2491–2500, Jul. 2021, doi: 10.1016/j.jmrt.2021.05.080.

[71] Y. Saeed *et al.*, "$Cs_2NaGaBr_6$: a new lead-free and direct band gap halide double perovskite," *RSC Adv.*, vol. 10, no. 30, pp. 17444–17451, 2020, doi: 10.1039/D0RA01764G.

[72] "Analysis of direct band gap A2ScInI6 (A=Rb, Cs) double perovskite halides using DFT approach for renewable energy devices - ScienceDirect." https://www.sciencedirect.com/science/article/pii/S2238785421005202?via%3Dihub (accessed Dec. 07, 2022).

[73] Y. Cai *et al.*, "High-throughput Computational Study of Halide Double Perovskite Inorganic Compounds," *Chem. Mater.*, vol. 31, no. 15, pp. 5392–5401, Aug. 2019, doi: 10.1021/acs.chemmater.9b00116.

[74] T.-Y. Tang, X.-H. Zhao, D.-Y. Hu, Q.-Q. Liang, X.-N. Wei, and Y.-L. Tang, "Theoretical exploration of mechanical, electronic structure and optical properties of aluminium based double halide perovskite," *RSC Adv.*, vol. 12, no. 17, pp. 10209–10218, Mar. 2022, doi: 10.1039/D2RA01216B.

[75] Z. Zhang *et al.*, "Potential Applications of Halide Double Perovskite Cs_2AgInX_6 (X = Cl, Br) in Flexible Optoelectronics: Unusual Effects of Uniaxial Strains," *J. Phys. Chem. Lett.*, vol. 10, no. 5, pp. 1120–1125, Mar. 2019, doi: 10.1021/acs.jpclett.9b00134.

[76] A. Menedjhi, N. Bouarissa, S. Saib, and K. Bouamama, "Halide double perovskite Cs2AgInBr6 for photovoltaic's applications: Optical properties and stability," *Optik*, vol. 243, p. 167198, Oct. 2021, doi: 10.1016/j.ijleo.2021.167198.

[77] X.-G. Zhao *et al.*, "Design of Lead-Free Inorganic Halide Perovskites for Solar Cells via Cation-Transmutation," *J. Am. Chem. Soc.*, vol. 139, no. 7, pp. 2630–2638, Feb. 2017, doi: 10.1021/jacs.6b09645.

[78] Z. Xiao, K.-Z. Du, W. Meng, D. B. Mitzi, and Y. Yan, "Chemical Origin of the Stability Difference between Copper(I)- and Silver(I)-Based Halide Double Perovskites," *Angew. Chem. Int. Ed.*, vol. 56, no. 40, pp. 12107–12111, 2017, doi: 10.1002/anie.201705113.

[79] M. Nabi and D. C. Gupta, "Potential lead-free small band gap halide double perovskites Cs2CuMCl6 (M = Sb, Bi) for green technology," *Sci. Rep.*, vol. 11, no. 1, p. 12945, Jun. 2021, doi: 10.1038/s41598-021-92443-1.

[80] M. Delor *et al.*, "Carrier Diffusion Lengths Exceeding 1 μm Despite Trap-Limited Transport in Halide Double Perovskites," *ACS Energy Lett.*, vol. 5, no. 5, pp. 1337–1345, May 2020, doi: 10.1021/acsenergylett.0c00414.

[81] "Potential lead-free small band gap halide double perovskites Cs2CuMCl6 (M = Sb, Bi) for green technology | Scientific Reports." https://www.nature.com/articles/s41598-021-92443-1 (accessed Dec. 07, 2022).

[82] N. R. Wolf, B. A. Connor, A. H. Slavney, and H. I. Karunadasa, "Doubling the Stakes: The Promise of Halide Double Perovskites," *Angew. Chem. Int. Ed.*, vol. 60, no. 30, pp. 16264–16278, Jul. 2021, doi: 10.1002/anie.202016185.

[83] W. Zhou *et al.*, "Lead-Free Small-Bandgap $Cs_2CuSbCl_6$ Double Perovskite Nanocrystals," *J. Phys. Chem. Lett.*, vol. 11, no. 15, pp. 6463–6467, Aug. 2020, doi: 10.1021/acs.jpclett.0c01968.

[84] E. T. McClure, M. R. Ball, W. Windl, and P. M. Woodward, "Cs_2AgBiX_6 (X = Br, Cl): New Visible Light Absorbing, Lead-Free Halide Perovskite Semiconductors," *Chem. Mater.*, vol. 28, no. 5, pp. 1348–1354, Mar. 2016, doi: 10.1021/acs.chemmater.5b04231.

[85] M. R. Filip, X. Liu, A. Miglio, G. Hautier, and F. Giustino, "Phase Diagrams and Stability of Lead-Free Halide Double Perovskites $Cs_2BB'X_6$: B = Sb and Bi, B′ = Cu, Ag, and Au, and X = Cl, Br, and I," *J. Phys. Chem. C*, vol. 122, no. 1, pp. 158–170, Jan. 2018, doi: 10.1021/acs.jpcc.7b10370.

[86] T. Nakajima and K. Sawada, "Discovery of Pb-Free Perovskite Solar Cells via High-Throughput Simulation on the K Computer," *J. Phys. Chem. Lett.*, vol. 8, no. 19, pp. 4826–4831, Oct. 2017, doi: 10.1021/acs.jpclett.7b02203.

[87] P. Hohenberg and W. Kohn, "Inhomogeneous Electron Gas," *Phys. Rev.*, vol. 136, no. 3B, pp. B864–B871, Nov. 1964, doi: 10.1103/PhysRev.136.B864.

[88] M. Born and R. Oppenheimer, "Zur Quantentheorie der Molekeln," *Ann. Phys.*, vol. 389, no. 20, pp. 457–484, 1927, doi: 10.1002/andp.19273892002.

[89] W. Kohn and L. J. Sham, "Self-Consistent Equations Including Exchange and Correlation Effects," *Phys. Rev.*, vol. 140, no. 4A, pp. A1133–A1138, Nov. 1965, doi: 10.1103/PhysRev.140.A1133.

[90] D. R. Hartree, "The Wave Mechanics of an Atom with a Non-Coulomb Central Field. Part I. Theory and Methods," *Math. Proc. Camb. Philos. Soc.*, vol. 24, no. 1, pp. 89–110, Jan. 1928, doi: 10.1017/S0305004100011919.

[91] V. Fock, "Nherungsmethode zur Lsung des quantenmechanischen Mehrk rperproblems," *Z. Fr Phys.*, vol. 61, no. 1–2, pp. 126–148, Jan. 1930, doi: 10.1007/BF01340294.

[92] L. H. Thomas, "The calculation of atomic fields," *Math. Proc. Camb. Philos. Soc.*, vol. 23, no. 5, pp. 542–548, Jan. 1927, doi: 10.1017/S0305004100011683.

[93] E. H. Lieb and B. Simon, "The Thomas-Fermi theory of atoms, molecules and solids," *Adv. Math.*, vol. 23, no. 1, pp. 22–116, Jan. 1977, doi: 10.1016/0001-8708(77)90108-6.

[94] J. Hafner and G. Kresse, "The Vienna AB-Initio Simulation Program VASP: An Efficient and Versatile Tool for Studying the Structural, Dynamic, and Electronic Properties of Materials," in *Properties of Complex Inorganic Solids*, A. Gonis, A. Meike, and P. E. A. Turchi, Eds. Boston, MA: Springer US, 1997, pp. 69–82. doi: 10.1007/978-1-4615-5943-6_10.

[95] P. E. Blöchl, "Projector augmented-wave method," *Phys. Rev. B*, vol. 50, no. 24, pp. 17953–17979, Dec. 1994, doi: 10.1103/PhysRevB.50.17953.

[96] G. Kresse and J. Furthmüller, "Efficient iterative schemes for ab initio total-energy calculations using a plane-wave basis set," *Phys. Rev. B*, vol. 54, no. 16, pp. 11169–11186, Oct. 1996, doi: 10.1103/PhysRevB.54.11169.

[97] G. Kresse and D. Joubert, "From ultrasoft pseudopotentials to the projector augmented-wave method," *Phys. Rev. B*, vol. 59, no. 3, pp. 1758–1775, Jan. 1999, doi: 10.1103/PhysRevB.59.1758.

[98] J. P. Perdew, K. Burke, and M. Ernzerhof, "Generalized Gradient Approximation Made Simple," *Phys. Rev. Lett.*, vol. 77, no. 18, pp. 3865–3868, Oct. 1996, doi: 10.1103/PhysRevLett.77.3865.

[99] J. P. Perdew *et al.*, "Restoring the Density-Gradient Expansion for Exchange in Solids and Surfaces," *Phys. Rev. Lett.*, vol. 100, no. 13, p. 136406, Apr. 2008, doi: 10.1103/PhysRevLett.100.136406.

[100] R. A. Evarestov and V. P. Smirnov, "Modification of the Monkhorst-Pack special points meshes in the Brillouin zone for density functional theory and Hartree-Fock calculations," *Phys. Rev. B*, vol. 70, no. 23, p. 233101, Dec. 2004, doi: 10.1103/PhysRevB.70.233101.

[101] P. Wisesa, K. A. McGill, and T. Mueller, "Efficient generation of generalized Monkhorst-Pack grids through the use of informatics," *Phys. Rev. B*, vol. 93, no. 15, p. 155109, Apr. 2016, doi: 10.1103/PhysRevB.93.155109.

[102] L. He *et al.*, "Accuracy of generalized gradient approximation functionals for density-functional perturbation theory calculations," *Phys. Rev. B*, vol. 89, no. 6, p. 064305, Feb. 2014, doi: 10.1103/PhysRevB.89.064305.

[103] W. Travis, E. N. K. Glover, H. Bronstein, D. O. Scanlon, and R. G. Palgrave, "On the application of the tolerance factor to inorganic and hybrid halide perovskites: a revised system," *Chem. Sci.*, vol. 7, no. 7, pp. 4548–4556, 2016, doi: 10.1039/C5SC04845A.

[104] C. Li, X. Lu, W. Ding, L. Feng, Y. Gao, and Z. Guo, "Formability of ABX_3 (X = F, Cl, Br, I) halide perovskites," *Acta Crystallogr. B*, vol. 64, no. 6, pp. 702–707, Dec. 2008, doi: 10.1107/S0108768108032734.

[105] H. Hayashi, H. Inaba, M. Matsuyama, N. G. Lan, M. Dokiya, and H. Tagawa, "Structural consideration on the ionic conductivity of perovskite-type oxides," *Solid State Ion.*, vol. 122, no. 1, pp. 1–15, Jul. 1999, doi: 10.1016/S0167-2738(99)00066-1.

[106] C. C. Stoumpos, C. D. Malliakas, and M. G. Kanatzidis, "Semiconducting tin and lead iodide perovskites with organic cations: phase transitions, high mobilities, and near-infrared photoluminescent properties," *Inorg. Chem.*, vol. 52, no. 15, pp. 9019–9038, Aug. 2013, doi: 10.1021/ic401215x.

[107] S.-H. Wei, W.-J. Yin, J.-H. Yang, J. Kang, and Y. Yan, "Halide perovskite materials for solar cells: a theoretical review," *J Mater Chem*, Jan. 2015, doi: 10.1039/C4TA05033A.

[108] R. D. Shannon, "Revised effective ionic radii and systematic studies of interatomic distances in halides and chalcogenides," *Acta Crystallogr. Sect. A*, vol. 32, no. 5, pp. 751–767, Sep. 1976, doi: 10.1107/S0567739476001551.

[109] M. Born, “On the stability of crystal lattices. I,” *Math. Proc. Camb. Philos. Soc.*, vol. 36, no. 2, pp. 160–172, Apr. 1940, doi: 10.1017/S0305004100017138.

[110] J. K. D. Verma and B. D. Nag, “On the Elastic Moduli of a Crystal and Voigt and Reuss Relations,” *J. Phys. Soc. Jpn.*, vol. 20, no. 4, pp. 635–636, Apr. 1965, doi: 10.1143/JPSJ.20.635.

[111] F. Mouhat and F.-X. Coudert, “Necessary and sufficient elastic stability conditions in various crystal systems,” *Phys. Rev. B*, vol. 90, no. 22, p. 224104, Dec. 2014, doi: 10.1103/PhysRevB.90.224104.

[112] B. B. Karki, G. J. Ackland, and J. Crain, “Elastic instabilities in crystals from ab initio stress - strain relations,” *J. Phys. Condens. Matter*, vol. 9, no. 41, p. 8579, Oct. 1997, doi: 10.1088/0953-8984/9/41/005.

[113] R. Hill, “The Elastic Behaviour of a Crystalline Aggregate,” *Proc. Phys. Soc. Sect. A*, vol. 65, no. 5, pp. 349–354, May 1952, doi: 10.1088/0370-1298/65/5/307.

[114] S. I. Ranganathan and M. Ostoja-Starzewski, “Universal Elastic Anisotropy Index,” *Phys. Rev. Lett.*, vol. 101, no. 5, p. 055504, Aug. 2008, doi: 10.1103/PhysRevLett.101.055504.

[115] S. F. Pugh, “XCII. Relations between the elastic moduli and the plastic properties of polycrystalline pure metals,” *Lond. Edinb. Dublin Philos. Mag. J. Sci.*, vol. 45, no. 367, pp. 823–843, Aug. 1954, doi: 10.1080/14786440808520496.

[116] J.-M. Zhang, Y. Zhang, K.-W. Xu, and V. Ji, “Young’s modulus surface and Poisson’s ratio curve for cubic metals,” *J. Phys. Chem. Solids*, vol. 68, no. 4, pp. 503–510, Apr. 2007, doi: 10.1016/j.jpcs.2007.01.025.

[117] H. Niu *et al.*, “Extra-electron induced covalent strengthening and generalization of intrinsic ductile-to-brittle criterion,” *Sci. Rep.*, vol. 2, no. 1, p. 718, Dec. 2012, doi: 10.1038/srep00718.

[118] S. Kumar and J. Jung, “Mechanical and electronic properties of Ag3Sn intermetallic compound in lead free solders using ab initio atomistic calculation,” *Mater. Sci. Eng. B*, vol. 178, no. 1, pp. 10–21, Jan. 2013, doi: 10.1016/j.mseb.2012.10.003.

[119] M. G. Brik, “First-principles calculations of electronic, optical and elastic properties of ZnAl2S4 and ZnGa2O4,” *J. Phys. Chem. Solids*, vol. 71, no. 10, pp. 1435–1442, Oct. 2010, doi: 10.1016/j.jpcs.2010.07.007.

[120] M. I. Naher and S. H. Naqib, “An ab-initio study on structural, elastic, electronic, bonding, thermal, and optical properties of topological Weyl semimetal TaX (X = P, As),” *Sci. Rep.*, vol. 11, no. 1, p. 5592, Mar. 2021, doi: 10.1038/s41598-021-85074-z.

[121] E. Schreiber, O. L. Anderson, N. Soga, and J. F. Bell, “Elastic Constants and Their Measurement,” *J. Appl. Mech.*, vol. 42, no. 3, pp. 747–748, Sep. 1975, doi: 10.1115/1.3423687.

[122] P. Ravindran, L. Fast, P. A. Korzhavyi, B. Johansson, J. Wills, and O. Eriksson, “Density functional theory for calculation of elastic properties of orthorhombic crystals: Application to TiSi2,” *J. Appl. Phys.*, vol. 84, no. 9, pp. 4891–4904, Nov. 1998, doi: 10.1063/1.368733.

[123] O. L. Anderson, “A simplified method for calculating the debye temperature from elastic constants,” *J. Phys. Chem. Solids*, vol. 24, no. 7, pp. 909–917, Jul. 1963, doi: 10.1016/0022-3697(63)90067-2.

[124] M. Gajdoš, K. Hummer, G. Kresse, J. Furthmüller, and F. Bechstedt, “Linear optical properties in the projector-augmented wave methodology,” *Phys. Rev. B*, vol. 73, no. 4, p. 045112, Jan. 2006, doi: 10.1103/PhysRevB.73.045112.

[125] F. Mahboub, G. Alghamdi, S. Al-Omari, and A. A. Mubarak, “Ab initio investigation of the structural, electronic, magnetic and optical properties of the perovskite TlMnX 3 (X = F, Cl) compounds,” *Int. J. Mod. Phys. B*, vol. 30, p. 1650031, Mar. 2016, doi: 10.1142/S0217979216500314.

[126] A. Kudo and Y. Miseki, “Heterogeneous photocatalyst materials for water splitting,” *Chem. Soc. Rev.*, vol. 38, no. 1, pp. 253–278, Dec. 2008, doi: 10.1039/B800489G.

[127] X. Zhang, X. Zhao, D. Wu, Y. Jing, and Z. Zhou, “MnPSe3 Monolayer: A Promising 2D Visible-Light Photohydrolytic Catalyst with High Carrier Mobility,” *Adv. Sci.*, vol. 3, no. 10, p. 1600062, Apr. 2016, doi: 10.1002/advs.201600062.

[128] V. Chakrapani, J. C. Angus, A. B. Anderson, S. D. Wolter, B. R. Stoner, and G. U. Sumanasekera, “Charge Transfer Equilibria Between Diamond and an Aqueous Oxygen Electrochemical Redox Couple,” *Science*, vol. 318, no. 5855, pp. 1424–1430, Nov. 2007, doi: 10.1126/science.1148841.

[129] L. Lu, X. Pan, J. Luo, and Z. Sun, “Recent Advances and Optoelectronic Applications of Lead-Free Halide Double Perovskites,” *Chem. – Eur. J.*, vol. 26, no. 71, pp. 16975–16984, 2020, doi: https://doi.org/10.1002/chem.202000788.

[130] L. Lei, Q. Dong, K. Gundogdu, and F. So, “Metal Halide Perovskites for Laser Applications,” *Adv. Funct. Mater.*, vol. 31, no. 16, p. 2010144, 2021, doi: https://doi.org/10.1002/adfm.202010144.

[131] X. Xiao *et al.*, “Recent Advances in Halide Perovskite Memristors: Materials, Structures, Mechanisms, and Applications,” *Adv. Mater. Technol.*, vol. 5, no. 6, p. 1900914, 2020, doi: https://doi.org/10.1002/admt.201900914.